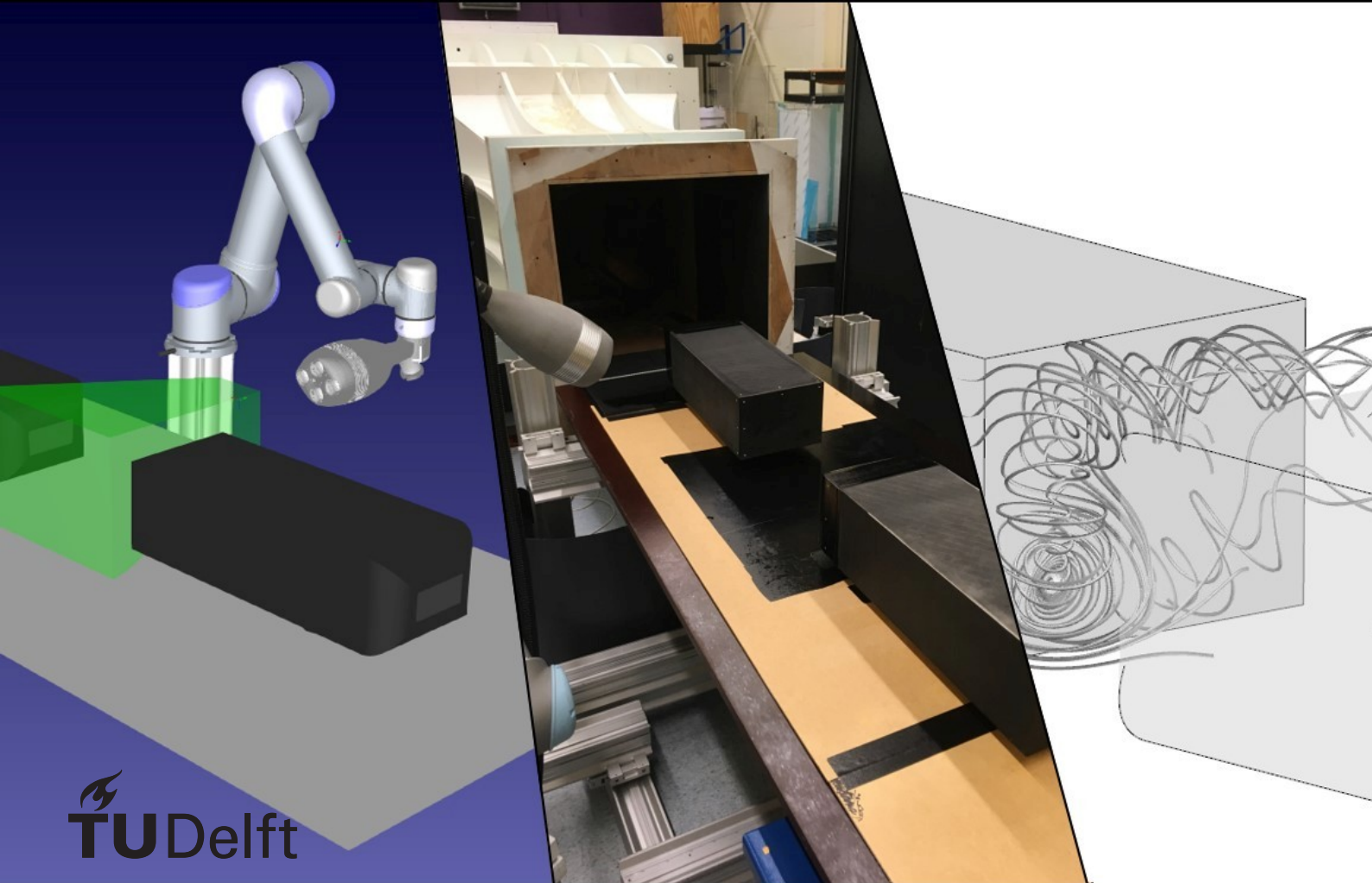


# Aerodynamics of Platooning Ahmed Bodies

An experimental analysis using large-scale PIV,  
pressure, and force measurements  
A. Naorniakowski

Delft University of Technology





# Aerodynamics of Platooning Ahmed Bodies

An experimental analysis using large-scale PIV,  
pressure, and force measurements

by

A. Naorniakowski

to obtain the degree of Master of Science  
at the Delft University of Technology,

Student number: 4229541

Thesis Committee:

Dr. A. Sciacchitano,

Ir. R. Veldhuizen,

Dr.ir. B.W. van Oudheusden,

Dr.ir. T. Sinnige,

TU Delft, Daily Supervisor

WABCO, Daily Supervisor

TU Delft

TU Delft



# Acknowledgements

This thesis could not have been completed without the assistance of several people, to whom I would like to express my gratitude. I would like to thank Gandert van Raemdonck for providing the research topic, and for his assistance during the conceptual design of the experiments. My thanks go out to the staff of the High-Speed Lab for their help fabricating the vehicle models. Furthermore, thank you to Joris van den Berg and Constantin Jux for being generous with their advice and their time during all stages of this project. Finally, I am grateful for the guidance and entrusted freedom in the execution of this project provided by my daily supervisors Andrea Sciacchitano and Roy Veldhuizen.

*Alexander Naorniakowski  
Delft, February 2020*



# Summary

Heavy-Duty Vehicles (HDVs) are responsible for a measurable and growing portion of the worldwide greenhouse gas emissions. As aerodynamic drag constitutes the single biggest source of engine power demand for HDVs at highway speeds, aerodynamic improvements are an effective measure to reduce fuel consumption and thus greenhouse gas emissions. Automated close-distance following of two or more HDVs, better known as “platooning”, can lead to lower drag through beneficial aerodynamic interference effects.

While the influence of longitudinal separation distance between HDVs on the aerodynamic drag of the vehicles has been investigated in several studies, considerably less research has been done on the influence of relative lateral positioning or “misalignment”. This report covers a wind-tunnel experiment with two simplified models, which are known as squareback Ahmed bodies, in several longitudinal and lateral positions. Pressure measurements were done on the rear face of the leading models, and force measurements were done on both models utilizing integrated load cells. Coaxial Volumetric Velocimetry, a large-scale Particle Image Velocimetry technique, was used for reconstruction of the mean three-dimensional velocity field in the gap between the models. Three separation distances were tested:  $20\%L$ ,  $40\%L$ ,  $60\%L$ , where  $L$  is model length. For each longitudinal separation distance five lateral positions were tested:  $-25\%W$ ,  $-15\%W$ ,  $0\%W$ ,  $15\%W$ ,  $25\%W$  where  $W$  is model width.

Based on the force readings it has been found that, for zero lateral offset, the leading model benefits of reduced drag coefficients for all separation distances. Pressure measurements confirm that the pressure across the base area is increased relative to the vehicle in isolation. The trailing model, on the other hand, suffers from increased drag coefficients at the tested separation distances. The positive effects of driving in a low-momentum wake are negated by secondary aerodynamic effects that increase the pressure on the nose section of the trailing model.

The introduction of lateral stagger generally increases the drag coefficient, relative to the drag coefficient when aligned, for all models and all separation distances. The magnitude of the drag coefficient increase is dependent on the separation distance. The smaller the separation distance is, the more negative impact lateral offset has. Pressure measurements show that areas of low pressure occur on the base of the leading model at the side to which the trailing model moves. That is: if the trailing model is offset to the left of the leading model, then an area of lower pressure exists across the left part of the base area of the leading model.

Time-averaged flow field visualizations show that for a platoon at  $0.6L$  separation, the near wake flow topology remains largely unchanged when a lateral offset is introduced. At  $0.2L$  separation, however, the wake topology changes considerably with lateral offset. When aligned, a toroidal vortex exists in the gap between the models. The toroidal structure changes in a horseshoe vortex when the platoon is laterally misaligned. The topological change is accompanied by strong flow curvature and leads to regions of low pressure across the base of the leading model.



# Contents

<b>Nomenclature</b>	<b>ix</b>
<b>List of Figures</b>	<b>xi</b>
<b>List of Tables</b>	<b>xv</b>
<b>1 Introduction</b>	<b>1</b>
<b>2 Prior Research &amp; Objectives of Current Work</b>	<b>5</b>
2.1 What is a heavy-duty vehicle? . . . . .	5
2.2 Introduction to drag characteristics of a Heavy-Duty Vehicle . . . . .	5
2.3 Bluff Body Aerodynamics . . . . .	7
2.3.1 Reference models . . . . .	7
2.3.2 Wake drag . . . . .	8
2.3.3 Forebody Drag . . . . .	13
2.4 Toolbox: Coaxial Volumetric Velocimetry . . . . .	15
2.5 Wake flow past the squareback Ahmed Body . . . . .	17
2.6 Drafting . . . . .	19
2.6.1 Aerodynamic principles of drafting . . . . .	19
2.6.2 Agreement between field tests and other experiments . . . . .	22
2.6.3 Lateral Stagger . . . . .	24
2.7 Research Plan . . . . .	25
2.7.1 Objective. . . . .	25
2.7.2 Methodology. . . . .	26
<b>3 Experimental Setup</b>	<b>27</b>
3.1 Setup . . . . .	27
3.1.1 Wind Tunnel . . . . .	27
3.1.2 Scale Model Construction . . . . .	27
3.1.3 Experiment Lay Out . . . . .	29
3.2 Instrumentation . . . . .	29
3.2.1 Load Sensors. . . . .	29
3.2.2 Pressure Ports . . . . .	31
3.2.3 Coaxial Volumetric Velocimetry . . . . .	31
3.3 Data Collection and Processing . . . . .	32
3.3.1 Test Plan . . . . .	32
3.3.2 Force Coefficients . . . . .	33
3.3.3 Pressure Coefficients. . . . .	33
3.3.4 Wind Tunnel Corrections . . . . .	34
3.3.5 Image Processing and Flow Field Analysis . . . . .	36
<b>4 Results</b>	<b>39</b>
4.1 Force measurements . . . . .	39
4.1.1 Isolated Ahmed Body . . . . .	39
4.1.2 Ahmed Body Platoon. . . . .	40
4.2 Pressure tap measurements. . . . .	43
4.2.1 Isolated Ahmed Body . . . . .	43
4.2.2 Ahmed Bodies Platoon. . . . .	45
4.3 Coaxial Volumetric Velocimetry measurements. . . . .	50
4.3.1 Isolated Ahmed body . . . . .	50
4.3.2 Aligned Platoon . . . . .	50
4.3.3 Platoon at 25%W Lateral Offset . . . . .	54

---

4.4	Discussion . . . . .	58
4.4.1	On the trailing model drag savings . . . . .	58
4.4.2	On bi-stability . . . . .	59
4.4.3	On the influence of lateral stagger . . . . .	60
<b>5</b>	<b>Conclusion &amp; Recommendations</b>	<b>63</b>
5.1	Conclusions. . . . .	63
5.2	Recommendations . . . . .	64
<b>A</b>	<b>Wind tunnel force measurement corrections</b>	<b>65</b>
	<b>Bibliography</b>	<b>69</b>

# Nomenclature

## Abbreviation

CFD	Computational Fluid Dynamics
COE	Cab Over Engine
CVV	Coaxial Volumetric Velocimetry
FSS	Full Scale Span
GETS	Generic European Transportation System
GHG	Greenhouse Gas
GTS	Ground transportation System
GVWR	Gross Vehicle Weight Rating
HDV	Heavy-Duty Vehicle
HFSB	Helium-Filled Soap Bubbles
PIV	Particle Image Velocimetry
PTV	Particle Tracking Velocimetry
STB	Shake-The-Box
V2V	Vehicle-to-Vehicle

## Symbols

$\bar{M}$	Mach number at dividing streamline	-
$\bar{u}$	Velocity at dividing streamline	m/s
$\dot{m}_{fuel}$	Fuel flow	kg/s
$\eta$	Influence factor	-
$\gamma$	Heat Capacity Ratio	-
$\rho$	Air density	kg/m <sup>3</sup>
$A$	Vehicle frontal area	m <sup>2</sup>
$C_D$	Aerodynamic drag coefficient	-
$c_{p\infty}$	Freestream pressure coefficient	-
$c_p$	Pressure coefficient	-
$C_{x^*}$	Force coefficient, x-axis, body mounted reference frame	-
$C_{y^*}$	Force coefficient, y-axis, body mounted reference frame	-
$C_{z^*}$	Force coefficient, z-axis, body mounted reference frame	-
$f_{r011}$	Rolling friction drag coefficient	-

$F_{Aero}$	Aerodynamic drag	N
$F_{Grade}$	Drag due to vehicle inclination	N
$F_{RL}$	Sum of vehicle drag forces	N
$F_{RR}$	Rolling resistance drag	N
$H$	Model height	0.143 m
$h^*$	Half of nondimensional (w.r.t $H$ ) lateral distance between pressure ports	–
$m$	Vehicle mass	kg
$m_{rev}$	Reverse mass flow	kg/s
$m_{scav}$	Scavenging mass flow	kg/s
$p'$	Downstream pressure	Pa
$p_{\infty}$	Freestream pressure	Pa
$p_b$	Base pressure	m/s
$p_d$	Base pressure	Pa
$p_{room}$	Pressure in plenum chamber	Pa
$u_*$	Mixing layer velocity ratio	-
$u_l$	Velocity downstream of near-wake	m/s
$u_e$	Velocity at edge of mixing layer	m/s
$x^*$	Nondimensional (w.r.t. $H$ ) x-axis, body mounted reference frame	–
$y^*$	Nondimensional (w.r.t. $H$ ) y-axis, body mounted reference frame	–
$z^*$	Nondimensional (w.r.t. $H$ ) z-axis, body mounted reference frame	–
$g$	Gravitational acceleration	9.81 m/s <sup>2</sup>

# List of Figures

1.1	Greenhouse Gas (GHG) emissions per sector and per transportation mode in 2016. Total EU-28 GHG emissions were 4440 million tonnes CO <sub>2</sub> eq, total US GHG emissions were 6492 million tonnes CO <sub>2</sub> eq. Naming differences are due to dissimilar categorization criteria in sources. Data compiled from [18] and [75]	2
1.2	Wireless communications between two platooning vehicles will ensure direct responses to actions taken by leading vehicles. Radar/lidar provides data for precision position keeping. Figure taken from [38]	3
2.1	Common tractor type distinction. Images courtesy of Volvo Trucks.	6
2.2	Power required to overcome aerodynamic drag versus required power to overcome rolling friction and enable accessories. Figure representative of a loaded regular-cab tractor-trailer. Typical highway speeds are between 50 and 60 MPH. Figure taken from [9]	7
2.3	Sources of drag on a regular truck. Figure taken from [81].	7
2.4	Example of HDV aerodynamic modifications (a) and their effect on wind averaged drag coefficient (b). Figure taken from: [46]	8
2.5	Dimensions of the Ahmed body (a), and the Ground Transportation System (b). Figures taken from [1, 31]	8
2.6	Impression of inviscid (ideale), and viscid (reale) flow (Strömung), around a simple bluff body. Figure taken from [35]	9
2.7	Pressure measurements along an Ahmed body in the vertical plane (a), and horizontal plane (b). Figure taken from [27]	9
2.8	Instability of a free shear layer for flow separated on a backwards facing corner. Figure taken from [36]	10
2.9	Impression of the flow at the separation point of a backward-facing step (a), and at the reattachment area (b). Figure taken from [12]	12
2.10	Impression of the mass flow equilibrium between scavenging mass flow, and the reverse mass flow at reattachment. Figure taken from [12]	12
2.11	Shadowgraph of a turbulent mixing layer between Helium (upper stream) and nitrogen (lower stream). Image taken from [61]	13
2.12	Impression of time-averaged wake behind a sphere. $S$ indicates the separation point (line for 3D objects), $P_b$ indicates the base pressure, and $R$ indicates the reattachment point. Image taken from [4]	13
2.13	Separation behind a squareback vehicle model, schematic impression of time-averaged flow topology. Visible are the recirculation zone (ring-type vortex), and the mixing layer (small circles), which consists of coherent vortices. Figure taken from [36]	14
2.14	Normalized flow velocity and streamlines for time-averaged (a-c), and instantaneous (d-e) flow behind a GTS-type body. Figure taken from [58]	14
2.15	Typical drag coefficient behavior relative to Reynolds number for HDVs. Figure reproduced from [79].	15
2.16	Edge radius $\eta$ (radius/width) versus Reynolds number. Critical edge radius is given for either edge-based, or width-based Reynolds number (left, and right line respectively). Figure taken from [80].	15
2.17	Pressure drag coefficients for a number of semi-infinite shapes. Figure taken from [34].	15
2.18	Schematic overview of a planar PIV system. Figure reproduced from [25]	16
2.19	CVV (left) and typical Tomographic PIV (right) setups. The red area indicates the overlap between cameras and laser light. Figure reproduced from [25]	16
2.20	Schematic representation of the computational steps and their effect on the residual image, for one time step and one camera. Figure copied from [65]	17
2.21	Ahmed body side profile, slant angle definition, and drag contribution of sections.	18

2.22	PIV recordings of the time-averaged flow field at the vertical center plane (a), and the horizontal center plane (b). Figures reproduced from [27]. . . . .	18
2.23	Vortex structures behind an Ahmed body with slanted rear. Acquisition done by means of CVV. Figure reproduced from [25] . . . . .	18
2.24	Oscillatory vortex shedding behind an Ahmed body. Figure reproduced from [58] . . . . .	19
2.25	Conditionally averaged flow field behind Ahmed body, showing one of the bi-stable states. Figure reproduced from [27]. . . . .	19
2.26	Pressure coefficient gradient across horizontal plane (a), and vertical plane (b). Bi-stability clearly visible for horizontal pressure distribution. Figure reproduced from [27]. . . . .	19
2.27	Smoke visualization of flow in gap between circular disc and semi-infinite cylinder. Non-bracketed number indicates gap width relative to cylinder diameter, bracketed number is the associated drag coefficient. Figure reproduced from [43]. . . . .	20
2.28	Drag coefficient $C_{D_m}$ of plate and semi-infinite afterbody for range of nondimensional gap widths between plate and afterbody $g/d_2$ . Front plate to afterbody diameter ratio $d_1/d_2$ is 0.25. Triangles indicate sharp afterbody corners, dots indicate rounded corners. Figure reproduced from [43]. . . . .	20
2.29	Conditionally averaged flow fields in tractor-trailer spacing for gap distance of $0.55G/\sqrt{tA}$ . Symmetry breakdown has been linked to steep drag increases. Figure reproduced from [32] . . .	21
2.30	Drag Coefficient of tractor, trailer, and combination for a GTS-type wind tunnel model, for a range of tractor trailer gaps. Figure reproduced from [32] . . . . .	21
2.31	Drag coefficients of leading ( $\circ$ ), and trailing ( $\Delta$ ) models in a platoon. Figure reproduced from [32] . . . . .	22
2.32	Pressure coefficient difference along front end of GETS model, vertical midplane location. Nr.2 vehicle in platoon, D indicates the normalized separation distance Gap/Length. Pressure coefficient difference defined as difference between #1 vehicle and #2 vehicle pressure coefficient ( $c_{p_{lead}} - c_{p_{mid}}$ ) at equal locations on the front end contour. Figure reproduced from [24]. . . . .	22
2.33	PIV recordings of the time-averaged flow field at the horizontal center plane at 0.63 vehicle widths longitudinal separation (a), and 2.84 vehicle widths longitudinal separation (b). Figures reproduced from [72] . . . . .	23
2.34	Comparison of fuel savings for trailing vehicle in 2, and 3-vehicle platoons in several field test studies and one WT experiment. Figure reproduced from [47] . . . . .	23
2.35	Drag reduction for regular cab tractor-trailers for two vehicle platoons that are aligned, and laterally staggered by 2 feet (0.6 meters). CFD results. Figure reproduced from [37]. . . . .	24
2.36	Yaw dependant drag coefficient improvements for aft ruck in two-vehicle drafting of regular-cab tractor-trailers. WT experiment. Figure reproduced from [47] . . . . .	24
3.1	Exploded view of Ahmed body internal structure and load cell. Body panels not shown. . . . .	28
3.2	Image of model #2 with ZigZag strips applied. . . . .	28
3.3	Schematic representation of ZZ strip position relative to the corner radius. Arrows indicate locations for models numbered #1 and #2, respectively. . . . .	28
3.4	Pressure port ( $\circ$ ) locations across rear face of model #1. The coordinate system is vehicle based, and normalized by model height $H$ . . . . .	29
3.5	Rendering of Ahmed bodies, floorboard, and robotic arm with <i>MiniShaker</i> as installed in the wind tunnel. The green cone represents the illuminated volume that is recorded by the cameras in the <i>MiniShaker</i> . . . . .	30
3.6	Image of test-section with annotations of models, <i>MiniShaker</i> , and nozzle. . . . .	30
3.7	Ahmed bodies in test section, side view (a), and top view (b). Definition of separation and stagger. . . . .	30
3.8	Force vectors and body oriented reference system on Ahmed body. Side view (a), and rear view (b). Lower solid line indicates floor. . . . .	33
3.9	Unfiltered load cell signal versus signal that has been averaged over 500 data points using a moving mean. Baseline and target force are easily distinguishable after averaging. . . . .	33
3.10	Correction factors at a range of test section locations. . . . .	35
3.11	Complete dynamic pressure correction at a range of test section locations. . . . .	35
3.12	Total and dynamic pressure in centre of empty jet (floorboard installed). Dynamic pressure in nozzle set to 106 [Pa]. Pressures are relative to plenum chamber static pressure. . . . .	35

3.13	Pressure coefficient distribution in in centre of empty jet (floorboard installed). Reference pressure is equal to plenum chamber pressure, dynamic pressure used for non-dimensionalizing is local dynamic pressure. . . . .	35
3.14	Processing of image with fluctuating background reflections. (a) Raw image, (b) RMS of intensity, (c) Gaussian and Butterworth filter applied to (a), (d) final result (image (c) minus a scaled version of image (b)). Images reproduced from [39]. . . . .	37
4.1	Drag coefficients of models and combined drag figure at 20% $L$ longitudinal separation. . . . .	40
4.2	Drag coefficients of models and combined drag figure at 40% $L$ longitudinal separation. . . . .	40
4.3	Drag coefficients of models and combined drag figure at 60% $L$ longitudinal separation. . . . .	41
4.4	Instantaneous drag force for platoon at 40% $L$ separation, 0°yaw, and no stagger. Drag values are obtained from applying a moving mean filter of window size 500 samples to the raw signal of 500Hz. Notice the aperiodic “jumps” in drag magnitude. . . . .	42
4.5	Side force coefficients of models and combined drag figure at 20% $L$ longitudinal separation. . .	42
4.6	Side force coefficients of models and combined drag figure at 40% $L$ longitudinal separation. . .	43
4.7	Side force coefficients of models and combined drag figure at 60% $L$ longitudinal separation. . .	43
4.8	Average pressure coefficient distribution on the rear face of model #1, in isolation at 0°yaw. . . .	44
4.9	Pressure coefficient distribution on the rear face of model #1, in isolation at (a) 5°yaw, and (b) at -5°yaw. . . . .	44
4.10	Probability Density Function of the pressure coefficient differential, in isolation at (a) 5°yaw, (b) 0°yaw, and (c) at -5°yaw. . . . .	45
4.11	Pressure coefficient map across rear face of model #1, at various stagger positions. Longitudinal separation is 20% $L$ and yaw is 0°. . . . .	46
4.12	Pressure coefficient map across rear face of model #1, at various stagger positions. Longitudinal separation is 40% $L$ and yaw is 0°. . . . .	47
4.13	Pressure coefficient map across rear face of model #1, at stagger positions. Separation is 60% and yaw is 0°. . . . .	48
4.14	Probability density functions of pressure coefficient gradient $\partial C_p / \partial y$ at $y^* = 0$ for leading vehicle in platoon. No stagger, 0°yaw, at: (a) 20% $L$ separation, (b) 40% $L$ separation, (c) 60% $L$ separation. . . . .	49
4.15	Contours of normalized average flow velocity in x-direction, and streamline patterns. Single vehicle (model #1) at 0°yaw. Bin size: 30x30x30 [ $mm^3$ ]. . . . .	51
4.16	Figure 4.16: Contours of average flow velocity in x-direction, and streamline patterns. Isolated model at 0°yaw. Location of vertical plane: $x^* = 0.6$ (left), $x^* = 1.68$ (right). Bin size: 30x30x30 [ $mm^3$ ] . . . . .	52
4.17	Three-dimensional vortex-core topology, identified using the “vortex core extraction method” in TecPlot 360 [70]. . . . .	52
4.18	Contours of average flow velocity in x-direction, and streamline patterns. Platoon at 60% $L$ longitudinal separation, 0% $W$ lateral stagger, and 0°yaw. Bin size: 30x30x30 [ $mm^3$ ]. . . . .	53
4.19	Contours of average flow velocity in x-direction, and streamline patterns. Platoon at 20% $L$ longitudinal separation, 0% $W$ lateral stagger, and 0°yaw. Binsize 20x20x20 [ $mm^3$ ]. . . . .	55
4.20	Contours of average flow velocity in x-direction, and streamline patterns. Platoon at 60% $L$ longitudinal separation, -25% $W$ lateral stagger, and 0°yaw. Binsize 20x20x20 [ $mm^3$ ]. . . . .	56
4.21	Contours of average flow velocity in x-direction, and streamline patterns. Platoon at 20% $L$ longitudinal separation, -25% $W$ lateral stagger, and 0°yaw. Binsize 20x20x20 [ $mm^3$ ]. . . . .	57
4.22	Streamlines in gap between models at 20% $L$ longitudinal separation, 0% $W$ lateral stagger, at 0°yaw. Streamline colors are used to increase contrast, and do not represent flow velocity. . . . .	58
4.23	Streamlines in gap between models at 20% $L$ longitudinal separation, -25% $W$ lateral stagger, at 0°yaw. Streamline colors are used to increase contrast, and do not represent flow velocity. . . . .	58
4.24	Drag coefficient of two streamlined struts in tandem. Figure reproduced from [34]. . . . .	59
4.25	Likelihood of observing either state in a bi-stable system as a function of sideslip angle. $\alpha$ is indicative of the likelihood of observing states $B_1$ or $B_2$ , as expressed by $A = \alpha B_1 + (1-\alpha) B_2$ , where $A$ indicates the flow field as averaged over a long time interval. Figure reproduced from [33] . . .	60

---

4.26	Schematic top view representation of gap flow for a platoon at $-25\%W$ lateral stagger and $20\%L$ longitudinal separation. Mass flow enters the region bounded by the streamlines on the left, and is expelled at the right side. Exiting flow is due to entrainment from mixing layer. The minus sign indicates area of low pressure required to turn freestream flow into the gap. . . . .	61
A.1	Interference effects of open-jet wind tunnel and object. Image reproduced from [21], original by [36]. . . . .	65
A.2	Example of horizontal buoyancy effect of model in test-section. Image reproduced from [21]. . .	66
A.3	Differential pressure measurements for either nozzle or plenum method. Figure reproduced from [52]. . . . .	66

# List of Tables

3.1	Technical details of the W-tunnel at the TU Delft. . . . .	27
3.2	Basic dimension Ahmed body scale models. . . . .	29
3.3	Technical details of K3D60 load cells. . . . .	31
3.4	Technical details of Nub Systems pressure scanner. . . . .	31
3.5	Experiment variables. Yaw angle is 0°. Green cells indicate that only pressure and force measurements have been performed. Red cells indicate the pressure, force, and CVV measurements have been done. . . . .	32
3.6	Experimental testing conditions. . . . .	32
3.7	Wind tunnel correction data. *= Nozzle area minus area blocked by floorboard. . . . .	34
3.8	Dynamic pressure and horizontal buoyancy corrections per model station. . . . .	36
4.1	Mean drag ( $x^*$ ), and mean side force ( $y^*$ ) coefficients for isolated Ahmed bodies. The $\pm$ values indicate the standard deviation of the sample of means. . . . .	39
4.2	Mean drag ( $x^*$ ) force coefficients for average platoon (average combined drag coefficient). The average drag coefficient of the models in isolation is 0.27. . . . .	41
4.3	Average pressure coefficient ( $C_p$ ) across rear face of leading model for tested combinations of longitudinal separation and lateral offset. Sideslip angle is 0°, pressure averages are from single runs. . . . .	49





# Introduction

Road freight transport is a fundamental way of delivering goods over short and long distances in many parts of the world. In the United States, more than 40% of all goods (estimated by share of total tonne-kilometer of inland transport) are transported by road, and in the EU-28 that share is almost 50% [11, 18]. For many countries in the EU-28, more than 90% of road freight transport was done by vehicles with a permissible laden weight of 30 metric-tonnes or more, i.e. tractor-trailers. Although it is not a strict definition, such vehicles can be categorized as Heavy-Duty Vehicles (HDVs). HDVs are mostly powered by diesel engines and thus produce exhaust gasses that are harmful to the environment. Even though modern HDVs are relatively efficient compared to other types of freight transport when it comes to energy use per tonne-kilometer [68], their contribution to the emission of greenhouse gasses is notable. Around 5% of the total  $CO_2$  equivalent emissions in the European Union, and a similar share in the United States, stem from HDVs. For a breakdown of GHG emissions per sector and transportation mode, see fig. 1.1 [18, 75]. Improving the fuel efficiency of Heavy-Duty Vehicles is therefore desirable from an environmental standpoint. Additionally, it is also economically attractive, as fuel costs are a major expense to the HDV operators [55].

It is expected that lowering aerodynamic drag will be instrumental to improve HDV fuel consumption [55, 68]. Aerodynamically improved designs are especially effective at highway speeds, where the majority of engine power is used to overcome aerodynamic drag. To this day, most aerodynamic improvements have been designed as hardware add-ons to the tractor or trailer. A familiar example might be the common roof deflector which streamlines the transition between the tractor and trailer roof. However, drag reduction can also be gained from driving in formation at close following distances, which is better known as “drafting”. Essentially, a trailing vehicle drives in the low-momentum wake of the leading vehicle, which decreases the pressure on the front of the trailing vehicle, and thus reduces drag. Vice-versa, the area of elevated pressure in front of the trailing vehicle will “push” the leading vehicle. Therefore, both the leading and trailing vehicle(s) (drafting can be done with more than two vehicles) will benefit from lower fuel consumption in such a scenario.

With advancing electronic capabilities in automotive applications, the concept of vehicle-to-vehicle (V2V) communication may become a tool to improve the operational capabilities of HDVs. Among the potential applications is the idea of platooning (early research has called it the “Electronic Tow Bar”). Platooning is an automated way of driving in a close spaced convoy of two or more vehicles. A suite of onboard sensors monitors the environment of the truck, while communication modules relay information about the state of the vehicle to the other trucks in the convoy. Based on this information, braking, accelerating, and even steering can be controlled by an autopilot. The autopilot can react quickly to actions taken by the other truck because the V2V communications will relay control inputs such as braking. See fig. 1.2 for a schematic impression of V2V communication. The benefits of platooning can be several; according to [38]:

- **Safety** V2V communications will allow for trailing vehicles to slow down automatically when the leading vehicle reduces speed. Reaction times can be minimized, reducing the risk of head-tail collisions.
- **Traffic Flow** Close following will reduce the length of road required to transport a given volume of goods. Quick reaction times will reduce traffic jams that occur from fluctuating following distances.
- **Fuel Consumption** Close following provides aerodynamic benefits known as drafting. All vehicles in a platoon may benefit from reduced aerodynamic drag, thus reduced fuel consumption.

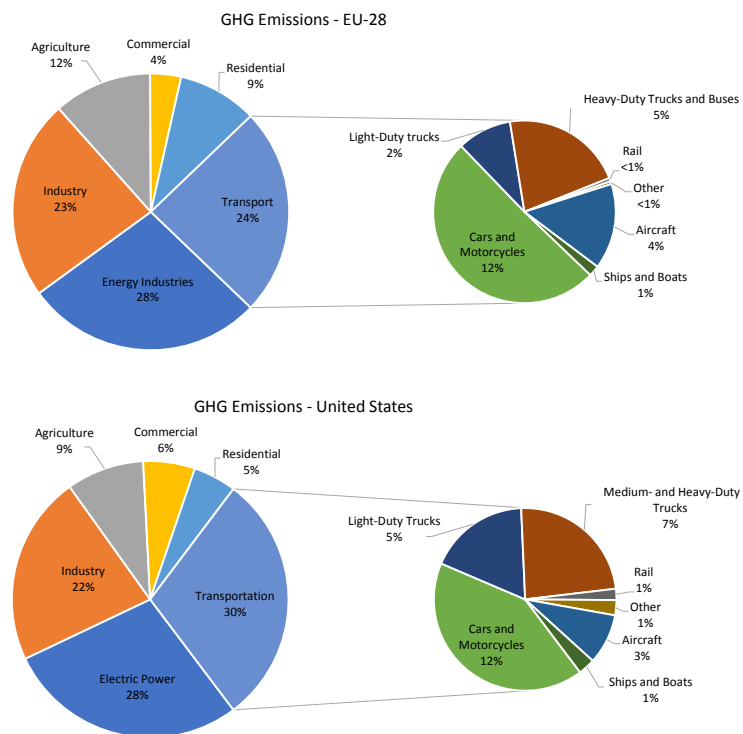


Figure 1.1: Greenhouse Gas (GHG) emissions per sector and per transportation mode in 2016. Total EU-28 GHG emissions were 4440 million tonnes CO<sub>2</sub>eq, total US GHG emissions were 6492 million tonnes CO<sub>2</sub>eq. Naming differences are due to dissimilar categorization criteria in sources. Data compiled from [18] and [75]

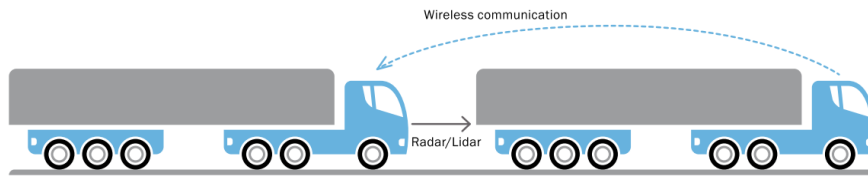


Figure 1.2: Wireless communications between two platooning vehicles will ensure direct responses to actions taken by leading vehicles. Radar/lidar provides data for precision position keeping. Figure taken from [38]

- **Driver Occupation** Systems capable of fully autonomous driving (following) may allow for drivers to disengage from steering the vehicle and let them rest or perform other (administrative) tasks.

As of now, there have been several successful tests in real-world traffic, see for example [3]. There is also genuine commercial interest. As a first indication for willingness to adopt the technology, the authors of [5, 7] interviewed fleet-managers and owner-operators about their potential interest. From this survey, it was concluded that the projected fuel-saving potential, regardless of other benefits, would be sufficient incentive to adopt an early form of platooning technology. However, there are still challenges associated with automated platooning, be it technological, economic or legislative in nature. To make platooning truly commonplace, it will be necessary to establish how vehicles from different manufacturers and owners can safely form a platoon and share the resulting profit fairly. Other road users will also need to adapt to sharing the road with convoys. Effective international regulation will likely be required to steer the development. From the perspective of the fuel-saving potential of platooning, further research is required to understand how exactly the individual vehicles influence each other. It should not be surprising that the aerodynamics of drafting HDVs is still an active field of research.

Which leads us to the work presented here. This thesis has been designed to improve the current understanding of aerodynamic interaction between HDVs, especially with off-design operating conditions in mind. To that end, a simplified, scaled platoon of two well-known aerodynamic bodies has been used as the basis for several experiments. Results from several instruments were tied together by the use of large-scale Coaxial Volumetric Velocimetry (CVV) technology that allowed for convenient reconstruction of the three-dimensional flow domain in between the models. This approach has hopefully lead to results which apply to full-scale platoons, and can one day be used to make the latter even more effective.



# 2

## Prior Research & Objectives of Current Work

The following chapter elaborates upon some of the aerodynamic characteristics of heavy-duty vehicles. The focus will be on primary drag sources. The goal of this review is to introduce the basics that define the drag of HDVs, and how drafting influences the flow characteristics.

### 2.1. What is a heavy-duty vehicle?

Before we start with the discussion of HDV aerodynamics, it is important to consider which vehicles classify as such. For regulatory and statistical purposes several classification systems exist, and some of them mention HDVs. For instance, North-American institutions such as the Federal Highway Administration distinguish between 13 “classes” of commercial vehicles, based on their visual appearance and intended use (truck, bus, motorcycle, number of axles, etc.), but also distinguish trucks based on vehicle weight in a separate system. The term heavy-duty is used to define all trucks having a gross vehicle weight rating (GVWR) of over 26,000 lbs (11,793 kg) [76]. The European Parliament identifies “lorries, busses, and coaches” as HDVs in some of their latest regulatory proposals, while a more strict classification of vehicles is based on weight and axle configuration [19]. As stated in the introduction, this thesis is concerned with drafting aerodynamics of road freight transport, and specifically large trucks, as those are the vehicles that are intended to form platoons first. Thus, for the remainder of this work, the term HDV will refer to trucks.

The common term “truck” (or “lorry” in British English) can apply to many vehicles, and therefore should also be explained further. When one speaks of a vehicle with a trailer that can pivot around a single joint, one speaks of a tractor-trailer or “semi”. If the trailer is rigidly attached to the tractor, the vehicle is called a rigid-truck. In the Federal Highway Administration truck classification system mentioned earlier, the common tractor-trailer is called a class-8 vehicle (GVWR of over 33,000 lbs (14,969 kg), the weight of tractor alone, trailer not included). This term is also used in some North-American literature on HDV aerodynamics. Two tractor designs are dominant in the road freight transport sector: The Cab Over Engine (COE) and the traditional truck. In Europe, the former is used most, while the latter is more familiar to the North American market. North American legislature dictates only the trailer length, while European legislature states the combined length. Therefore, European trucks require a more compact tractor to maximize useful cargo volume. The difference between the two tractors types can be seen in fig. 2.1. The nose shape of the traditional truck generally makes it more aerodynamically efficient than the COE design according to [63].

### 2.2. Introduction to drag characteristics of a Heavy-Duty Vehicle

Contrary to the seemingly streamlined shapes of modern passenger cars, conflicting design requirements have resulted in rather bulky vehicle shapes for most HDVs. That does not mean that aerodynamic forces are negligible. Figure fig. 2.2 qualitatively demonstrates the relative effect of aerodynamic drag on a typical class-8 truck based on vehicle speed. The graph shows that at highway speeds the aerodynamic drag is the dominant source of power demand. One should be aware that the relative share of power demanded to overcome aerodynamic drag is dependent on the weight of the vehicle, as the vehicle weight is related to the

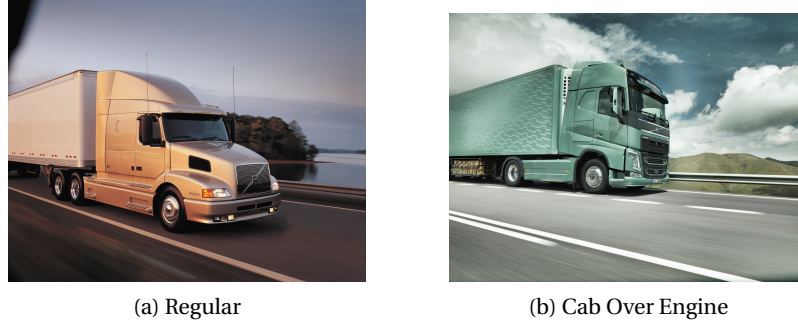


Figure 2.1: Common tractor type distinction. Images courtesy of Volvo Trucks.

rolling friction. This is important to bear in mind when comparing field tests, as many studies provide the relative gain in fuel consumption as a metric for aerodynamic improvement. To illustrate this point, let us start by considering the drag forces on a road vehicle. The following equations have been reproduced and modified from [8, 49]:

$$F_{RL} = F_{Aero} + F_{RR} + F_{Grade} \quad (2.1)$$

Here  $F_{RL}$  is the sum of drag forces, of which  $F_{Aero}$  is the aerodynamic drag,  $F_{RR}$  is the rolling resistance, and  $F_{Grade}$  the weight component along the driving direction when the vehicle is at an inclination. Let us assume that  $F_{Grade} = 0$ . One could state that fuel flow  $\dot{m}_{fuel}$  is proportional to the remaining force terms by means of proportionality factor  $k$ :

$$\dot{m}_{fuel} \approx k \cdot \left( \frac{1}{2} \rho A C_D v^2 + f_{roll} m g \right) \quad (2.2)$$

The aerodynamic drag has been expressed as a function of air density  $\rho$ , frontal area  $A$ , airspeed  $v$ , and aerodynamic drag coefficient  $C_D$  (in itself a function of yaw angle, and Reynolds number). The rolling resistance is a function of vehicle mass  $m$ , and rolling friction coefficient  $f_{roll}$ . Because it is difficult to obtain the proportionality factor from typical field test data, an expression for relative improvement simplifies matters (assuming a constant proportionality factor):

$$\frac{(\dot{m}_{fuel_0} - \dot{m}_{fuel})}{\dot{m}_{fuel_0}} = \frac{\frac{1}{2} \rho A v^2 \cdot (C_{D_0} - C_D)}{\left( \frac{1}{2} \rho A C_{D_0} v^2 + f_{roll} m g \right)} \quad (2.3)$$

The expression can be shortened to the following equation, in which the coefficient  $\eta$  can be tweaked to represent not just one constant velocity ( $\eta_{cv}$ ), but a scenario such as city-or highway driving [69]. For the field test of [8], the researchers suggest an influence factor  $\eta$  of 0.48 for a tractor-trailer which weighs 28 metric tonnes and is moving at 80 kilometers per hour. Thus, a drag coefficient reduction of 10%, for example, would reduce fuel consumption by 4.8%.

$$\frac{(F_0 - F)}{F_0} = \eta \cdot \frac{(C_{D_0} - C_D)}{C_{D_0}} \quad (2.4)$$

$$\eta = \eta_{cv} = \frac{1}{1 + f_{roll} \cdot \frac{g}{1/2 \cdot \rho} \cdot \frac{1}{v^2} \cdot \frac{m}{C_{D_0} A}} \quad (2.5)$$

Aerodynamic drag of tractor-trailer combinations can mainly be contributed to pressure drag of front, rear, wheels, the gap between tractor and trailer, and underside. The generalized schematic of fig. 2.3 provides an overview of the relative magnitude of drag sources on a tractor-trailer. It is important to note that the measurements on which fig. 2.3 is based are from 1978 and 1987[81]. Modern vehicles are likely to have a more streamlined tractor.

To improve drag that stems from the areas highlighted in fig. 2.3, general add-on modifications have been designed. For example, trailer skirts reduce underside turbulence, roof deflectors allow for cleaner airflow from tractor to trailer, and boat-tail trailing extensions reduce the area and unsteadiness of the wake. One comprehensive overview of add-ons that can be applied to a modern tractor-trailer can be found in [46].

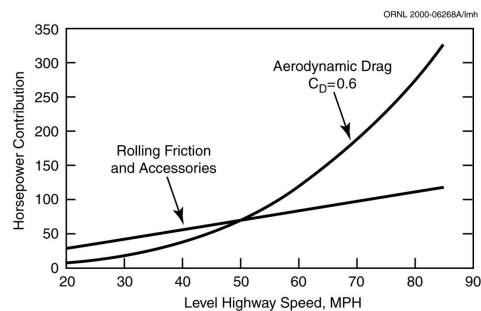


Figure 2.2: Power required to overcome aerodynamic drag versus required power to overcome rolling friction and enable accessories. Figure representative of a loaded regular-cab tractor-trailer. Typical highway speeds are between 50 and 60 MPH. Figure taken from [9]

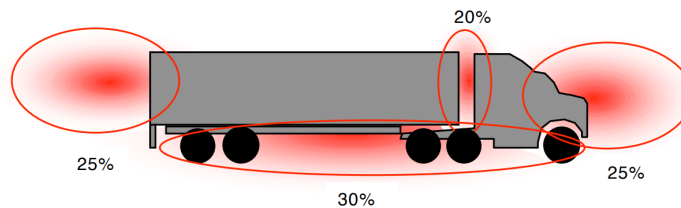


Figure 2.3: Sources of drag on a regular truck. Figure taken from [81].

The savings which are presented in fig. 2.4 illustrate that there is room for improvement for many HDVs on the road today. Surprisingly, most of the added devices have been tested many years ago (see also [14] for a historic perspective on HDV drag reduction). Yet, as expressed by both authors, many operators do not seem to equip their vehicles with the available technology. It has been suggested in [14] that some firms use too many different trailers to equip all with equal devices. Other devices might not be considered practical for everyday use. However, as efforts to reduce GHG emissions are increased, drag-lowering devices will likely become more commonplace.

## 2.3. Bluff Body Aerodynamics

In aerodynamic terms, Heavy-Duty Vehicles can be categorized as bluff bodies. Bluff bodies are associated with large regions of flow separation, which results in pressure drag. For bluff-bodies pressure drag, rather than viscous drag, is the primary drag source. In contrast, an airfoil is designed as a streamlined body, and drag is mostly due to friction between the airfoil and the passing air. Pressure drag stems from several areas on an HDV, as has been shown in the previous section. The magnitude of drag from each area is dependant on the detailed shape of the vehicle.

### 2.3.1. Reference models

To investigate flow behavior over an HDV in a more general sense, simplified reference models have been developed that do away with vehicle-specific details. Over the years, many simplified shapes have been used in literature. Two examples of such models are the Ground Transportation System (GTS) [31], and the Ahmed body [1], both shown in fig. 2.5. These models have streamlined frontal features and the typical vertical rear end, which is also called a squareback. The GTS features simplified wheels, while the Ahmed body is positioned on stilts. Neither model features the gap between tractor and trailer. The Ahmed body has originally been designed with passenger vehicles in mind. To that end, it can be equipped with different rear slopes, such that passenger car shapes such as the “hatchback” can be modeled. The squareback Ahmed body, however, has a vertical rear end similar to an HDV. The main difference between the GTS model and the Ahmed body is the width-height-ratio. The Ahmed body is wider than it is tall, unlike most HDVs.

If one is to take such a simplified shape and assume it is placed in inviscid flow, the pressure distribution would be similar to that shown in fig. 2.6. The figure shows the pressure distribution around a basic two-dimensional bluff body, with rounded front and rear edges. The pressure coefficient ( $c_p$ ) at the front is nearly identical for inviscid (ideale), and viscous (reale) solutions (as long as the flow stays attached). At the rear, inviscid flow fully recovers, thus the pressure coefficient distribution is equal to that of the front (see upper-right part of fig. 2.6). As is expected from inviscid theory, the drag is therefore zero. In viscous flow, however,

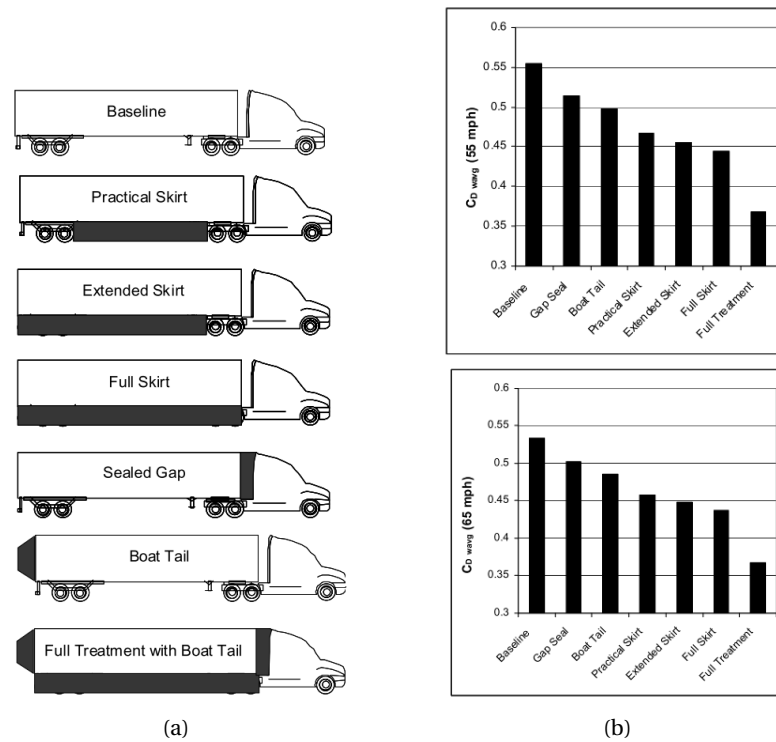


Figure 2.4: Example of HDV aerodynamic modifications (a) and their effect on wind averaged drag coefficient (b). Figure taken from: [46]

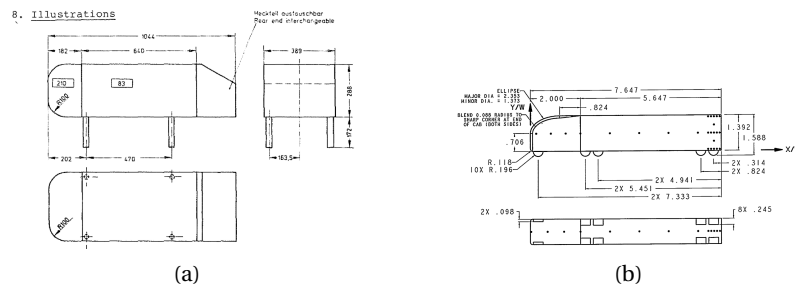


Figure 2.5: Dimensions of the Ahmed body (a), and the Ground Transportation System (b). Figures taken from [1, 31]

separation (Ablösung) will occur at the rear. The pressure does not recover, shown in both fig. 2.6, as well as in the experimental (three dimensional) results in fig. 2.7, and therefore significant pressure drag is experienced.

### 2.3.2. Wake drag

The area of separated flow over the rear of a squareback model is a well-studied example of a classical bluff body aerodynamics problem. The relevant question for the current work is how flow separation can lower base pressure. Due to its turbulent nature, accurate predictions about the specifics of the flow are based on CFD models or wind-tunnel experiments, rather than analytical models. However, a qualitative interpretation of the processes that define the wake can be given here, without the need to resort to numerical or empirical models yet. To that end, we will start with the following description of separated flow and pressure distribution at a backward-facing step. The theoretical model reproduced here is based on descriptions by [12], and [36].

In figs. 2.8 and 2.9 two-dimensional flow over a backward-facing step is shown, in which a stream of air moves along a solid boundary and separates at a sharp corner. The fine region between the faster-moving freestream and the “dead-air” behind the step is called the free shear layer. At Reynolds numbers typical for HDVs the free shear layer is very unstable, and it is likely to roll up into discrete eddies, as shown in the top three figures of fig. 2.8. The large eddies entrain air from the dead-air zone and thus reduce the velocity gradient between the dead-air and the freestream. This turbulent area between the freestream velocity and

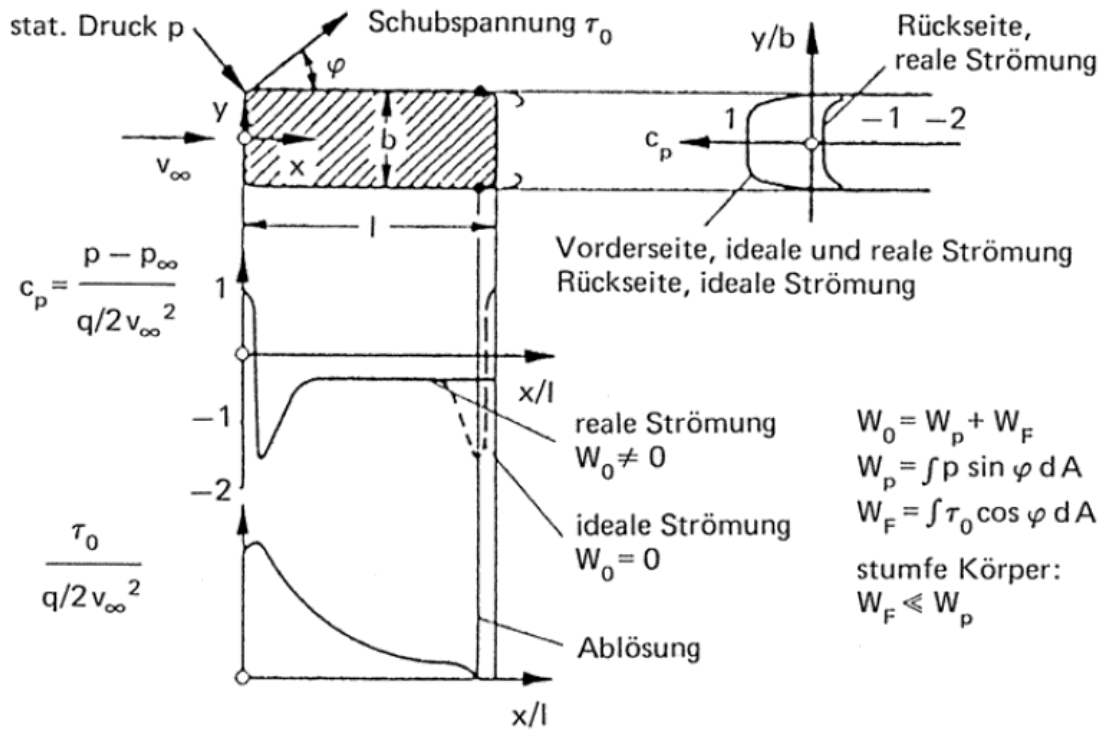


Figure 2.6: Impression of inviscid (ideale), and viscid (reale) flow (Strömung), around a simple bluff body. Figure taken from [35]

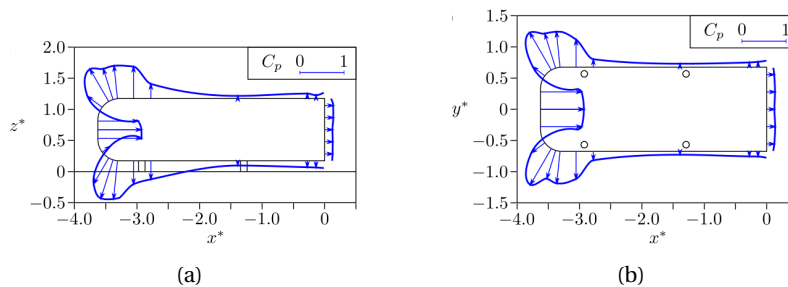


Figure 2.7: Pressure measurements along an Ahmed body in the vertical plane (a), and horizontal plane (b). Figure taken from [27]

the stagnant dead-air is called the mixing layer. The aforementioned entrainment is the process of mixing nonrotational flow into a turbulent stream, which is done by the eddies through inviscid “engulfment”, and by “nibbling” on a smaller viscous scale [16]. The large vortical structures in the mixing layer were first confirmed in [61]. It was found that entrainment is caused mainly by the large scale eddies in the shear layer, which was shown in shadowgraphs that are reproduced here in fig. 2.11. The image shows a mixing layer between two streams at different velocities and densities, but the principle applies for shear mixing in pure air. The unsteady flow in the mixing layer can be simplified, by showing the time-averaged velocity profile across it, as shown in the bottom figure of fig. 2.8.

Let us turn to the example of [12] to analyze the flow in the near wake of a bluff body. Through entrainment, or as the authors called it “scavenging”, the mixing layer accelerates air away from the base region of the backward step. This can be viewed as a constant mass flow leaving the dead air region ( $m_{scav}$ ), see fig. 2.9 (a). Thereby base pressure ( $p_d$ ) is lowered, which in turn curves the mixing layer towards a reattachment zone at the horizontal wall further downstream. The reattachment zone lies between two areas of pressure; low base pressure upstream and higher pressure downstream ( $p'$ ), see fig. 2.9 (b). The portion of the mixing layer that does not carry enough total pressure to overcome  $p'$  as it stagnates towards the reattachment zone, will flow back to the dead-air region. This should be viewed as mass flow entering the dead-air region ( $m_{rev}$ ).

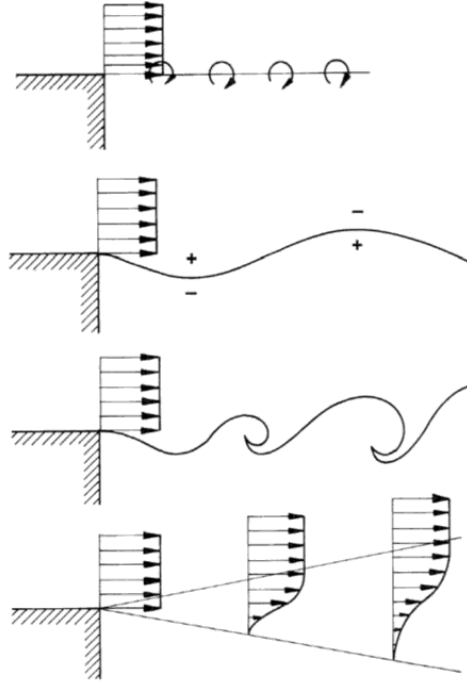


Figure 2.8: Instability of a free shear layer for flow separated on a backwards facing corner. Figure taken from [36]

In [12] the assumption is made that, at the point of separation, the static pressure across the mixing layer is constant and equal to the base pressure. A “dividing streamline” separates the streamlines which arrive from the freestream, and those that are enclosed within the dead air region. With knowledge of the velocity ratio between the edge of the mixing layer and the “dividing streamline” ( $\bar{u}_* \equiv \bar{u}/u_e$ ), it is possible to calculate the static pressure at the separation point by stating that the total pressure of the dividing streamline is equal to  $p'$ . Stagnation is assumed to be isentropic:

$$p_d = \frac{p'}{\left(1 + \frac{\gamma-1}{2} \bar{M}^2\right)^{\gamma/(\gamma-1)}} \quad (2.6)$$

Here,  $\gamma$  is the heat capacity ratio for air, and  $\bar{M}$  is the Mach number at the separating streamline. The authors demonstrate that for a laminar mixing layer of negligible thickness at separation, it is possible to calculate the base pressure explicitly. The result can be found in expression eq. (2.7), which is valid for subsonic, incompressible flow with the aforementioned assumptions about laminar mixing layers. Interestingly, the velocity ratio  $\bar{u}_*$  is independent of Reynolds number, and thus, for a given velocity profile, the base pressure is fully governed by the downstream pressure and velocity. A similar approach to calculating the base pressure for turbulent mixing layers could be done when the velocity profiles for turbulent mixing layers are known.

$$\frac{p_d - p'}{\frac{1}{2} \rho u^2} = - \frac{\bar{u}_*^2}{1 - \bar{u}_*^2} \quad (2.7)$$

An interpretation of the idea described above is shown in fig. 2.10 (a) and (b). The base pressure is the manifestation of a self-stabilizing balance between mass flow leaving the dead-air through entrainment in the mixing layer, and mass flow entering from the stagnation region. As shown in fig. 2.10 (b), any change in dead-air pressure will change the mass flow rate entering or leaving, which would translate into a condition away from the equilibrium. For example: assuming one starts from equilibrium, a temporary decrease in base pressure will cause a larger reverse flow, as more of the mixing layer is turned inward. However, a lower base pressure will also deflect the mixing layer such that it stagnates more upstream. The consequence is a shorter mixing layer that lowers the scavenging mass flow. As a result, there will be a net mass flow into the dead air region, which will increase the base pressure. Eventually, the system returns to equilibrium. In fig. 2.10 two curves are shown for the reverse flow, which are characterized by the location of transition. For

the curve which denotes transition before reattachment, only a small part slightly upstream of  $R$  is turbulent. The authors argue that turbulent mixing layers will entrain more momentum from the freestream than the laminar mixing layer. Therefore the velocity profile across the mixing layer changes and a larger part will flow downstream. That lowers the reverse mass flow for a given base pressure, which is why the dashed curve is lower on the graph than the continuous one. Because for this example transition happens only just before reattachment, the scavenging mass flow curve is not influenced greatly.

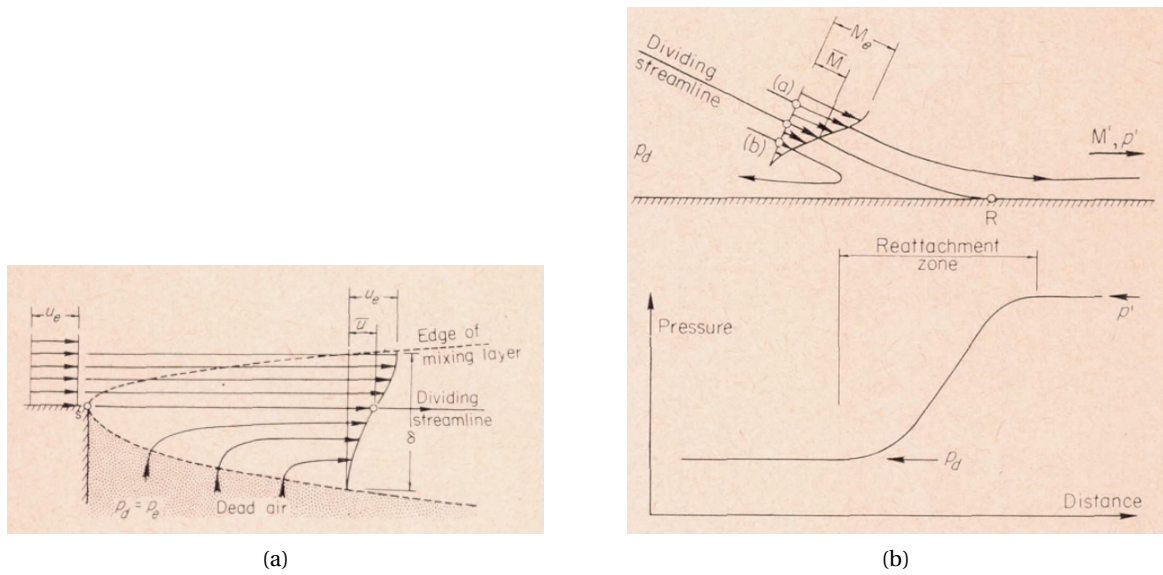


Figure 2.9: Impression of the flow at the separation point of a backward-facing step (a), and at the reattachment area (b). Figure taken from [12]

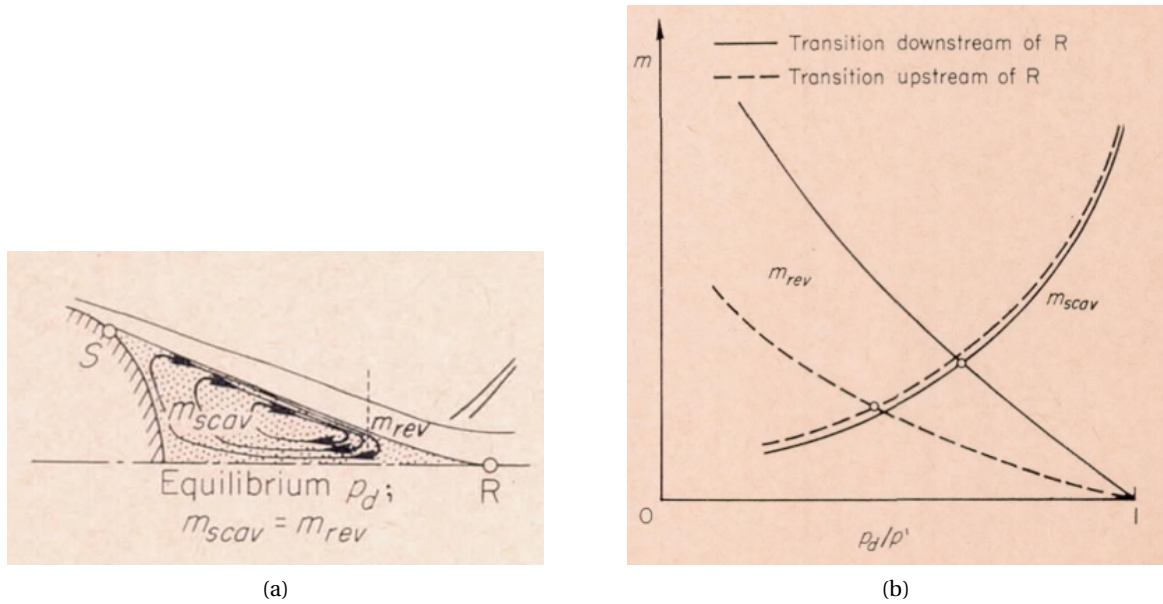


Figure 2.10: Impression of the mass flow equilibrium between scavenging mass flow, and the reverse mass flow at reattachment. Figure taken from [12]

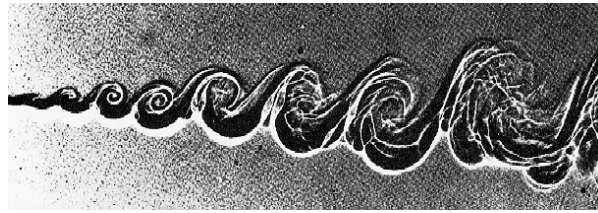


Figure 2.11: Shadowgraph of a turbulent mixing layer between Helium (upper stream) and nitrogen (lower stream). Image taken from [61]

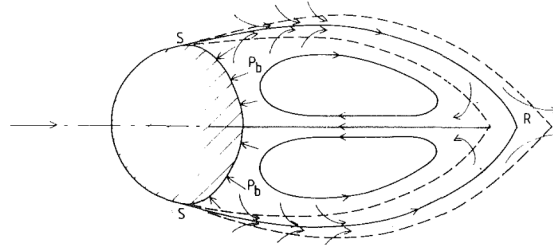


Figure 2.12: Impression of time-averaged wake behind a sphere.  $S$  indicates the separation point (line for 3D objects),  $P_b$  indicates the base pressure, and  $R$  indicates the reattachment point. Image taken from [4]

The two-dimensional backward-facing step discussed in the previous paragraphs illustrates the principles of the mixing layer and the way in which base pressure is lowered. To complete our conceptual understanding of bluff body wakes, one has to look at the three-dimensional flow, which is in some ways distinctively different.

First, the example of the backward-facing step shows a stagnation point that is impinged on a wall. In three-dimensional wakes, separating streamlines may converge mid-air, forming a free stagnation point. For two-dimensional flows with free stagnation points, i.e. flow separates on two sides of an object, strong vortex shedding may occur. The famous Von Karman vortex sheet which can be observed behind two-dimensional cylinders is one example. Such vortex shedding is linked to a significant drag increase. However, HDVs are inherently three-dimensional with a body aspect ratio (larger cross-wind dimension to smaller cross-wind dimension) of less than two. For such structures, vortex shedding still occurs but is less prominent than for two-dimensional bodies [4]. In fig. 2.12 a cross-section of the time-averaged flow behind an axisymmetric bluff body is shown, where separation occurs at points (or rather line)  $S$ . The mixing layer lowers the pressure in the near wake region, and thus the base pressure ( $P_b$ ), through the entrainment mechanism described earlier. The low pressure causes the mixing layer to deflect towards the axis of symmetry until it reaches a stagnation point which encloses the near wake. Similarly to the backward-facing step example, the fluid evacuated from the dead air by the mixing layer is balanced by reflux from the rear stagnation point. This motion creates the recirculation zones visible in the near wake. The recirculating zones should be seen as a ring-type, also called “toroidal”, structure when one considers its three-dimensional shape, see fig. 2.13.

On a separate note, the representations of wake flow as shown in this section resemble the average flow field in the wake. That is, the schematics show the flow speed and direction as averaged over a time frame much larger than that of temporal flow phenomena. Despite the previously stated observation that HDV wakes do not show strong shedding, separated wakes are inherently unsteady. A clear illustration of the difference between the average view of the flow and the instantaneous situation is shown in fig. 2.14. These figures are reproduced from [58], and they show the computationally simulated wake behind a GTS model. One can make out vortical structures in the mixing layer in the images of unsteady flow. These are reminiscent of the vortical structures as shown in fig. 2.11. The recirculation zone, obvious in the average flow field, is not easily distinguishable as such in the instantaneous flow field.

### 2.3.3. Forebody Drag

The front end of a simplified bluff body presents a somewhat simpler problem in terms of drag prediction and flow patterns. For most HDVs the front end is a flat surface, normal to the flow, with rounded edges. A region of stagnating flow is observed near the flat surface, and accelerated flow around is seen at the edges. However, the boundary layer that forms at the nose might separate at the edges, depending on the design of

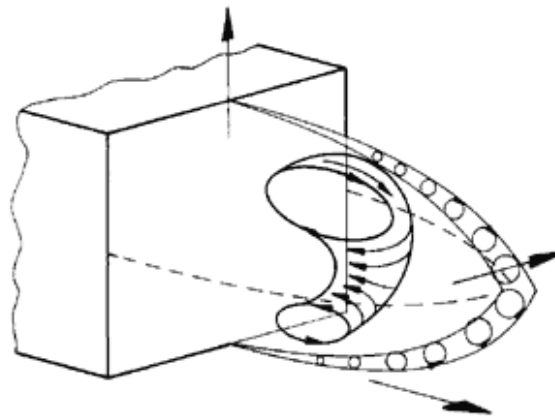


Figure 2.13: Separation behind a squareback vehicle model, schematic impression of time-averaged flow topology. Visible are the recirculation zone (ring-type vortex), and the mixing layer (small circles), which consists of coherent vortices. Figure taken from [36]

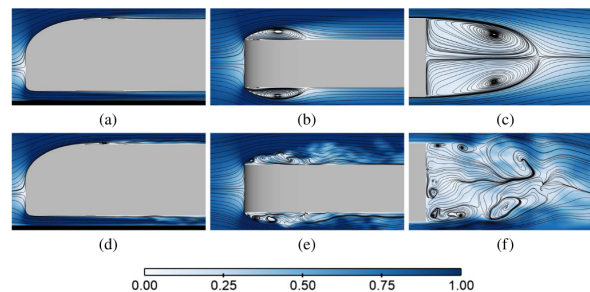


Figure 2.14: Normalized flow velocity and streamlines for time-averaged (a-c), and instantaneous (d-e) flow behind a GTS-type body. Figure taken from [58]

the edges and the local boundary layer velocity, and profile. In a study by Cooper [13], drag on simple road vehicles with varying edge curvatures was measured. The study found that the drag coefficient would change drastically for the same body based on the flow velocity. More specifically, three regions were defined in a plot of drag coefficient versus Reynolds number as seen in fig. 2.15: a subcritical, transitional, and a transcritical region. In the subcritical region, the drag coefficient decreases moderately with increasing Reynolds number. Beyond a critical Reynolds number, the slope of the graph steepens, and drag decreases further. This is the transitional region. Beyond the transitional region, the drag coefficient remains rather constant. It was observed that the subcritical region was indicative of separation bubbles at the rounded edges, which decreased in size until the transitional region. There, the flow would be attached and separate intermittently. In the transcritical region, the flow would remain attached at all times. It was found that this critical Reynolds number is constant when the typical length scale, on which the Reynolds parameter is based, was defined as the radius of the edge curvature, as shown in fig. 2.16. This result is not unexpected, as it is well known that at high Reynolds numbers boundary layers become more energized and that energetic boundary layers are better suited to negate adverse pressure gradients, such as those after the curved nose sections. Thus, at low Reynolds numbers, the flow would separate at the edges which caused frontal pressure drag. However, if sufficiently energized, the flow would remain attached. Once the flow was attached, increasing the Reynolds number did not improve the drag coefficient any further. It was also found in the study that using surface roughness to energize boundary layers it was possible to lower the critical Reynolds number.

Despite appearances, front end shapes that appear bluff can have surprisingly low drag coefficients, as long as no flow separation takes place. If one assumes potential flow, then any axisymmetric, infinitely extended front-end experiences zero drag [34, 71]. In fig. 2.17, Hoerner [34] has compiled an overview of some front-end shapes and their respective pressure drag based on experiments. The first three shapes confirm that sufficient curvature can lead to very low drag coefficients. Interestingly, the first shape even appears to produce negative drag, i.e. thrust. Looking back at the example of fig. 2.7, one can observe that the negative

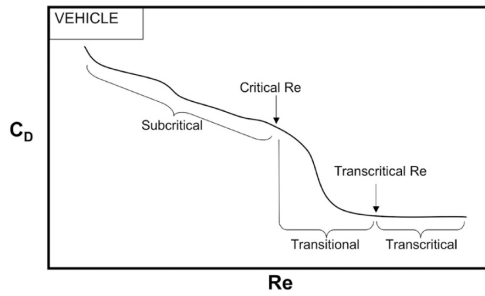


Figure 2.15: Typical drag coefficient behavior relative to Reynolds number for HDVs. Figure reproduced from [79].

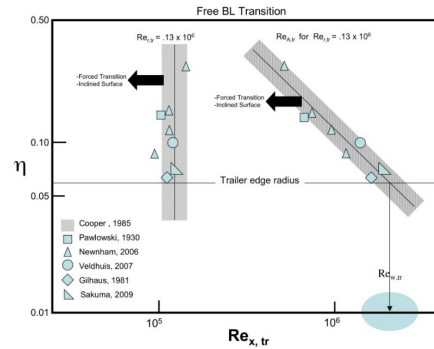


Figure 2.16: Edge radius  $\eta$  (radius/width) versus Reynolds number. Critical edge radius is given for either edge-based, or width-based Reynolds number (left, and right line respectively). Figure taken from [80].

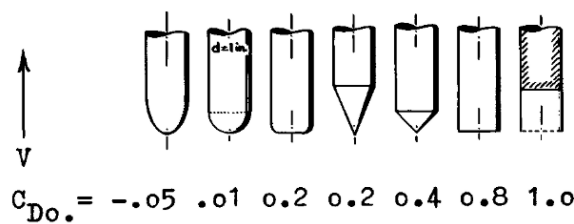


Figure 2.17: Pressure drag coefficients for a number of semi-infinite shapes. Figure taken from [34].

pressure over the corners of a bluff body will provide a thrust. As shown by Hoerner, this effect is significant, and can quite well balance the rearward pressure in the stagnation region.

Interestingly, there is an interaction between forebody drag and rear pressure drag that has been mentioned by [34, 36, 63, 77]. Any forebody drag will increase the boundary layer thickness before it separates at the base. For all HDVs under real-world driving conditions, one has to assume that the boundary layer at separation has a certain thickness, and is fully turbulent. According to [34], the separated boundary layer acts as an insulating layer between the near wake and the free stream, effectively raising the base pressure. The author has likened the flow around the recirculating wake and the entrainment of air from the base (although he does not reference entrainment explicitly) to a “jet-pump” which pumps away air [34]. In his analogy, the separating boundary layer acts as a “blanket”.

## 2.4. Toolbox: Coaxial Volumetric Velocimetry

Before advancing to the specifics of the aerodynamic characteristics of the Ahmed body, and the principles of drafting, we will take the time to introduce a powerful flow measuring technique. Its ability to visualize and quantify flow from wind tunnel experiments has been an important addition to the wind tunnel instrumentation toolbox. The following sections will elaborate on the concept of PIV, PTV, and CVV in general and the system used for the current work in specific.

Coaxial Volumetric Velocimetry is based on the concept of photographing particles in the researched flow domain and reconstructing their position and velocity through time. For illustrative purposes, the workings of a planar PIV system will be described first, and then the specifics of the Coaxial Volumetric Velocimetry (CVV) system used for this thesis will be explained. See fig. 2.19 for a schematic overview of planar PIV measurement and analysis. A general PIV system consists of a light source (commonly a laser), a high-speed camera, and a particle dispenser. Upstream of the domain of interest, particles (e.g. smoke) are introduced in the flow (e.g. by a smoke generator). The particles travel downstream with the flow towards the domain of interest. Here, a thin laser sheet illuminates part of the flow. The particles reflect the laser light, which is recorded by a camera placed obliquely to the laser sheet. The images are recorded at a considerable frame rate, such that images taken at consecutive time steps will picture many of the same particles. Employing computational correlation techniques, a subset of illuminated particles (interrogation window) can be matched across two consecutive images, and thus the velocity magnitude and direction of that subset can be reconstructed. Tomographic

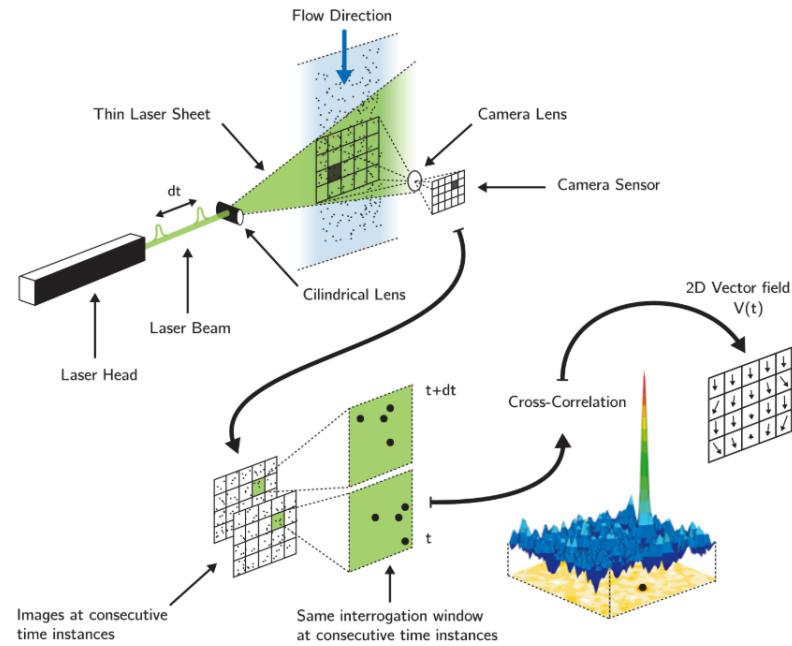


Figure 2.18: Schematic overview of a planar PIV system. Figure reproduced from [25]

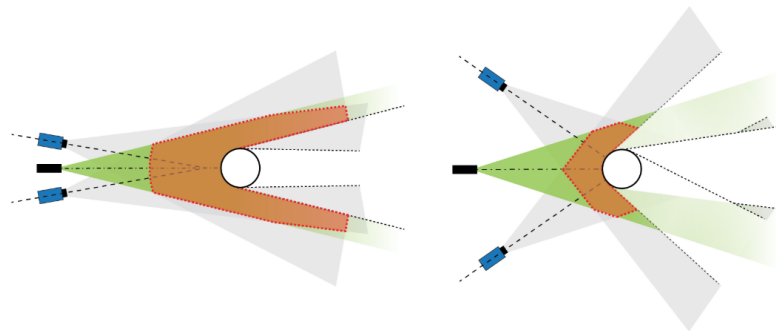


Figure 2.19: CVV (left) and typical Tomographic PIV (right) setups. The red area indicates the overlap between cameras and laser light. Figure reproduced from [25]

PIV increases planar capacity to reconstruct subset positions not just for one slice of the flow domain, but for a complete volume. The laser illuminates a volume, and three or more cameras are recording the flow. Therefore, a three-dimensional picture of the flow emerges.

The system used for this thesis was similar to the tomographic system described above but has been improved on a number of limitations. Most importantly, it improves the size of the illuminated volume and the processing speed. To increase the size of the illuminated volume two innovations have been crucial. The first is the introduction of Helium-Filled Soap Bubbles (HFSB). Accurate tomographic reconstruction requires well-lit particles. When the laser strength is limited, increasing the scattering of available lighting by increasing particle size has proven successful [64]. The HFSB particles are designed to be large, but also neutrally buoyant and capable of following the flow accurately. The second improvement has been the introduction of Coaxial Volumetric Velocimetry, where the laser is aligned with the cameras, rather than at a significant angle [66]. As shown in fig. 2.18, this increases the volume which is both illuminated and covered by the cameras. The proximity of cameras and laser head allow these part to be integrated into a single unit. When mounted on a robotic arm, as shown in fig. 3.5, the user gains the possibility of quick readjustment of the CVV system. After the robotic arm is calibrated at the beginning of experiments, there is no need to redo the calibration between different robot positions [40].

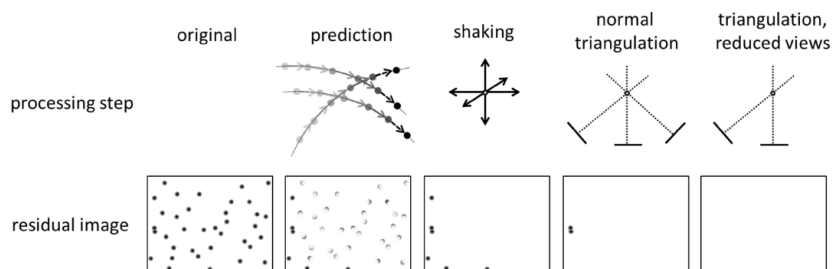


Figure 2.20: Schematic representation of the computational steps and their effect on the residual image, for one time step and one camera. Figure copied from [65]

Another significant improvement of the current system over some other three-dimensional flow reconstruction techniques is the relatively low computational cost of numerical processing. To that end, the current system uses an algorithm called Shake The Box (STB) to reproduce the flow domain from the images. In this algorithm, it is not the interrogation windows which are matched between time steps, but the individual particles. The term Particle Tracking Velocimetry (PTV), rather than PIV, would be more apt, although the complete system will be referred to as CVV from now on to emphasize the coaxial aspect. An intelligent predictor helps reconstruct the positions of the particles at the reduced computational cost compared to tomographic PIV, or even other particle tracking techniques. The STB technique works roughly as follows, but a full description can be found in [65]. For the first set of images in a data set, the software will triangulate some particles, but not all. Their tracks through space are reconstructed, by searching the true location at the next time step within a radius of a predicted location. The prediction can be based on the initial position and rough knowledge of the flow. When sufficient particles are tracked for a sufficient number of time steps, i.e. the initialization part is over, the intelligent predictor comes into play. For the tracked particles, the position in the next time step ( $t_{n+1}$ ) is estimated using a Wiener filter that uses the information of the previous position data (typically four previous time steps). The estimate is usually precise enough that slight spatial “shaking” of the particle will result in a match with the recorded image at ( $t_{n+1}$ ). The matched particles are removed from the images, and now the remaining particles are identified and tracks are constructed. The effort to find and track these remaining particles is less than in the initialization phase, as there are fewer particles left and velocity information of the resolved tracks will help in the position prediction. Thus, the system will keep converging until most particles are tracked, and the only new tracks are particles entering the domain. An overview of the steps described above is found in fig. 2.20. As one can see, there is a possibility that triangulation with all four cameras is not possible, perhaps due to overlapping particles from one perspective. Eliminating one camera perspective can help to create a clearer picture.

## 2.5. Wake flow past the squareback Ahmed Body

In 1984, in a paper by S.R. Ahmed et al. titled; “Some Salient Features Of The Time-Averaged Ground Vehicle Wake” [1], the aforementioned simplified vehicle shape is commonly known as the “Ahmed body” was introduced. The model was designed to investigate the separated flow behind the base of common road-vehicles. One of the features of the model is the variable base slant angle, see fig. 2.21. When slanted, the base produces a wake similar to that of passenger cars such as “hatchbacks” or “fastbacks”. At zero degrees slant, i.e. a vertical base area, the wake should be similar to that of any squareback vehicle of similar bluffness. Considering that a platoon of Ahmed bodies will be used for the current work as the subject of the experiments, it is worthwhile to review some of the latest publications concerning the Ahmed body wake topology, drag, and unsteady flow behavior.

In section 2.5, the time-averaged flow fields around a squareback Ahmed body are shown. The images have been reproduced from work by M. Grandemange et al. [27]. The flow fields have been recorded using planar PIV; the height-based Reynolds number was  $9.2e4$ . Although not explicitly visible in the images, the boundary layer separates just downstream of the front edges of the model due to adverse pressure gradients (see fig. 2.7). The separated boundary layers reattach further downstream along the body. The general wake topology is as expected from the description of wake flows in section 2.3.2. Both the top and side views show a pair of counter-rotating flows. In three-dimensional space, the recirculating regions are probably linked and form a toroid similar to fig. 2.13. Here, in the description of three-dimensional flow topology, a benefit of volumetric particle imaging techniques (CVV in particular) presents itself. See for example the research

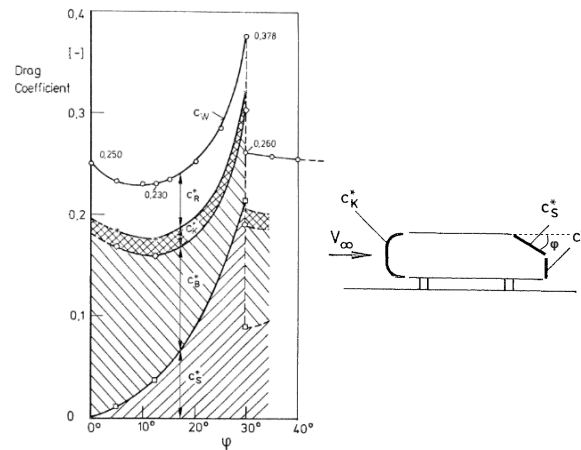


Figure 2.21: Ahmed body side profile, slant angle definition, and drag contribution of sections.

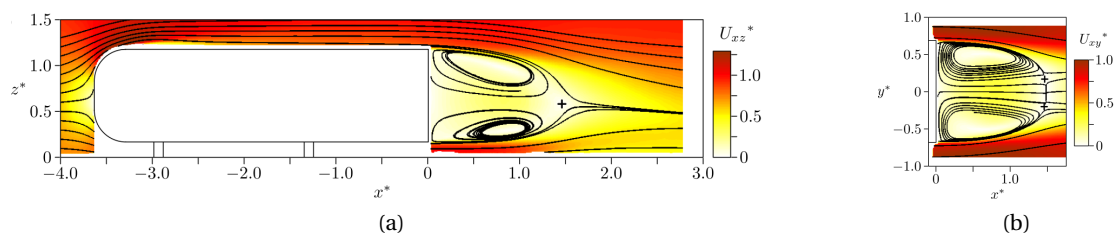


Figure 2.22: PIV recordings of the time-averaged flow field at the vertical center plane (a), and the horizontal center plane (b). Figures reproduced from [27].

of [25], in which the flow field around an Ahmed body with slanted rear has been reproduced (squareback Ahmed bodies were not tested). For an example of such a reconstruction, see fig. 2.23.

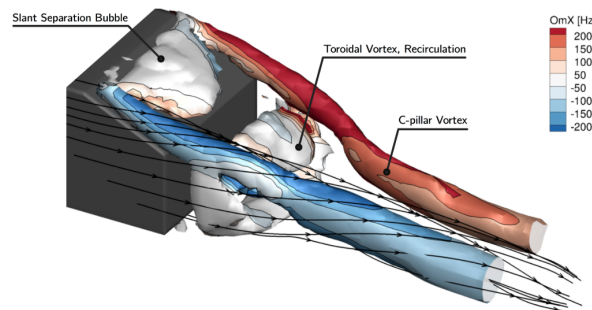


Figure 2.23: Vortex structures behind an Ahmed body with slanted rear. Acquisition done by means of CVV. Figure reproduced from [25]

Shedding of vortices from the mixing layer into the wake downstream of the recirculation areas has been reported by [17, 27, 56]. As shown earlier, shear layers roll up into vortical structures after separating. These vortices are then shed from the mixing layers periodically as shown in fig. 2.24 [17, 27]. After a vortex has been shed, the stagnation point momentarily moves upstream. This lowers the base pressure slightly. The stagnation point then travels upstream again until the next vortex is shed, which results in a “pumping” effect. The associated energy is low, according to [27], and thus it does not affect the drag of the Ahmed body much.

An interesting observation was made by Grandemange et al. in [26] about the stability of the average flow field in the near wake of a squareback Ahmed body. It was found that if one takes an average of the flow velocity of all recorded images, also called the global average, over a long time, the flow field in the horizontal plane appears symmetric; as was shown in section 2.5. However, if one averages over specific shorter time intervals, by means of conditional averaging, then one of two wake “states” becomes apparent. That is, samples that are allowed to form the average must satisfy specified conditions. An example of one such a conditionally averaged state is shown in fig. 2.25. The condition used for sorting the PIV results was based on the lateral position of the average wake momentum deficit. Another clear way to tell which of the

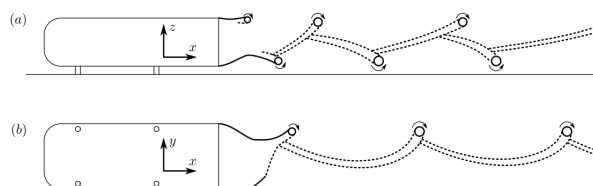


Figure 2.24: Oscillatory vortex shedding behind an Ahmed body. Figure reproduced from [58]

two states the near wake is in, is by measuring the lateral projection of the gradient of the pressure coefficient  $\frac{\partial c_p}{\partial y^*}$  at the backside of the vehicle at  $y = 0$ . A perfectly symmetric flow field would show a lateral gradient projection of zero, while an asymmetric state would yield a non zero gradient projection. In fig. 2.26 one can see that the switches between the pressure gradient sign happen randomly, and always resort to one of two steady values. The two states of the flow field are mirror images of each other across the  $xz$  plane at  $y^* = 0$  and both states are equally likely to be observed. Therefore a symmetric flow field is observed when PIV data is averaged over long enough periods. The switching between the modes is fast and appears to happen aperiodically. In the vertical direction, the pressure distribution remains constant, and thus in the vertical plane only one stable state exists. The condition of two stable wake states behind a bluff body which switch randomly has been termed bi-stability, and the states have been named reflectional symmetry breaking (RSB) states.

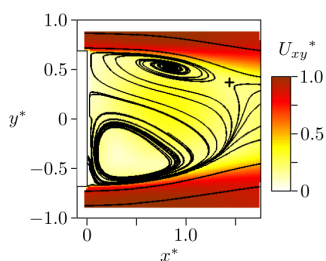


Figure 2.25: Conditionally averaged flow field behind Ahmed body, showing one of the bi-stable states. Figure reproduced from [27].

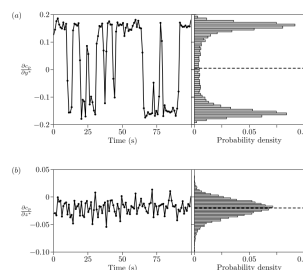


Figure 2.26: Pressure coefficient gradient across horizontal plane (a), and vertical plane (b). Bi-stability clearly visible for horizontal pressure distribution. Figure reproduced from [27].

In [28], the authors experiment with altering the Ahmed body wake dynamics using a thin cylinder, which is placed at various positions in the recirculation area. The wake could be forced to remain symmetric by placing the control cylinder in specific locations within the recirculation zone. By doing so, the pressure drag was lowered by 6%. Drag reductions were also measured for symmetric wakes behind another squareback geometry in [56]. The authors of [28] suggest that the bi-stable behavior alone might be responsible for anywhere between 4%-9% of the pressure drag on an Ahmed body. The source of the drag is likely related to the fact that the asymmetry of the bi-stable wake creates a lateral force on the vehicle, and thus influences the strength, position, and orientation of the vortex structure in the near wake [56]. The behavior of drag due to side force is not unlike that of drag due to lift on aircraft wings and has therefore been termed induced drag.

## 2.6. Drafting

In chapter 1 the concept of platooning as a method of improving road freight transport has been introduced. Among the mentioned benefits of automated position-keeping was reduced fuel consumption through the reduction of aerodynamic drag. How much can be saved, under what conditions, and why, remains an active field of research. The topic falls into a broader spectrum of research topics that deal with the aerodynamic interaction between two or more bluff bodies which is known as drafting.

### 2.6.1. Aerodynamic principles of drafting

Let us start by reconsidering the pressure field around a simple bluff body that resembles an HDVs: a high-pressure region is created over a large part of the front of the vehicle due to stagnating flow, while the near wake is of a pressure lower than ambient. Further downstream pressure is ambient, but flow momentum is low. Now let another vehicle approach the wake from far downstream. As the trailing vehicle approaches the

leader, it will progressively experience that the incoming flow carries less momentum than the freestream. Therefore, it will likely experience less drag. At the same time, the incoming low-momentum flow will stagnate at the front of the trailing vehicle, and thus static pressure will increase. The stagnated flow is of higher static pressure than would be seen far downstream of an isolated wake. Thus, the base pressure over the leading vehicle will increase, which means that the leading vehicle should experience a decrease in drag as well. Based on this basic description, one can intuitively understand the mutual benefit of drafting for vehicles in a platoon. However, let us return to the example of a bluff body in ideal flow. As shown in fig. 2.6, stagnation does not only occur at the front of the body but also at the rear. When placing two bluff bodies in tandem, the leading body will indeed experience a propulsive force, yet the trailing body will experience a drag increase [50]. The net drag of the combined bodies remains zero, as expected from d’Alambert’s principle. Therefore, it appears that at least two principles are at play when bluff bodies are platooning: there is the low-momentum wake interaction which should reduce drag for the trailing model, and there is the inviscid interaction of streamline curvature. In addition, the flow between the bodies is highly unsteady and turbulent, and thus the analysis of drafting aerodynamics is far from straightforward.

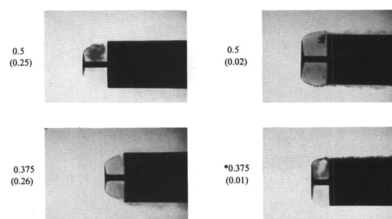


Figure 2.27: Smoke visualization of flow in gap between circular disc and semi-infinite cylinder. Non-bracketed number indicates gap width relative to cylinder diameter, bracketed number is the associated drag coefficient. Figure reproduced from [43].

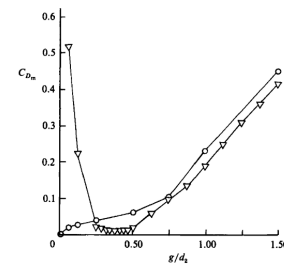


Figure 2.28: Drag coefficient  $C_{D_m}$  of plate and semi-infinite afterbody for range of nondimensional gap widths between plate and afterbody  $g/d_2$ . Front plate to afterbody diameter ratio  $d_1/d_2$  is 0.25. Triangles indicate sharp afterbody corners, dots indicate rounded corners. Figure reproduced from [43].

One of the earliest references to the idea of reducing the drag of HDVs by placing two bluff bodies in tandem can be found in the combined works [42, 43, 60]. The articles deal with fundamental flow phenomena and link these to practical applications, such as roof deflectors and drafting, only in passing. The results are nonetheless noteworthy. Essentially, the drag of a bluff body was lowered by placing a flat plate obliquely into the flow, just upstream, as shown in fig. 2.27. The flat plate was varied in size, and distance to the main body. The tests were repeated for two frontal shapes (axisymmetric and square). Drag was measured for the flat plate and afterbody combined. The measured drag coefficient was (to the surprise of the authors) notably lower than the unshielded afterbody. Note though, that the drag due to base pressure of the main body was intentionally not taken into account (the body was semi-infinite). The results show that even bluff bodies could approach the optimal forebody drag coefficients that have been studied by Hoerner (see again fig. 2.17). The authors identified a trend in minimum drag with respect to disk sizes and gap distances. They distinguish a sub- and supercritical region of low and high drag respectively. In a later paper [22], the authors return to the previous findings and mention that the sub and supercritical regimes could be better termed, self-sustained oscillation type, and wake type flows respectively. The self-sustained oscillation type flows coincide with significant drag reductions as compared to the wake type flow. Its name is due to the measured oscillatory behavior of the shear layers which are important to maintaining a low drag coefficient [22]. One other aspect of the experiments of [42, 43, 60] that is worth mentioning, is the influence of edge rounding on the drag coefficient. The pictures in fig. 2.27 show a main body with sharp edges, which has been the subject of the bulk of the work, but an experiment smaller in scope has been reported too where the main body edges were rounded (radius based Reynolds number was  $6.25 \times 10^4$ ). The graph in fig. 2.28 shows that the rounding of the edges lowers the drag coefficient compared to the square-edged case only for small gap sizes, for larger gap sizes the drag coefficient is higher than it would be with sharp edges. Note also that the semi-infinite body with rounded edges and without upstream disk ( $g/d_2$ ) has a drag coefficient of 0.01, which means that the frontal disc increases the drag coefficient in the absolute sense in all cases. The authors suggest that reattachment of the separated shear layers spoils the propulsive effect of the rounded corners, but they do not elaborate on this suggestion.

In the work of Hammache and Browand [32], a more practical setup is tested in a wind tunnel experiment. First, the authors looked at the tractor-trailer gap, next they extended their experiment to platooning. Scale

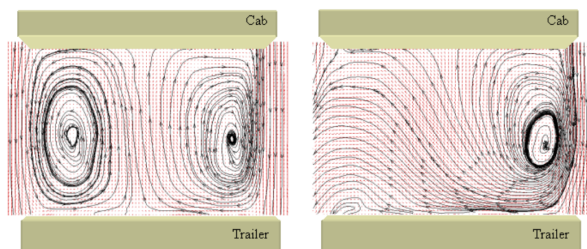


Figure 2.29: Conditionally averaged flow fields in tractor-trailer spacing for gap distance of  $0.55G/\sqrt{rtA}$ . Symmetry breakdown has been linked to steep drag increases. Figure reproduced from [32]

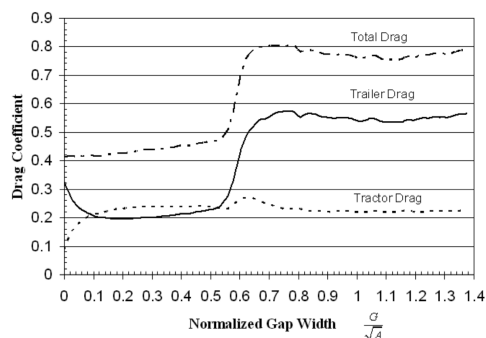


Figure 2.30: Drag Coefficient of tractor, trailer, and combination for a GTS-type wind tunnel model, for a range of tractor trailer gaps. Figure reproduced from [32]

models were used for the tractor-trailer gap experiments, while simpler models with no tractor-trailer gap were used for the drafting tests. Drag measurements showed that closing the tractor-trailer gap decreased vehicle drag while increasing the spacing led to a notable drag rise around the normalized separation distance of .55, see fig. 2.30. This relative distance is similar to that found in [22] for transition from self-sustained oscillation to wake mode. The authors have made snapshots of the instantaneous flow field between the trailers using PIV measurements. The images, shown in fig. 2.29, indicate that the dramatic drag rise is related to the stability of cavity recirculation flow. In the range between 0.55-0.75 intermittent breakdown of symmetry is observed. At larger separations, the flow becomes symmetric again, but drag remains high.

The authors of [32] extend their research to two HDVs in tandem, by testing all possible combinations of a simplified truck shape with either rounded or square front end corners. Care was taken that the front end rounding was sufficient, such that the flow would stay attached. The results are shown in fig. 2.31. Again, two regions are discerned, this time called strong-interaction, and weak-interaction regions. Noteworthy is pronounced drag rise in the crossover between weak and strong interaction regions. Furthermore, it is curious to see that, when both models have rounded fronts, the leading vehicle can experience less drag than the trailing model (in the weak interaction region). The authors provide a possible explanation: for well-rounded fronts, most drag stems from the base. Therefore, any improvements in the base drag yield relatively high benefits, while the trailing model, with its already aerodynamic front, sees less benefit from the wake.

The influence of corner radii on the effectiveness of platoons is further investigated in a CFD experiment that has been reported in [24], and the associated MSc thesis [23]. The contributions of front, sides, and base to the overall drag of a GTS type vehicle were separated for convenient analysis. The study shows that trailing vehicles might experience reduced suction at the front corners, which leads to diminished savings. In isolated conditions, the well-rounded corners at the front provide suction, which counteracts the stagnation pressure over the center front part, see for example figure fig. 2.7. When immersed in the wake of the preceding vehicle, the suction diminishes due to the curvature of streamlines between the vehicles [24], see fig. 2.32. While the overall momentum in the wake is lower than ambient and therefore the stagnation pressure is reduced, the reduction of the suction peak can be the dominating effect at close separation distances. In the study, the trailing vehicle of a three-vehicle platoon actually experienced higher drag than it would in isolation.

In an experimental campaign that utilized both force measurements and CVV measurements, the flow topology in the region between two simplified HDV shapes was studied by [72]. Figures of the average flow field at different separation distances are shown in fig. 2.33. From a visual standpoint, the difference be-

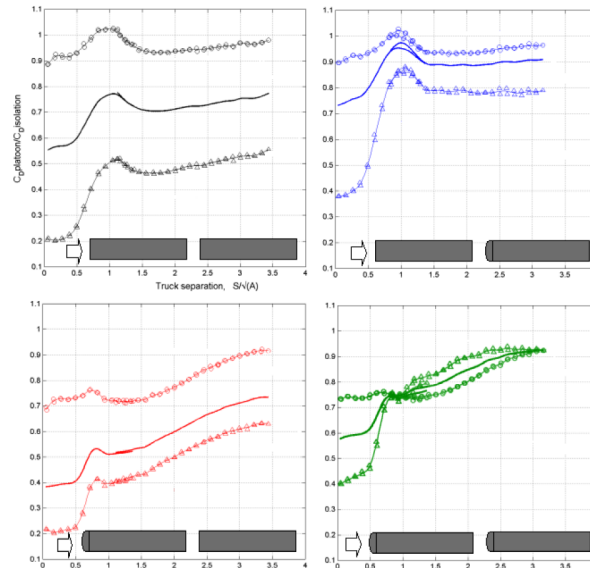


Figure 2.31: Drag coefficients of leading (o), and trailing ( $\Delta$ ) models in a platoon. Figure reproduced from [32]

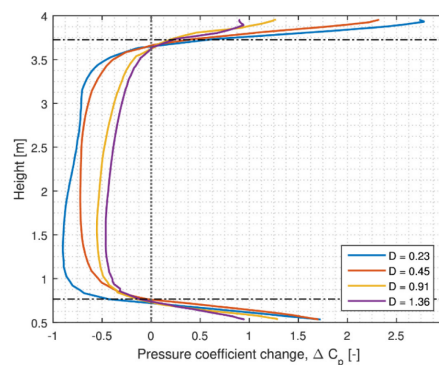


Figure 2.32: Pressure coefficient difference along front end of GETS model, vertical midplane location. Nr.2 vehicle in platoon,  $D$  indicates the normalized separation distance  $\text{Gap}/\text{Length}$ . Pressure coefficient difference defined as difference between #1 vehicle and #2 vehicle pressure coefficient ( $c_{p_{lead}} - c_{p_{mid}}$ ) at equal locations on the front end contour. Figure reproduced from [24].

tween short separation distances and the larger separation distance is mainly in the shape and location of the recirculation area. For the small separation distance, the shear layers bridge the gap between the models without turning into it much. The streamlines suggest that the shear layer stagnates somewhere on the curved edge. In the case of sharp edges the shear layer can “lock-on” to the downstream edge if separation distance is small enough (indicative of self-sustained oscillation) [22]; whether the lock-on also occurs for rounded edges is unclear. For the larger separation distance, the shear layers form a closed loop around the recirculation zone. Drag was measured for a range of corner radii, and a drag increase over the value in isolation was measured for the models with large corner radii. That is, models which had low drag coefficients due to streamlined front-ends experienced a drag penalty while drafting in the trailing position. Although front surface stagnation pressure decreased, the loss of propulsive force over the rounded edges resulted in a net increase in drag.

### 2.6.2. Agreement between field tests and other experiments

Concurrently with wind tunnel and CFD research of HDV drafting, a number of field tests have been carried out in order to investigate the fuel-saving potential of platooning. Among the experimental campaigns are those with COE type trucks [2, 8, 73, 78], and regular trucks [6, 10, 44, 48, 49, 54].

One could summarize the results of the field tests as follows. First, fuel consumption is reduced for leading and trailing vehicles in a close-spaced convoy, as compared to the vehicles driving in isolation. This is clearly the result of reduced aerodynamic drag. Second, to minimize the combined fuel consumption of all

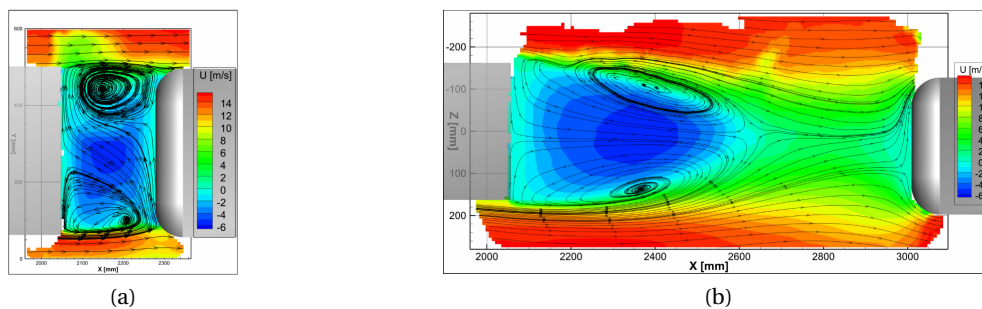


Figure 2.33: PIV recordings of the time-averaged flow field at the horizontal center plane at 0.63 vehicle widths longitudinal separation (a), and 2.84 vehicle widths longitudinal separation (b). Figures reproduced from [72]

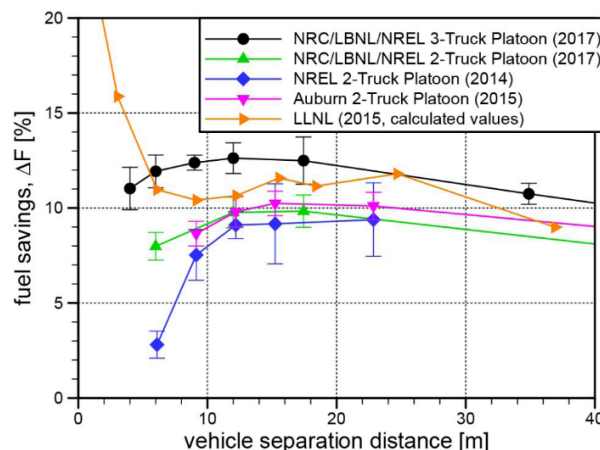


Figure 2.34: Comparison of fuel savings for trailing vehicle in 2- and 3-vehicle platoons in several field test studies and one WT experiment. Figure reproduced from [47]

vehicles in the platoon, the inter-vehicle spacing should be as short as possible. Third, the trailing vehicle does not show a monotonic reduction of fuel consumption with decreased following distance. These conclusions appear to be universal and somewhat independent of specific truck design (although some variation exists).

Most researchers seem not to have expected the fuel consumption behavior of the trailing vehicle. Several hypotheses have been proposed to explain a perceived anomaly [10, 44]. Interestingly, when most of the field tests were conducted, not much fundamental research on HDV drafting other than that described in [32] was available. The models used for those tests were highly simplified and therefore might not have been perfectly comparable to start with. Perhaps it is not surprising that the field tests would yield fewer savings than sterile wind tunnel tests. It is, however, important to investigate what exactly causes the difference, and what can be done to make the most out of the potential of drafting. This issue has been recognized by the researchers that have performed the field tests, and some comparative studies are available.

The National Renewable Energy Laboratory (NREL), which produced the field test study described in [45], has compiled a number of wind-tunnel and field tests, in order to investigate how well these two agree. The same has been done in [47]. In fig. 2.34, the fuel savings for comparable field tests and one wind tunnel test are compared side-by-side. The wind-tunnel drag figures have been transformed into potential fuel savings by means of assuming friction drag at a representative vehicle weight and speed. As seen before, all trailing vehicles seem to experience diminished savings at following distances closer than 15 meters. Yet, there does not seem to be a satisfactory explanation for this effect. Interestingly, the wind-tunnel experiment shows an erratic trend that matches the onset of diminished savings between 8-15 meters, after which the fuel savings increase strongly at separation closer than 8 meters. This would suggest that the diminished savings are a natural occurrence of the interaction effects between a realistic regular cab tractor and the back-end of a squareback trailer.

Of the possible explanations for decreased performance at close separation from [10], “control dither” and increased engine temperatures seem unlikely. The field test of [6] provides evidence that improved control algorithms do not change the fuel consumption of the rear vehicle significantly. The engine temperature was

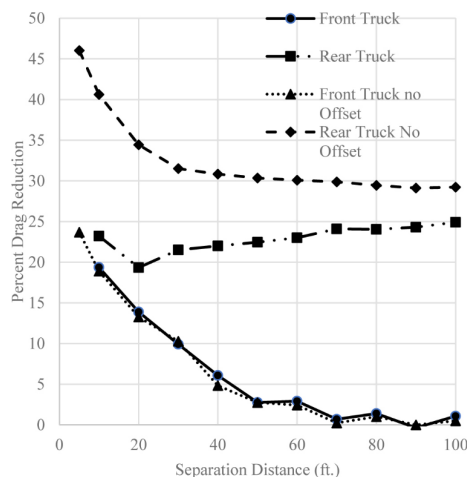


Figure 2.35: Drag reduction for regular cab tractor-trailers for two vehicle platoons that are aligned, and laterally staggered by 2 feet (0.6 meters). CFD results. Figure reproduced from [37].

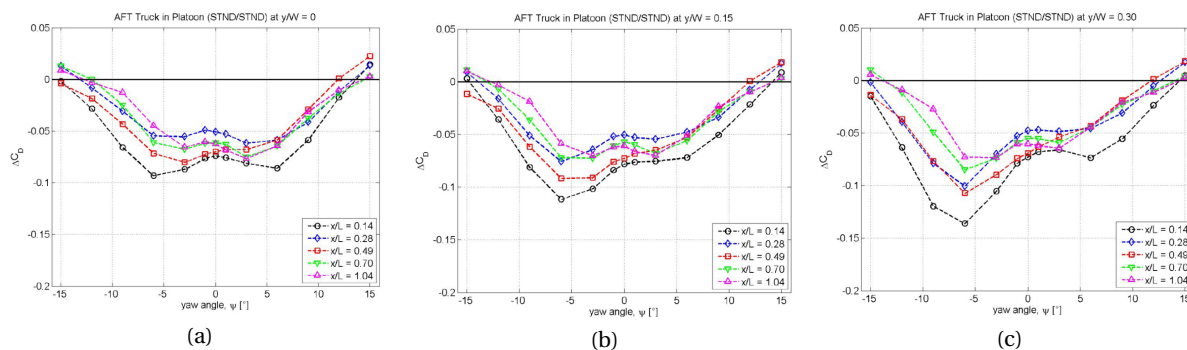


Figure 2.36: Yaw dependant drag coefficient improvements for aft truck in two-vehicle drafting of regular-cab tractor-trailers. WT experiment. Figure reproduced from [47]

monitored and does not correlate with diminished savings, as was previously thought.

### 2.6.3. Lateral Stagger

The notion that HDVs which are platooning in traffic will not be as nicely aligned as wind tunnel experiments or CFD tests, is considered in [10]. The researchers visually observe that lateral misalignment is in the order of  $\pm 0.5$  meters. Data on lateral offsets are not reported for all field tests, but some do mention it. In [6], GPS data is used to assess lateral offset. Although high precision data is corrupted, the data that was available shows that at close separation distances, offsets of more than  $\pm 0.3$  meters are unlikely. In these tests, the lateral control was done by human drivers. For the research of [74] (COE tractors), the vehicles were equipped with lane-keeping systems. Lateral wandering was reduced to  $\pm 6$  centimeters lateral offset.

From these observations, one can conclude that lateral offsets in the field were relatively small. Naturally, when automatic lane-keeping is not on, the offsets are fully dependant on the skill and concentration of the driver. This might mean that in commercial applications, with tired or less experienced drivers, lateral offsets could be greater than mentioned. Therefore, it is relevant to investigate how sensitive drafting HDVs are to lateral offsets.

CFD research by [37], shows that aligned trucks with regular cabs will experience a monotonic drag reduction when separation distance decreases. However, at two feet lateral offset, the trailing vehicle's drag reduction becomes worse. The trend, shown in fig. 2.35, resembles that which has been seen in the field tests. Smaller lateral offsets had little effect on the drag coefficient. It must be mentioned that the CFD simulations were Reynolds averaged (RANS), and therefore transient behavior was not considered.

Lateral offset conditions in HDV drafting have been investigated in at least two wind-tunnel experiments. Both of these tests involved regular-cab tractor-trailers. The first experiment was done with 1/50 scale models [62]. The width-based Reynolds number for the tests was  $2.65e5$ . The tests showed that neither the leading

nor trailing model was affected by lateral offsets of up to 0.5 vehicle widths. The tested separation distances were 9, 15, and 49 meters of full-scale distance, the drag coefficients were wind-averaged. A similar conclusion was drawn in [48]. For those experiments, two regular cab tractor-trailers of 1/15 scale were tested at width based Reynolds numbers of  $8.5e5$ . A selection of aerodynamic add-ons was applied to the models to test their effect on drafting performance. The wind-averaged drag coefficients do not show much dependence on lateral stagger up to 0.3 vehicle widths (situation in which the vehicles are at opposite edges of 3.7-meter wide lane). Interestingly, the yaw-dependant drag coefficient does change notably with such offsets. In fig. 2.36 the drag coefficient for a platoon of standard (STND) trucks (no aero-modifications) is shown. One can clearly see that the figures lose their symmetry with lateral stagger. Furthermore, the variation in drag appears to become larger with decreasing following distance, e.i. the aft vehicle becomes more sensitive to within lane offsets.

The study also makes an important observation about the wind-averaged drag coefficients of trailing vehicles: for some configurations, the drag reduction is not monotonic with separation distance. It seems that the applied aerodynamic modifications can shift the point of maximum savings, which means that the shortest separation distance may not be the optimal position for the trailing vehicle. As has been the case before, the combined drag coefficient of lead and aft vehicle is always lowest at the shortest distance. The non-monotonic behavior appears to agree with the earlier field tests of [5, 10, 44] according to the authors of [48]. Therefore, it is less likely that lateral offsets caused the diminished savings at some close distance. It is rather the specific geometry of the vehicles that is responsible for the non-monotonic drag decrease. The precise relation between vehicle geometry and flow field is not discussed in the article.

There does not appear to be similar research into the effect of lateral stagger on drag for COE type tractor-trailers. An indication of the possible effects might be found however in an unintentional alignment error in [72]. This author's experimental campaign consisted of CFD, and wind-tunnel measurements of two GETS (similar to GTS) models in drafting. According to the author, the wind tunnel alignment was difficult due to the size of the models and mounting equipment. Vertical and lateral misalignment was noticed in some cases, and to quantify the effect it might have had, the offset was simulated in CFD. For a leading model that was positioned lower by 0.03 vehicle height than the aft model, the aft model experienced a considerable drag rise of 0.046 drag counts (0.344 isolated value). The longitudinal separation distance was 0.63 vehicle widths. The leading model did not experience any significant changes in the drag coefficient. The main cause of the increased drag of the aft model was the increased pressure at the exposed edge. Although this case of misalignment is not the same as lateral stagger, it might give an indication of the sensitivity of COE type tractor-trailers to lateral misalignment, considering that the tested offset was very subtle.

## 2.7. Research Plan

After analyzing the current state of the research field of HDV drafting, the motivation and objective of the presented thesis are formulated in the following section. A brief discussion of the method in which the research questions are to be answered is provided, such that the choice of the experimental setup of the next chapters becomes clear.

### 2.7.1. Objective

The survey of available literature in the preceding sections has shown that expectations of fuel savings from platooning do not always match field tests. Several potential causes are brought forward, yet none are proven conclusive. The suspicion that lateral misalignment (also called lateral "stagger") of the vehicles is detrimental to the savings, and might be correlated with crosswind, has so far only been studied for realistic regular-cab truck models. The topic of misalignment is therefore not fully exhausted yet. There have been no studies that investigate the COE type tractor in misalignment scenarios, and an analysis of the flow topology for any laterally misaligned platoon of HDVs appears to be missing. It is therefore desirable to approach the issue of misalignment from a fundamental perspective, such that general conclusions can be drawn which might be applicable to a wider range of vehicles. The objective of the presented research is aimed at answering the following questions, and thus deepening the understanding of HDV drafting under certain conditions:

*What is the influence of lateral offset on the flow topology between two squareback Heavy-Duty Vehicles while drafting?*

Including the following sub-questions:

- How does the drag coefficient of a platoon of Heavy-Duty Vehicles change for realistic combinations of stagger and separation distances?
- What is the pressure coefficient distribution at the base of the leading vehicle in a platoon for realistic combinations of stagger, and separation distances?
- How are the drag and pressure distribution linked to the flow topology between the two bodies?

### 2.7.2. Methodology

To answer the research questions, new data needs to be gathered, as there is insufficient information currently available. There are three types of experiments that can be used for aerodynamic research into HDVs; field tests, wind-tunnel experiments, and CFD experiments. Field tests are rather unsuitable for the current study, due to atmospheric disturbances and the inability to visualize flow topology. Even if atmospheric disturbance or visualization is not an issue, the aerodynamic drag can only be found by approximation, because other sources of drag such as rolling friction cannot be measured directly. More suitable would be computational or wind-tunnel environments. Both have been employed successfully in drafting research, as can be seen in the previous chapter. Both approaches have their strengths and weaknesses, a discussion of which is beyond the scope of this thesis. Suffice it to say that with CVV measurements, many of the possibilities for flow visualization and quantification that had before been the domain of CFD, are now available in the wind tunnel. The choice to use wind tunnel measurements for this research rather than computational methods was based on the extensive experience of the supervisors in the domain of CVV measurements.

The size of the available wind-tunnel (cross-section of the jet is 0.6x0.6 meters) necessitated the use of small-scale models. Scaled models can be good representatives of full-scale vehicles as long as one accounts for the effects of decreased Reynolds number. In deciding the actual size of the vehicles and the range of experiment variables separation, yaw and stagger, two other aspects besides the Reynolds number were of importance. The first is the blockage factor; that is, the ratio between the frontal area of the model and the test section. It should preferably be kept as low as possible. Second is the length of the platoon. The open-jet tunnel creates mixing layers at the edges of the jet, which widen downstream. The effective length of undisturbed air is therefore limited. The lateral stagger should represent realistic driving conditions without moving too close to the edge of the jet.

The choice of model type, model size and experiment variables was subsequently the subject of a short trade-off study. An important boundary condition was that the wind tunnel speed was limited by the CVV system. Therefore, one would desire a model with large leading edge radii to maintain sufficiently high local Reynolds numbers. Thus, a wide and high model would be necessary. However, as mentioned above, a small blockage factor is preferred to minimize wind tunnel interference effects. The result of the trade-off was that half-scale Ahmed bodies would be the most suitable objects. Radius based Reynolds numbers are similar to other experiments with Ahmed bodies ([29, 41]), and the models are shorter w.r.t. their cross-sectional area than GTS/GETS models, which means that for a given test section length larger separation distances can be tested. The wake is nonetheless expected to be similar to that of HDVs.

# 3

## Experimental Setup

The following chapter consists of three parts. The first part describes the wind-tunnel and the Ahmed body models. It further provides an overview of the experiment variables. The second part deals with the instruments which were used to observe the experiment. Lastly, an overview of the data acquisition and processing techniques is given.

### 3.1. Setup

#### 3.1.1. Wind Tunnel

The experiment has been performed at the w-tunnel at the faculty of Aerospace Engineering of the TU Delft. This is an open circuit wind tunnel, which features an open test-section and interchangeable nozzles. The throat area of the nozzle used for this experiment was  $0.6 \times 0.6 [m^2]$ . Key information about the wind tunnel is summarized in table 3.1. Jet velocity is controlled manually by setting the rotational speed of an upstream fan. Dynamic pressure is measured in the throat with a single pitot tube. A digital readout provides the pressure in Pascal. The fan speed is adjusted until measured dynamic pressure is close to the desired value. The pressure readout has been observed to fluctuates approximately within one Pascal. Temperature and ambient pressure are recorded before every test, so freestream velocity can be deduced from the dynamic pressure measurement.

Technical Data	
Type	Open test-section
Nozzle area	$0.6 \times 0.6 [m^2]$
Contraction Ration	4 [-]
Turbulence intensity (seeding rake installed)	1%

Table 3.1: Technical details of the W-tunnel at the TU Delft.

#### 3.1.2. Scale Model Construction

Two squareback Ahmed body models were designed and built specifically for the presented wind tunnel experiments. The models are referred to as model #1, and model #2. Both models had the same outside dimensions. The main difference is that model #1 was equipped with pressure taps, while model #2 was not. The design of the models was mostly dictated by the available load cells, see section 3.2.1 for specifications of the latter. Previous load cell users warned for the possibility of excessive vibration of the model while positioned in the freestream. This was particularly clear for setups in which the load cells were placed at distances of more than 20 centimeters away from the center of force application, e.g. when the load cell is under the floorboard. Tiny elastic movement of the load cell surface to which the model was attached resulted in visible vibrations at the model, and therefore likely to erroneous force readings.

To mitigate the issue of vibration, it was decided to mount the load cells inside the vehicles (see fig. 3.1), and to keep the models lightweight. The central mounting position decreased the moments exerted by the

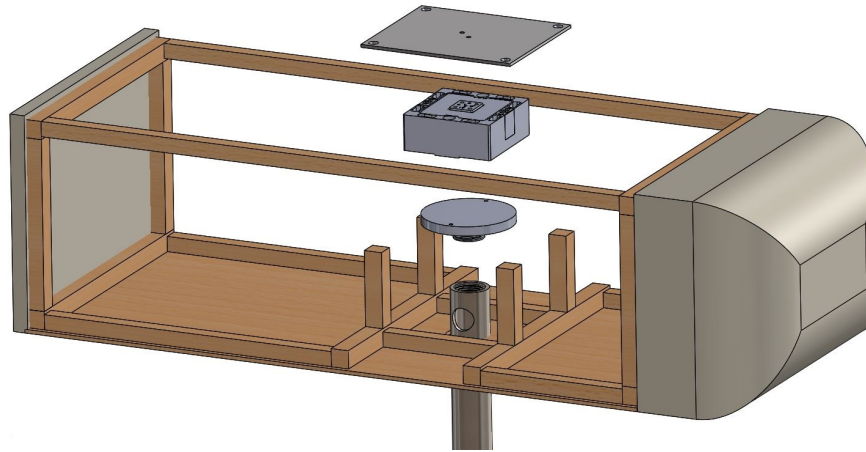


Figure 3.1: Exploded view of Ahmed body internal structure and load cell. Body panels not shown.

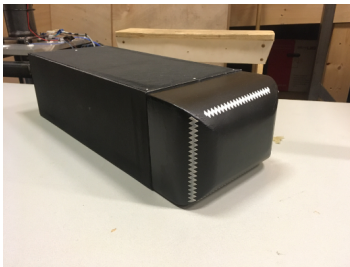


Figure 3.2: Image of model #2 with ZigZag strips applied.

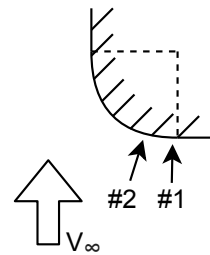


Figure 3.3: Schematic representation of ZZ strip position relative to the corner radius. Arrows indicate locations for models numbered #1 and #2, respectively.

model on the sensor and reduced the movement of the model for a given flexible inclination of the sensor surface. Additionally, a low mass moment of inertia increased the natural frequency of the sensor-model system, which reduced the likeliness of resonance during testing.

The internal structure of the models was built from light woods such as balsa and pine. The bottom surface was made of plywood. The sides and top were made from foam sheets (Graupner Vector boards), which were reinforced with pine stringers. The nosecone was made from a grainy, brittle, foam type, which lent itself to sanding. The edges were rounded with a wooden scraper of the appropriate radius. The nosecone was then covered in protective adhesive film. The structure and panels were glued together, except for the topside panel. This panel was used as an inspection panel for mounting/dismounting the load sensor and connecting/disconnecting the pressure taps. The entire model was painted black to minimize reflections during CVV measurements. ZigZag (ZZ) tape, which is used to trip laminar boundary layers into turbulence, was placed on the four corners of the nose cone for both vehicles. Unbeknownst that the longitudinal placement was critical for the ZZ strips to work effectively, as will be discussed in section 4.1, the location differed between the models. The location of the ZZ tape application is shown in figs. 3.2 and 3.3. The dimensions of the model are given in table 3.2. Manufacturing of parts and subsequent assembly was performed manually. Some dimensional differences between the models exists and are in the order of one-to-two millimeters. The precision of the nose curvature is more difficult to assess, but considering that the nose sections were sanded into shape by hand, some differences between the two examples should also be expected.

Over the rear face of Ahmed body #1, 16 holes were drilled for pressure taps. To each hole, a piece of steel pipe with a diameter of 0.3 millimeters was connected. The pipes were mounted flush with the rear surface. Plastic tubing connected the pipes to the pressure measurement device. The distribution of pressure ports is shown in fig. 3.4.

Unlike the original Ahmed body, which was mounted to the floor by four pegs [1], the scaled models have been mounted on a single central pole which was connected to a frame beneath the floorboard. The load sensor was attached to the top of the pole. The model was then bolted to the top of the load sensor (again,

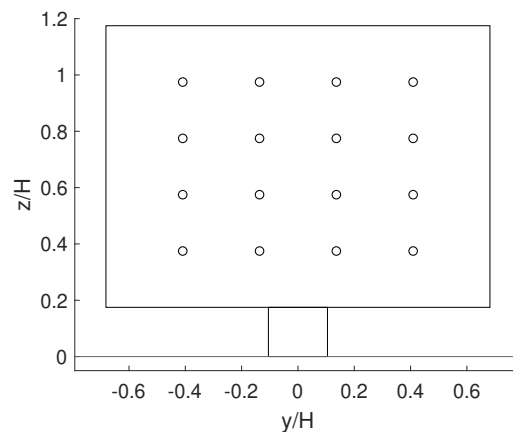


Figure 3.4: Pressure port (o) locations across rear face of model #1. The coordinate system is vehicle based, and normalized by model height  $H$ .

see fig. 3.1). The reason for using this mounting system was the flexibility it offered to move and rotate the models in the test section. Additionally, the single hollow pole allowed for convenient routing of the pressure tap tubing to the pressure scanner beneath the floorboard. The downside of the single-pole setup was that the new Ahmed bodies would have different underbody flow compared to the reference cases in literature. The outside diameter of the mounting pole is 30 millimeters.

Scale w.r.t. original Ahmed body	1/2 [-]
Length	522 [mm]
Width	195 [mm]
Height	143 [mm]
Nose curvature radius	50 [mm]

Table 3.2: Basic dimension Ahmed body scale models.

### 3.1.3. Experiment Lay Out

In the rendering of fig. 3.5 the setup of the models, robotic CVV, and floorboard is shown. These elements were attached to a single rigid frame. In that way, after calibrating the robotic arm, the position of the base of the arm would remain set. To decrease interference effects between the CVV head unit (also called *MiniShaker*) and the models, the former was kept outside of the projected jet area.

The floorboard was made such that the trailing model could be moved laterally without dismantling either the model or floor. To that end, three oval slots were created, each at one predefined separation distance. The model had to be partially dismantled only to change the separation distance. A side- and top view of the test section with the models in place is shown in fig. 3.7. Note the reference system orientation. The position of the leading vehicle was constrained to a single circular slot, the trailing vehicle was positioned in one of the three oval slots. Both models could be yawed in their slots by twisting the support poles. Slots that were not in use were closed with tape to maintain a continuous and smooth ground plane. The upstream edge of the floorboard coincided with the nozzle exit plane. The floorboard was elevated around 50 millimeters above the lower nozzle exit, rather than flush with the nozzle. This was due to the distribution of HFSB particles in the jet, as it appeared during initial testing that there were insufficient particles around the lower part of the Ahmed bodies. Elevating the floorboard has a detrimental effect on the blockage factor, which will be discussed in section 3.3.4. The models were positioned 25 millimeters above the floorboard, which is in accordance with the scaled height above the ground plane as tested by [1].

## 3.2. Instrumentation

### 3.2.1. Load Sensors

To measure the drag, lift, and side forces on the Ahmed bodies, two load sensors were used (one per vehicle). The sensors are K3D60's, manufactured by ME-Meßsysteme. They are three-axis sensors that measure forces

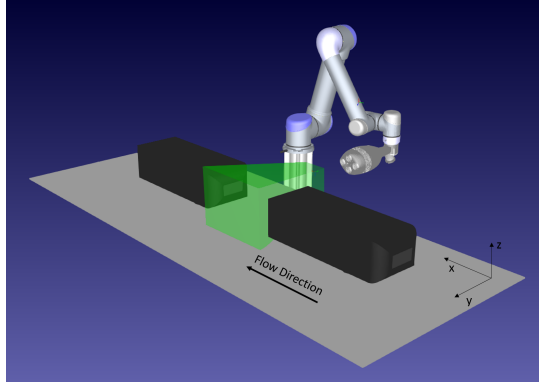


Figure 3.5: Rendering of Ahmed bodies, floorboard, and robotic arm with *MiniShaker* as installed in the wind tunnel. The green cone represents the illuminated volume that is recorded by the cameras in the *MiniShaker*.

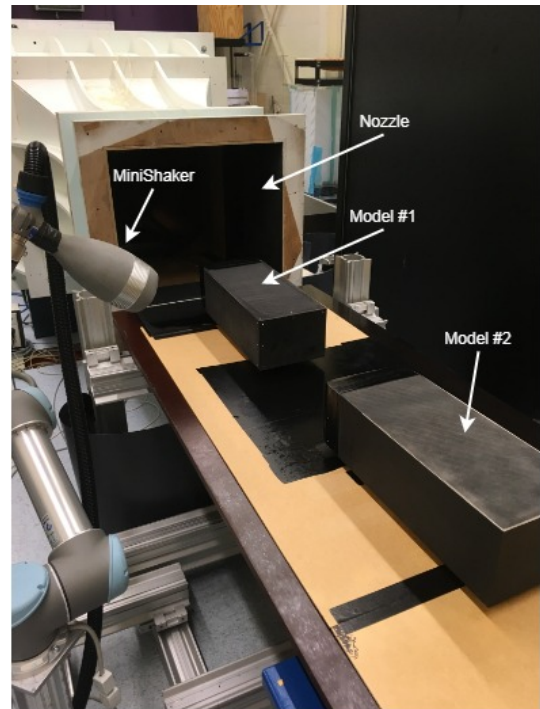


Figure 3.6: Image of test-section with annotations of models, *MiniShaker*, and nozzle.

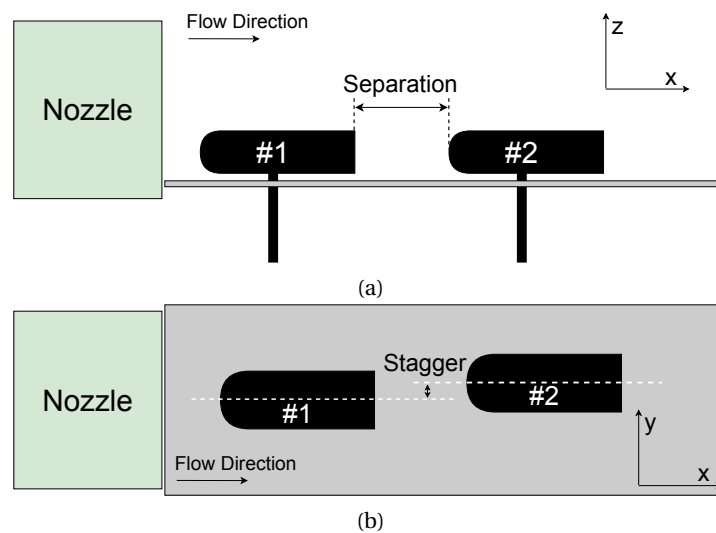


Figure 3.7: Ahmed bodies in test section, side view (a), and top view (b). Definition of separation and stagger.

in 3 perpendicular directions. Moments are not measured, and their influence on force readings are limited by design. Load measurements are based on internal strain gauges. An overview of the most important features is shown in table 3.3.

Technical Data	
Full Scale (FS) rated output	$\pm 10$ [N]
Accuracy Class	1%
Influence of eccentric load to FS	1% [FS/50mm]
Crosstalk at rated load (x to y, y to x, or z to x/y)	2% [FS]
Rated output per axis	0.5 [mV/V/FS]

Table 3.3: Technical details of K3D60 load cells.

The load cells are connected to separate amplifiers. The calibrated sensitivity of the load cells, i.e. [N/mV/V], is stored on the amplifiers. Data is recorded through dedicated software called GSVMultichannel available from the company website, which combines the readouts of both amplifiers to one file. The acquisition frequency for the experiments was 500 Hz.

### 3.2.2. Pressure Ports

Pressure measurements on the model were done with the use of a pressure scanner by Nub Systems. The system allows for 16 pressure taps to be connected at once. The pressure scanner measured the differential pressure between the ambient air in the plenum chamber, and the pressure tap at the model. The sensor, which was located beneath the floorboard, was connected to the pressure taps with flexible tubing. The tubes were about one meter in length.

Acquisition software allowed for continuous or average measurements, based on the user request. In continuous mode, the scanner can scan each port at 2 kilohertz. The range of pressure differential that could be measured was  $\pm 160$ Pa. A summary of technical specifications can be found in table 3.4. These results are copied from an internally available technical report.

Technical Data	
Full Scale Span (FSS) pressure range	$\pm 160$ [Pa]
Total error band	$\pm 2.5\%$ FSS
Resolution	0.022 [Pa]
Measurement Frequency	2 [kHz]

Table 3.4: Technical details of Nub Systems pressure scanner.

### 3.2.3. Coaxial Volumetric Velocimetry

For inspection of the flow domain between the platooning Ahmed bodies, a Coaxial Volumetric Velocimetry (CVV) system was used. The general principles of particle tracking have been presented in section 2.4. The following is a more detailed description of the specific instruments that have been used here.

The seeding rake that expelled the Helium-Filled Soap Bubbles (HFSB) in the jet consists of 200 nozzles which are spread over 10 streamlined struts and cover an area of approximately 50 centimeters in width and 95 centimeters in height. Unfortunately, some of the nozzles appeared not to be working during the experiments. According to the author of [72], who used the same seeding rake for an earlier experiment, 25 nozzles had been blocked off already due to their malfunctioning. The number of faulty nozzles has probably risen in the meantime. The lack of nozzles reduced the uniformity and the seeding density of the HFSB in the jet. The seeding rake was placed in the settling chamber, as opposed to after the nozzle, to minimize turbulence production. As such, the stream of bubbles it generated was contracted by the nozzle to approximately 25 by 47 centimeters width and height respectively. Compressed air, helium, and soap, which are required to produce the HFSB, were supplied through a Fluid Supply Unit that was built by *LaVision*. As stated in table 3.1, the wind tunnel freestream turbulence is less than 1% with the seeding rake installed (based on internally available documentation).

The four cameras which record the particles and the optical lens which disperses concentrated laser light

in a conical volume are combined in a single device. This device is called the *MiniShaker* and has been built by *LaVision GmbH*. The device is housed in an aerodynamically shaped casing and is coupled to a robotic arm. The laser which illuminates the particles is generated by a *Quantronix Darwin Duo Nd:YLF* unit and sent to the *MiniShaker* through an optical fiber.

The robotic arm which is used to move the *MiniShaker*, and thus the illuminated volume, provided six degrees of freedom. The arm was built by *Universal Robots*; type *UR5*. Position and orientation of the arm are set either directly by the dedicated controller, or through an interface with *DaVis 10* and *RoboDK* software. *DaVis 10* is the image acquisition and processing software, and *RoboDK* allows the user to position the robotic arm in a virtual environment. Robot positions that have been predefined in a virtual environment can be uploaded to the robotic arm before image acquisition.

### 3.3. Data Collection and Processing

#### 3.3.1. Test Plan

Two design variables have been varied for the platoons during the experiment: the separation distance (expressed in percentage of model length  $L$ ), and the lateral stagger (expressed in percentage of model width  $W$ ). For tests with the models in isolation the positions were kept constant, but the yaw angle (expressed in degrees) was changed. To limit the time required in the wind tunnel, a grid with a discrete number of design variable combinations has been selected. The limits of the variables were selected based on literature research, blockage effects, and instrument precision. Furthermore, all tests were done under similar conditions, which are summarized in table 3.6.

The variable matrix presented in table 3.5 presents all possible combinations of variables that can be tested, given that the yaw angle is set at zero degrees. To make the most of available time and resources, these measurements have been divided into subsets. The subsets have been based mostly on the restrictions of measuring pressure and force at the same time, and on the likely accuracy of the CVV measurements.

The load and pressure measurements are the least time demanding. Apart from properly aligning the vehicles, no further preparation is needed after the instruments have been connected to computers for recording. Therefore, it was possible to test many of combinations of variables in little time. Note that the load measurements of the leading model could not be done at the same time as the pressure measurements. The reason being that the flexible tubing exerted a loading on the model and and support pole, and therefore limited the sensor movement. For correct measurements, the only load path from model to the support pole should go through the load cell, and not the tubing. This meant that the load and pressure measurements were done separately.

The CVV measurements required more preparation and processing time, and therefore a scarcer test matrix was assembled. Based on the assumption that left and right misalignment would be symmetric, it was decided to mainly observe misalignment to one side. The force and pressure measurements would have to prove that there is indeed symmetry between the cases. Furthermore, only the outermost positions were tested. That is, only the closest (20%  $L$ ) and furthest (60%  $L$ ) separation distances were tested in combination with (0%  $W$ ) and the leftmost (-25%  $W$ ) lateral positions.

Sep. Dist. / Lat. Offset	-25%W	-15%W	0%W	15%W	25%W
20%L					
40%L					
60%L					

Table 3.5: Experiment variables. Yaw angle is 0°. Green cells indicate that only pressure and force measurements have been performed. Red cells indicate the pressure, force, and CVV measurements have been done.

Freestream velocity	13-14 [m/s]
Width based Reynolds Nr.	1.8e5 [-]
Height based Reynolds Nr.	1.3e5 [-]
Radius based Reynolds Nr.	8.8e3 [-]

Table 3.6: Experimental testing conditions.

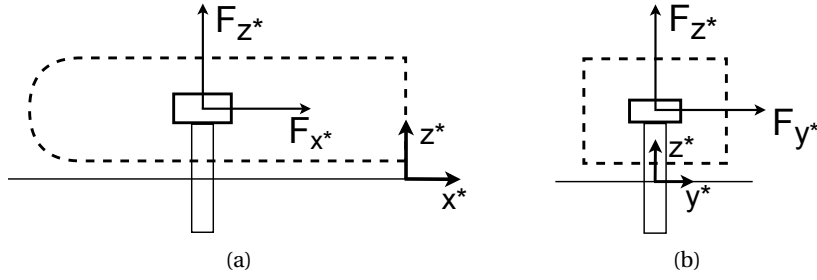


Figure 3.8: Force vectors and body oriented reference system on Ahmed body. Side view (a), and rear view (b). Lower solid line indicates floor.

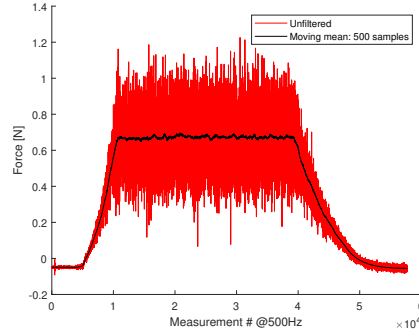


Figure 3.9: Unfiltered load cell signal versus signal that has been averaged over 500 data points using a moving mean. Baseline and target force are easily distinguishable after averaging.

### 3.3.2. Force Coefficients

To compare force and pressure measurements between test setups and literature, the results have been converted to coefficients. First, let us define the orientation of force measurements. Because the load sensors are mounted rigidly in the vehicles, it is convenient to express the forces in the vehicle reference frame, see fig. 3.8. The latter reference frame will be indicated by an asterisk (\*), to distinguish it from the general reference frame (such as shown in fig. 3.7). The units of distance in the body mounted reference frame will be related to the characteristic length of the model, namely the height  $H$ . Therefore,  $x^* = x/H$ ,  $y^* = y/H$ , and  $z^* = z/H$ . The force coefficients are calculated as shown in eq. (3.1), where  $\rho$  is the air density,  $A$  is the frontal area of the model without the support pole ( $A = 27.90 \times 10^{-3} \text{ m}^2$ ),  $v_c$  is the corrected jet velocity, and  $q_c$  is the corrected dynamic pressure. For the correction of dynamic pressure measurements, see section 3.3.4 and appendix A.

$$C_{x^*} = \frac{F_{x^*}}{\frac{1}{2}\rho v_c^2 A} = \frac{F_{x^*}}{q_c A} \quad C_{y^*} = \frac{F_{y^*}}{\frac{1}{2}\rho v_c^2 A} = \frac{F_{y^*}}{q_c A} \quad C_{z^*} = \frac{F_{z^*}}{\frac{1}{2}\rho v_c^2 A} = \frac{F_{z^*}}{q_c A} \quad (3.1)$$

The direct signal provided by the load sensors during operation was quite noisy, as is shown in fig. 3.9. The unfiltered signal covers a wind-tunnel measurement from start in “off” condition, the ramp-up to desired dynamic pressure, steady flow at desired dynamic pressure, and return after shutdown. From the unfiltered signal it is difficult to judge precisely when these phases start or end. Therefore, for all measurements, a moving mean filter has been applied to aid in defining the time at which each phase starts and ends. The effect of filtering is also shown in fig. 3.9. The filtered images are easier to analyze. For every measurement a “baseline” region, and a “target” region were identified manually. The baseline is the mean force reading when the wind tunnel is initially “off”. The target is defined as the mean force reading when the wind tunnel is set at the desired freestream velocity. The difference between the means of both “baseline” and “target” signals is defined as the net force. This is similar to zeroing the load sensor before each measurement.

### 3.3.3. Pressure Coefficients

Pressure measurements are normalized using expression eq. (3.2), for which  $p_\infty$  is the static freestream pressure,  $\rho$  is the air density,  $V_c$  is the corrected air velocity, and  $p$  the static pressure at the pressure port. The pressure sensor measures the differential pressure between the pressure taps and ambient pressure at the

sensor which is positioned away from the jet, i.e.  $\Delta p_{measured} = p - p_{room}$ . One would expect that the ambient pressure at the sensor and that of the jet are equal because the test section is open. However, as will be shown in section 3.3.4, the measured freestream static pressure  $p_\infty$  in the undisturbed jet was slightly higher. Thus, the measured pressure at the taps across the Ahmed body is not equal to  $p - p_\infty$ . The reason for this discrepancy is not known, but the difference is rather consistent throughout the test-section. Therefore, for all pressure coefficient calculations it was assumed that  $p_\infty - p_{room} = 4[Pa]$ , and thus  $p - p_\infty = p - p_{room} - 4[Pa] = \Delta p_{measured} - 4[Pa]$

$$c_p = \frac{p - p_\infty}{\frac{1}{2}\rho V_c^2} \quad (3.2)$$

For further analysis of the pressure distribution across the rear face of the Ahmed body, the lateral projection of the gradient of the pressure coefficient will be used. More specifically, the lateral projection of the gradient  $\partial C_p / \partial y^*$  at the  $y^* = 0$  location. A simple, central finite difference method is used, which is shown in eq. (3.3). The step size  $h^*$  is equal to half the non-dimensional lateral distance (in  $y^*$ ) between two pressure ports, i.e.  $h^* = 0.14[-]$ .

$$\frac{\partial C_p(y^* = 0)}{\partial y^*} \approx \frac{C_p(y^* + h) - C_p(y^* - h)}{2h} \quad (3.3)$$

### 3.3.4. Wind Tunnel Corrections

While full-scale HDVs drive in the open air, the Ahmed bodies of the presented experiment operate in a jet of air of finite cross-section which interacts with the static air in the plenum, as well as the nozzle and collector itself. The result is that force and pressure measurements can be over- or underestimated when compared to models in the open air. It is therefore common practice to apply correction methods to wind tunnel results, to compensate for interference effects. To this end, the research by Mercker, Weidemann, and Wickern [52, 53] provides a clear approach for correcting measurements in open test-section wind tunnels for automotive applications (and high blockage ratios). In short, the correction procedure consists of superimposing multiple factors that take into account individual blockage effects as well as deviations in the static pressure distribution in the jet. A more complete explanation of the method can be found in appendix A. For the current study, one of the main goals of the correction procedure should be to identify any effects that will cause measurement differences based on the longitudinal position in the jet alone. To make meaningful observations based on the relative longitudinal position between the models, one must find out which differences are due to drafting effects, and which are due to wind-tunnel interference. Interference effects based on lateral position have not been taken into account.

Nozzle area	0.6x0.6 [ $m^2$ ]
Effective Nozzle area*	0.6*0.55 [ $m^2$ ]
Ahmed body + pole extension frontal area	0.0288 [ $m^2$ ]
Blockage at 0% lateral misalignment	8.7 [%]

Table 3.7: Wind tunnel correction data. \*= Nozzle area minus area blocked by floorboard.

The corrections in the method of [52] can be divided into two parts: one part is related to blockage effects, and the other part is related to the streamwise pressure gradient in the empty jet. The full correction is formulated as:

$$C_{D_{cor}} = (C_{D_m} + \Delta C_{D_{HB}}) / (q_{cor} / q_\infty) \quad (3.4)$$

For which  $\Delta C_{D_{HB}}$  is the drag coefficient correction due to static pressure distribution in the empty jet (also called ‘‘Horizontal Buoyancy’’ hence the subscript), and  $q_{cor} / q_\infty$  is the dynamic pressure correction due to blockage. The terms  $C_{D_{cor}}$ , and  $(C_{D_m})$  denote the corrected and the measured dynamic pressure respectively.

Blockage effects can be interpreted as all wind-tunnel interference that causes streamlines to divert from their ideal path, i.e. their path in an infinite jet with no nozzle or collector present. The blockage correction is applied by scaling the measured dynamic pressure. The corrected dynamic pressure is then used to make results non-dimensional; such as drag or pressure coefficients. For the dynamic pressure correction, the so-called ‘‘Nozzle-method’’ correction will be applied. It assumes that dynamic pressure is measured using a static pressure differential between the settling chamber, and one or more pressure ports in the nozzle. In

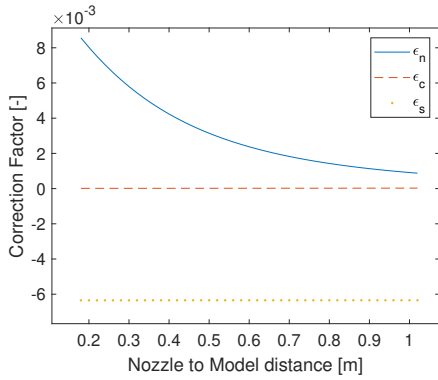


Figure 3.10: Correction factors at a range of test section locations.

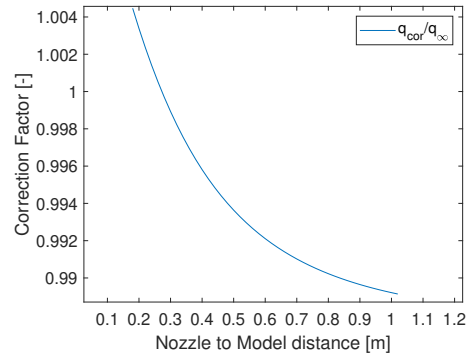


Figure 3.11: Complete dynamic pressure correction at a range of test section locations.

the w-tunnel, the dynamic pressure is measured with a pitot-tube in the nozzle, a method that is not covered explicitly in the correction procedure of [52]. However, the “Nozzle method” correction should be the most applicable, as is explained in more detail in appendix A. The full dynamic pressure correction is thus:

$$q_{cor} / q_{\infty} = (1 + \epsilon_S + \epsilon_C + \epsilon_N)^2 \tag{3.5}$$

For which  $\epsilon_N$  is the velocity perturbation due to nozzle blockage,  $\epsilon_S$  is the velocity perturbation due to jet expansion, and  $\epsilon_C$  covers collector blockage. The floorboard, which was elevated above the lower nozzle exit, was modeled by reducing the nozzle area by the area blocked by the raised floor. The principal blockage conditions can be found in table 3.7.

The graph that is shown in fig. 3.10 displays the individual corrections for a range of positions of a single Ahmed body in the test section. As can be seen, the corrections are most noticeable close to the nozzle. The main effects here are the nozzle blockage and jet expansion. The collector blockage is of minor importance due to the relatively large size of the collector, and its location far downstream.

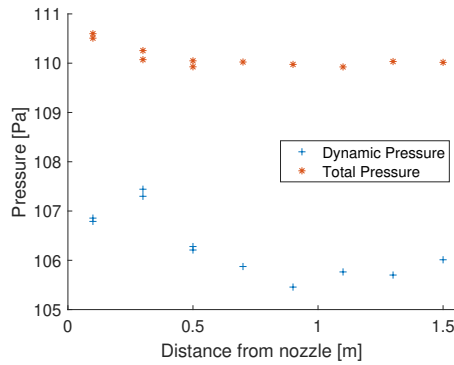


Figure 3.12: Total and dynamic pressure in centre of empty jet (floorboard installed). Dynamic pressure in nozzle set to 106 [Pa]. Pressures are relative to plenum chamber static pressure.

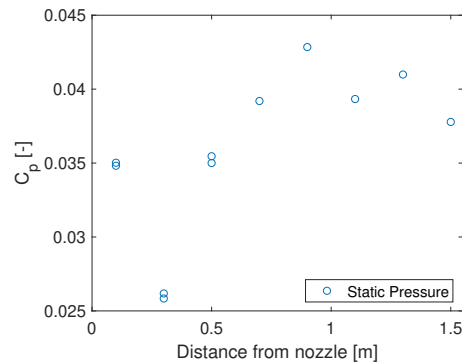


Figure 3.13: Pressure coefficient distribution in in centre of empty jet (floorboard installed). Reference pressure is equal to plenum chamber pressure, dynamic pressure used for non-dimensionalizing is local dynamic pressure.

Concerning the horizontal buoyancy correction: if there is a streamwise pressure gradient in the jet when no model is present, then according to [53] it may be assumed that the same pressure distribution applies when the model is placed in the jet. Therefore, the front-end and rear-end of the model could experience slightly different pressures, on top of the pressure distribution caused by the model itself. The pressure gradient correction is applied directly to the measured drag coefficient and is also known as the “Horizontal Buoyancy” correction. A plot of the static and dynamic pressures in the center of the empty jet, with floorboard installed, can be found in fig. 3.12. These results were obtained by placing a pitot-static tube in the empty jet at a range of locations. Overlapping measurements at the three locations closest to the nozzle confirm the consistency of the measurements. The pitot measured total pressure and static pressure relative to

the plenum chamber static pressure (away from the jet). Dynamic pressure was then obtained by subtracting the relative static pressure from the relative total pressure. The figure shows that total pressure remains fairly constant as should be expected with no model installed. Therefore, to satisfy the Bernoulli equation, dynamic pressure changes are equal and opposite to the static pressure (coefficient) changes, as can be seen in the right-hand part of fig. 3.12. At all stations, a higher than ambient static pressure was measured. The measurement at 0.3 meters from the nozzle is notably lower than the two nearest measurements, which hints at a local interference-effect. Around the mentioned location two beams (used to mount the floorboard) extended above the ground plane (visible in fig. 3.6). Although these beams were outside of the projected nozzle area, they could have interacted with the jet mixing layer, which caused the local increase in flow velocity.

With knowledge of the static pressure coefficient distribution throughout the empty jet and the size and position of the models, the full correction can be obtained (as per appendix A). A summary of the correction factors is presented in table 3.8. These corrections apply to the vehicle positioned at the location mentioned in the first column, given that the full platoon is installed in the test section. That is: one model should be in the leading position, its nose 0.18 meters from the nozzle exit, and the trailing model at one of the three other positions.

Nozzle to model front-end distance	$q_{cor}/q_{\infty}$	$\Delta C_{D_{HB}}$
0.18 [m]	1.0045	0.0117
0.81 [m]	0.9902	-0.0007
0.91 [m]	0.9896	-0.0041
1.02 [m]	0.9892	-0.0047

Table 3.8: Dynamic pressure and horizontal buoyancy corrections per model station.

### 3.3.5. Image Processing and Flow Field Analysis

Image acquisition and processing were managed with *LaVision* software *Davis 10*. Around 10,000 images were shot for each position of the *MiniShaker* to obtain sufficient images for statistical convergence of flow information. The maximum acquisition frequency of the cameras is 511 Hz at the full sensor resolution of 800x600 pixels. Taking into account the freestream velocity and the size of the illuminated volume, a higher acquisition frequency was required such that average particle displacement between frames would not become too large. The STB routine may have trouble correctly recreating particle tracks if the displacements between two time-steps become too large [25]. To increase the acquisition frequency to 700 Hz, the resolution of the cameras was cropped to 700x420 pixels.

After acquiring sufficient images of laser-illuminated Helium Filled Soap Bubbles, the images need to be processed to translate the data into a three-dimensional flow field. The first step is the correction of the raw images. Correction here means reducing background noise that exists due to reflections and camera noise. To minimize reflections, the Ahmed bodies and the floorboard were painted in a matt black color. Despite the effort, some reflections are bound to remain. For most data sets, a single High-Pass Butterworth filter was sufficient to reduce noise due to reflection to acceptable levels. This method of image filtering in CVV applications has been pioneered by Sciacchitano and Scarano in [67]. The High-Pass Butterworth filter decreases the intensity of steady and slow-moving reflections, while fast-moving reflections are left unchanged. Therefore, passing particles remain in the processed images, while stationary or slowly oscillating background reflections are minimized. The filter was constructed over a moving window of 7 images. However, in some cases, vibrations of the model caused fluctuating reflections that the Butterworth filter would not clean from the raw images. An image cleaning strategy originally proposed by [39] was used for these cases. The strategy consists of the following procedure. A visual representation is shown in fig. 3.14 (a-d).

1. The standard deviation of the pixel intensity of a set of raw images is calculated and stored.
2. Another copy of the same raw images is first filtered with a Gaussian filter to reduce noise, and then by a High-Pass Butterworth filter to repress unwanted reflections.
3. The map of pixel intensity standard deviation is multiplied with a small coefficient. It is then subtracted from the filtered images. The result is a single set of images with minimal noise due to reflections. The coefficient should be chosen such that after subtraction noise is filtered, but particle information remains sufficient. The coefficient used in this thesis was 0.083.

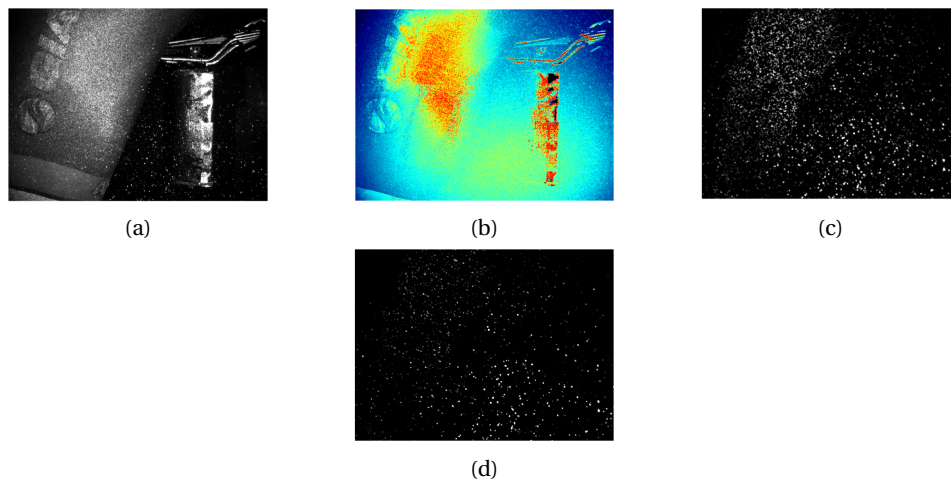


Figure 3.14: Processing of image with fluctuating background reflections. (a) Raw image, (b) RMS of intensity, (c) Gaussian and Butterworth filter applied to (a), (d) final result (image (c) minus a scaled version of image (b)). Images reproduced from [39].

In the next step of post-processing, filtered images are analyzed with the Shake The Box routine, which has been covered in section 2.4. The result is a three-dimensional field of particle tracks at each time step. Finally, the instantaneous particle field is transformed into an average flow field. This is done by spatial averaging, also known as “binning”. The user defines the size of three-dimensional cuboids (bins) and a script averages velocity magnitude and direction of particles that pass through the bin. For the results presented in this thesis a minimum number of 50 tracks must have passed through a bin before its average velocity value is considered statistically converged. Unconverged bins are left blank. The binned data is processed in *Tecplot 360* to create visuals that can be analyzed.



# 4

## Results

In the following chapter the results of the experiment that is described in chapter 3 are presented. The results are organized by instrumentation type. The final section of this chapter is a discussion of the results in light of earlier research, as described in chapter 2.

### 4.1. Force measurements

The following sections will cover the drag and side forces on the models in isolation and in the platoon. For a description of the load sensors and data analysis approach see, sections 3.2.1 and 3.3.2.

#### 4.1.1. Isolated Ahmed Body

As discussed in section 3.1.2, the two Ahmed bodies in the platoon are labeled #1 & #2. In all platooning situations, vehicle #1 was the lead model. However, the models were tested in isolation as well, to obtain baseline values for later comparison. When the models were tested in isolation, they were placed in the “lead” position (i.e.: the front of the models was 18 centimeters from the nozzle exit). For measurements presented in this thesis, the drag of the support pole is not measured because the sensor is placed inside the models, on top of the support. Interference drag between model and support is not taken into account.

	Model #1	Model #2
Sample size $n$	$n = 4$	$n = 7$
$C_{x*}$	$0.28 \pm 0.01$	$0.25 \pm 0.01$
$C_{y*}$	$0.07 \pm 0.01$	$0.06 \pm 0.04$

Table 4.1: Mean drag ( $x^*$ ), and mean side force ( $y^*$ ) coefficients for isolated Ahmed bodies. The  $\pm$  values indicate the standard deviation of the sample of means.

In table 4.1, the mean drag, and side force coefficients of the models in isolation are presented. The drag of model #1 is between that reported in [27] (i.e. 0.27), and in [41] (i.e. 0.30). The mean value for the drag coefficient of model #2 is closer to the drag coefficient reported in the original article by Ahmed et al. [1] (i.e. 0.25). In the latter article, the authors mention that the tare drag of the stilts has been compensated for, for the articles of [27], and [41] there is no mention whether the stilt drag is compensated. As for the side force coefficient; both models show a similar pull to the right, but the standard deviation for the #2 model is much larger than that found for any other coefficient. Based on Ahmed body side force coefficients presented in [27], a near-zero mean value was expected. The non-zero values reported here, hint at a constant asymmetrical effect.

As the Ahmed body models of this report had the same general dimensions, the notable difference between the models’ drag coefficients was unexpected. Thus, a follow-up set of experiments was done to clarify what could cause it. Based on those results, it is believed that the difference is partly due to the positioning of the ZZ strips on the nose of the models. For the repeated experiments, the ZZ strips of both models were first removed completely. Without ZZ strips, the drag coefficient of model #2 rose to approximately 0.28, indicating that the ZZ strips were responsible for drag reduction. When the ZZ strips on the nose of model #1 were

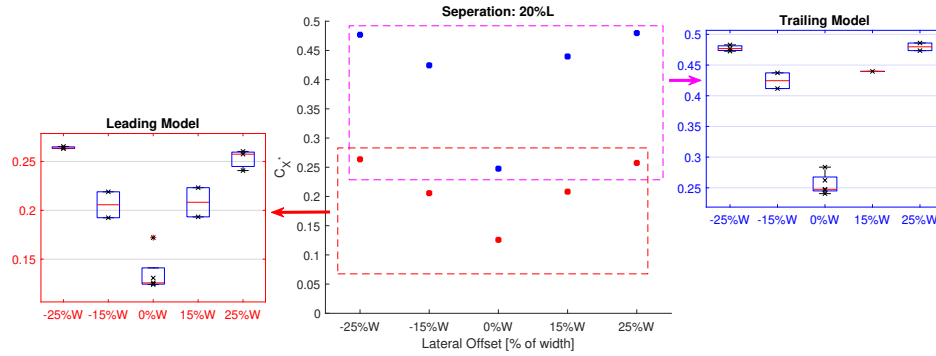


Figure 4.1: Drag coefficients of models and combined drag figure at 20%L longitudinal separation.

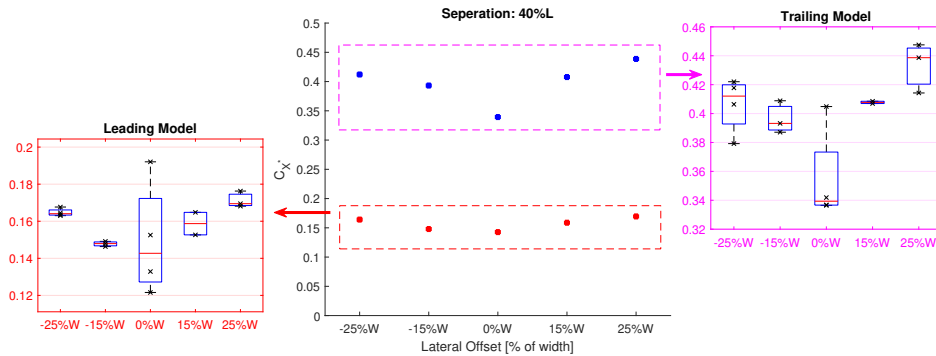


Figure 4.2: Drag coefficients of models and combined drag figure at 40%L longitudinal separation.

removed, the mean drag coefficient remained at 0.28. This was an unexpected result because the models were designed to be the same, and thus the ZZ strips should have had similar effects. However, as mentioned in section 3.1.2, the ZZ strips on model #1 were originally applied about one centimeter further upstream, compared to model #2 (an oversight during the production of the models). A schematic representation of the position of the ZZ strips relative to the corner radius is given in fig. 3.3 in section 3.1.2. Reapplying the ZZ strips to model #1 about one centimeter aft helped reduce the drag coefficient of the model to 0.26, which is closer to the drag coefficient originally measured on model #2. Therefore, it is assumed that one cause of the discrepancy between the two models was likely due to different flow behavior at the nose caused by the positioning of the ZZ strips. Secondly, small geometric differences between the models (resulting from the manual manufacturing method) may account for some of the differences in flow behavior. Regardless of the ZZ strip location, separation at the edges of the nose section was noticed. Woolen tufts on an extension pole were traversed along the edges manually to visually inspect the flow.

#### 4.1.2. Ahmed Body Platoon

For the effect of lateral stagger on the drag of a platoon, see the plots in figs. 4.1 to 4.3. Positive stagger is defined as movement of the trailing vehicle to the right, the leading model's longitudinal and lateral position stays fixed. To display both the considerable differences between leading and trailing model drag coefficients measured while platooning, as well as the smaller variations for each model separately, a combined graph display has been used. For comparison between the two models, the median drag coefficients have been plotted in one of the central graphs. Each graph corresponds to one of the three longitudinal separation distances, with the lateral alignment variations displayed on the x-axis. Smaller graph inserts display the force measurements as box plots of the drag coefficient. The box plots are based on repeated runs of the same experimental setup. The results of the individual runs have been plotted as crosses in the same figure. The red centerline in the box plots indicate the median value of the repeated runs, the boxes indicate the upper and lower quartiles. Whiskers (when shown) indicate the maximum and minimum values in the set of repeated runs.

Let us discuss some observations. First, the leading model consistently experiences a lower drag coefficient than the trailing model under all combinations of separation and stagger. This is surprising because the

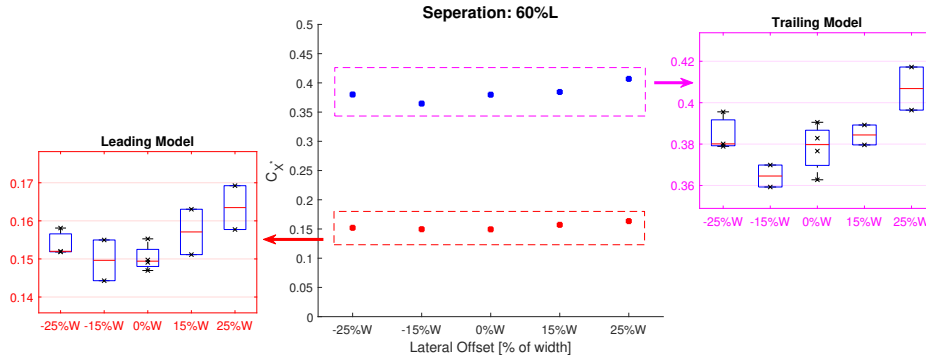


Figure 4.3: Drag coefficients of models and combined drag figure at 60%L longitudinal separation.

trailing model has a lower drag coefficient when in isolation. The drag coefficient of the leading model is in almost all cases lower than its value in isolation. Only at severe lateral offset, and at the shortest separation distance does the lead vehicle's drag coefficient approach that of itself in isolation. The trailing model experiences even more drag than it would in isolation for almost all presented cases. Only when aligned, and at the shortest separation distance does the drag coefficient become similar to its value in isolation.

A second observation from figs. 4.1 to 4.3 is that moving laterally away from the zero-stagger position, increases the drag coefficient of both vehicles in nearly all cases. At 20%L separation, the drag increase appears symmetric, i.e. Either left or right excursions from the aligned case result in similar drag figures. At 40%L separation, the drag increase due to stagger appears less steep, but still largely symmetric. At 60%L separation, there appears to be an asymmetric effect, which is particularly noticeable for the trailing model. The lowest drag is measured at -15%W stagger (i.e. to the left), rather than at zero stagger. Drag measurements at the leading model also appear to be lower when the platoon is staggered to the left, in comparison with lateral stagger to the right. However, considering that the spread of drag coefficients per lateral station is relatively large compared to the difference in mean values between the stations, the asymmetry could also be due to measurement error.

Sep. Dist. / Lat. Offset	-25%W	-15%W	0%W	15%W	25%W
20%L	0.37	0.32	0.20	0.33	0.37
40%L	0.29	0.27	0.25	0.28	0.30
60%L	0.27	0.26	0.26	0.27	0.29

Table 4.2: Mean drag ( $x^*$ ) force coefficients for average platoon (average combined drag coefficient). The average drag coefficient of the models in isolation is 0.27.

To analyze the performance of the platoon as a whole, the average drag coefficient of the two models should be compared to the average drag coefficient of the two models in isolation. For this analysis, the drag coefficient of a model at a certain position is the average of the sampled drag coefficients. As shown in table 4.2, one can conclude that in the case of zero stagger, the lowest average drag for this platoon is obtained when the vehicles are at the shortest separation distance. Thus, increasing the separation distance worsens the savings. However, when lateral stagger is introduced, it is more beneficial to increase the separation distance. In other words; the penalty for misalignment is much higher at close longitudinal separation distances than at large longitudinal separation distances.

A single measurement in the combined plot of fig. 4.2 warrants a closer look. At 40%L separation and no lateral stagger, the maximum drag coefficient of both leading and trailing models is notably higher than the median. This is believed not to be a measurement error. If one looks at the drag force over time, see the filtered graph in fig. 4.4, a pattern is discernible. The drag of both models “jumps” aperiodically. The jumps are synchronous which makes it unlikely that this is a random sensor error. Heavy buffeting of both vehicles was also noticed visually in the wind tunnel. Interestingly, repeated attempts to replicate the phenomenon did not lead to similar results. Therefore, one could assume that the behavior is very sensitive to alignment. On a separate note, notice the drag of the trailing model after wind tunnel shutdown. The load cell measurement does not return to zero immediately but measures a value lower than before. This behavior has been mentioned in section 3.3.2. However, each measurement starts with a new baseline measurement to minimize

the error due to zero-offset.

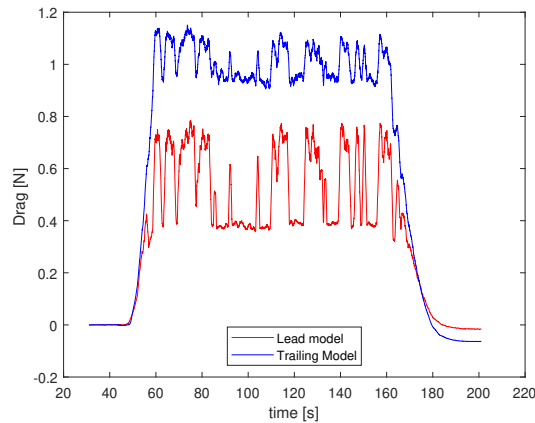


Figure 4.4: Instantaneous drag force for platoon at 40% $L$  separation, 0° yaw, and no stagger. Drag values are obtained from applying a moving mean filter of window size 500 samples to the raw signal of 500Hz. Notice the aperiodic “jumps” in drag magnitude.

Having established that stagger has a measurable effect on the drag coefficient of the platoon, it is worthwhile to examine the side forces on the Ahmed bodies in drafting. Normalized side force coefficients have been plotted in figs. 4.5 to 4.7, and should be compared to the isolated side force coefficients, which are presented in table 4.1.

For the platoon at 60% $L$  separation, the spread in force measurements does not present a clear trend, and neither is it visible at 40% $L$  separation. However, at 20% $L$  separation, despite the spread, there is a clear trend. The side forces increase in magnitude for the  $|15\%|W$  lateral offset cases. Moving even further away laterally does not yield higher side forces. The sign of the side forces indicates that the vehicles are drawn to one another in the lateral direction. That is, if the trailing model staggers to the left, the aerodynamic side force pushes it back to the right, while the leading model is forced to the left. Thus, at the shortest separation distance, the side force is stabilizing in nature for the stagger distances tested here.

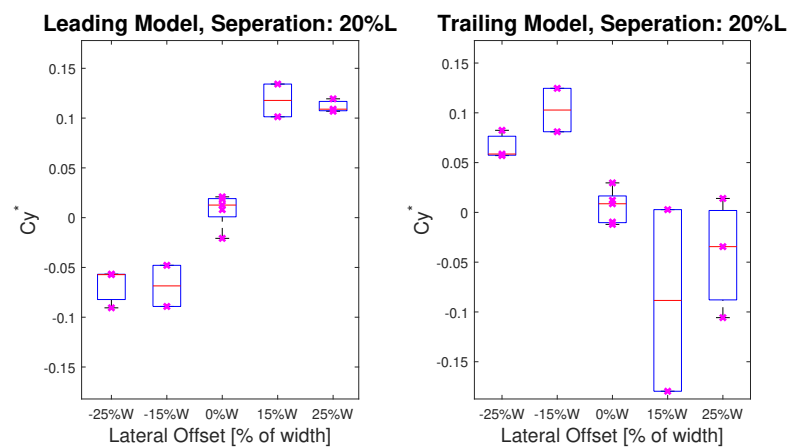


Figure 4.5: Side force coefficients of models and combined drag figure at 20% $L$  longitudinal separation.

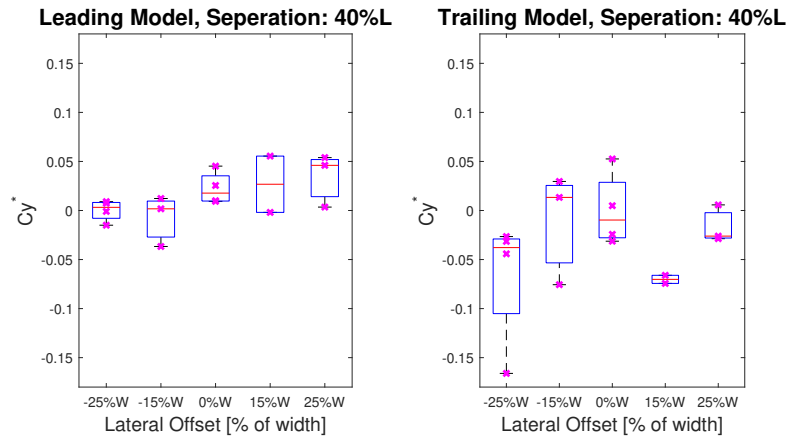


Figure 4.6: Side force coefficients of models and combined drag figure at 40%L longitudinal separation.

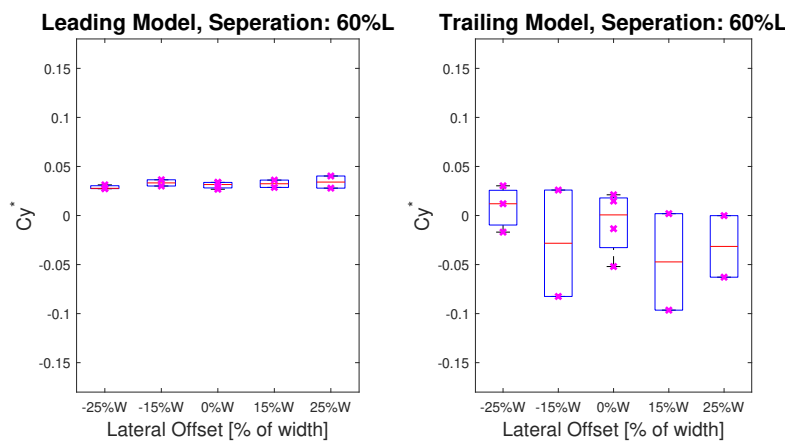


Figure 4.7: Side force coefficients of models and combined drag figure at 60%L longitudinal separation.

## 4.2. Pressure tap measurements

In the following section, results of pressure tap measurements over the rear part model #1 are presented and discussed. The pressure measurements were done one a grid of 16 pressure ports, as described in section 3.1.2.

The contour plots presented throughout this section show the average pressure fields across the rear surface of model #1. Each dot on the figures corresponds to the pressure port located at its center. The contours have been obtained through linear interpolation between the pressure port measurements. All contour plots are based on the average pressure coefficients of single measurement runs (thus not averaged over multiple runs), but have been compared to repeated runs to inspect for deviations. None were found; repeated runs showed similar pressure distributions.

During the experiments, it was found that pressure port #10 (located at  $y^* = -0.15$ ,  $z^* = 0.57$ ) appeared to be malfunctioning. Because it was not possible to establish which measurements of pressure port #10 were entirely trustworthy, data stemming from that port has been excluded from all contour plots. The values that are shown in the plots at the location of pressure port #10 are based on linear interpolation of its nearest neighbors.

### 4.2.1. Isolated Ahmed Body

At zero degree yaw, the average pressure field shows an asymmetric distribution with respect to the vertical plane of symmetry of the model. Lowest pressure occurs at the right-hand side. The average pressure coefficient is  $C_p = -0.20$ , which is similar to the average pressure coefficients found in [41] and [27]. To investigate how much of the asymmetric pressure distribution is due to some unintended sideslip angle, the model was yawed by five degrees left and right. Yawing the model lowered the pressure coefficients at all ports. The

average pressure coefficients were  $C_p = -0.23$  and  $C_p = -0.26$  for  $5^\circ$  and  $-5^\circ$  yaw respectively. The lateral component of the pressure gradient orientates itself according to the yaw angle as is shown in fig. 4.9. The lowest pressure is observed on the leeward side of the model. It is to be expected that low pressure occurs at the leeward side if one would assume the Ahmed body at sideslip to be similar to a symmetric airfoil at an angle of attack. In the case of an airfoil, a pressure differential will exist between the top-and-bottom side. In the case of the Ahmed body, the pressure differential exists between left-and right-hand sides.

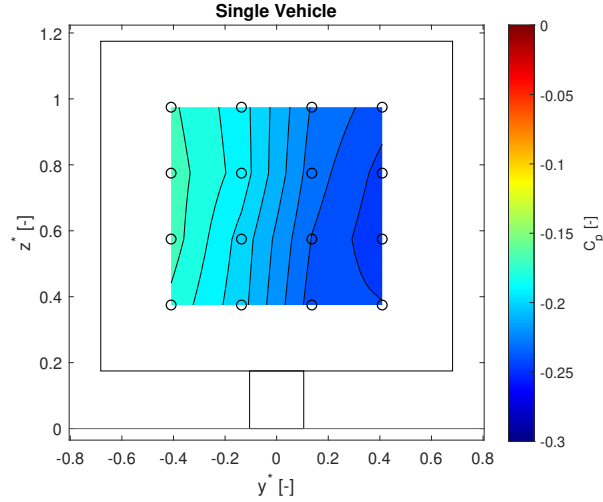


Figure 4.8: Average pressure coefficient distribution on the rear face of model #1, in isolation at  $0^\circ$  yaw.

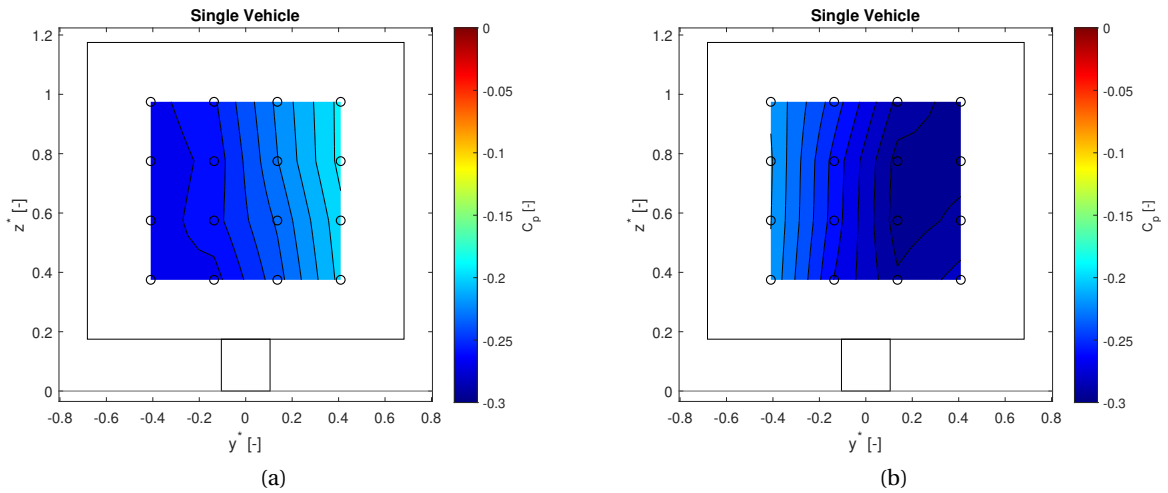


Figure 4.9: Pressure coefficient distribution on the rear face of model #1, in isolation at (a)  $5^\circ$  yaw, and (b)  $-5^\circ$  yaw.

In the introductory chapter chapter 2, it was mentioned that the squareback Ahmed body shows bi-stable behavior at zero degrees sideslip, and Reynolds numbers similar to those tested here. To examine the wake stability for the experiments performed during this thesis, probability histograms have been created which indicate the likeliness and strength of a horizontal pressure gradient component across the rear face of the model. If the wake was indeed bi-stable, then one should expect a non-zero horizontal component of the gradient at nearly all times (except for the brief moment where the wake moves from one state to the next). Over a longer time, both states (which are mirror images and thus should show a lateral gradient component equal in magnitude and opposite in sign) should have occurred for roughly the same duration. Therefore two peaks in the probability density function should be expected [27]. The lateral component of the pressure gradient is approximated across the third horizontal row from the bottom, in the central position ( $z^* = 77[z/H]$ ,  $y^* = 0[y/H]$ ). This row is centrally located, which is similar to the location of the gradient examined in [27] and has not shown malfunctioning ports (unlike the row which contains pressure port number 10).

To create the probability histogram, a finite difference approximation has been made based on ports #6 and #7 for each pressure measurement in an experiment (samples were taken at 2000 Hertz), see also sections 3.2.2 and 3.3.3. For comparison, other port combinations have also been used to confirm the consistency of the findings. All combinations revealed similar histograms. The signal has been smoothed by averaging the pressure over subsequent intervals of 20 samples. The filtered signal is thus effectively at 100Hz. Because the pressure scanner is located at some distance from the pressure ports, the air mass in the tubing which connected the pressure ports to the pressure scanner will have also filtered some pressure fluctuations. However, the states of a bi-stable wake exist for such large time intervals (in the order of several seconds) that they will be measured if present [27]. The histograms consist of bins that are sized  $0.01 [\partial p / \partial y^*]$ , the function value in the graphs indicates the likeliness of measuring a pressure gradient in that bin.

Probability density functions for the isolated vehicle at three yaw angles are shown in fig. 4.10. What stands out from the results, is that the projected gradient shows a single peak for all cases. The histogram at zero yaw is very similar in shape and magnitude to that at minus five degrees yaw. As could be expected from fig. 4.8, the most likely gradient at zero degrees yaw is not zero, but slightly negative (corresponding with the bin  $-0.1$  to  $-0.08 [\partial p / \partial y^*]$ ). The wake pressure gradient at minus five degrees yaw resembles a mirror image of the other two histograms. The bin having the highest probability is of the same magnitude, but different sign.

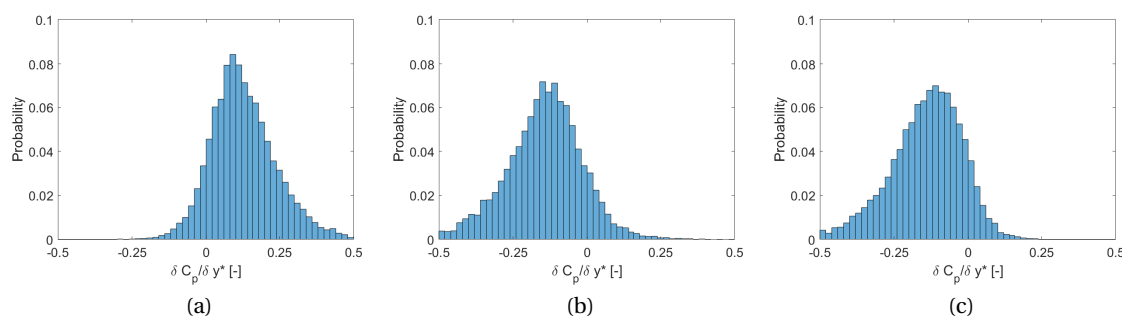


Figure 4.10: Probability Density Function of the pressure coefficient differential, in isolation at (a)  $5^\circ$  yaw, (b)  $0^\circ$  yaw, and (c) at  $-5^\circ$  yaw.

#### 4.2.2. Ahmed Bodies Platoon

Average pressure contours for the platoon at zero yaw and various stagger, are shown in figs. 4.11 to 4.13. The combined average pressure coefficients of all (functioning) pressure ports for a given setup has been summarized in table 4.3. From these results, one can observe that, compared to the isolated case, the platoon leader benefits from higher pressures over the rear surface in the majority of cases. Depending on the separation distance, however, the pressure distribution changes quite differently with lateral offsets. At a separation of  $60\%L$ , lateral stagger does not appear to change the pressure distribution much. A top-bottom gradient, not seen in the isolated cases, seems to exist regardless of the lateral position. The upper half measures higher pressure than the bottom half.

At  $40\%L$  longitudinal separation a left-right oriented gradient appears in response to misalignment, see fig. 4.12. The lowest pressure occurs on the side to which the trailing model moves (i.e. with negative lateral offset, the trailing model moves to the left, and so the area of lowest pressure at the leading model's rear surface moves to the left). This might be seen as counter-intuitive, as one would expect that the stagnation pressure in front of the trailing vehicle's nose would shift the region of highest pressure to the side of the lateral excursion. Furthermore, with larger stagger distances, a more noticeable vertical component in the pressure gradient appears as well. Similar to the  $60\%L$  separation case, the upper half seems to be at a higher pressure than the lower half.

At the  $20\%L$  separation distance, the differences between aligned, and non-aligned platoons are very pronounced. The magnitude and spread of the pressure coefficients necessitates a wider color bar in fig. 4.11, than in figs. 4.12 and 4.13. Thus, one should keep in mind that the colors shown in these figures do not necessarily represent the same pressure coefficients. When aligned, the pressure plot shows a unique symmetry in the vertical plane, with higher pressures in a vertical column at  $y^* = 0$  flanked by areas of lower pressure. Little top to bottom difference is visible. Lateral misalignment introduces areas of low pressure at the top and bottom edge, and a left-right gradient component which varies with height. As seen before, the lowest pressure moves laterally with the direction of misalignment. The contour plots for the staggered combinations

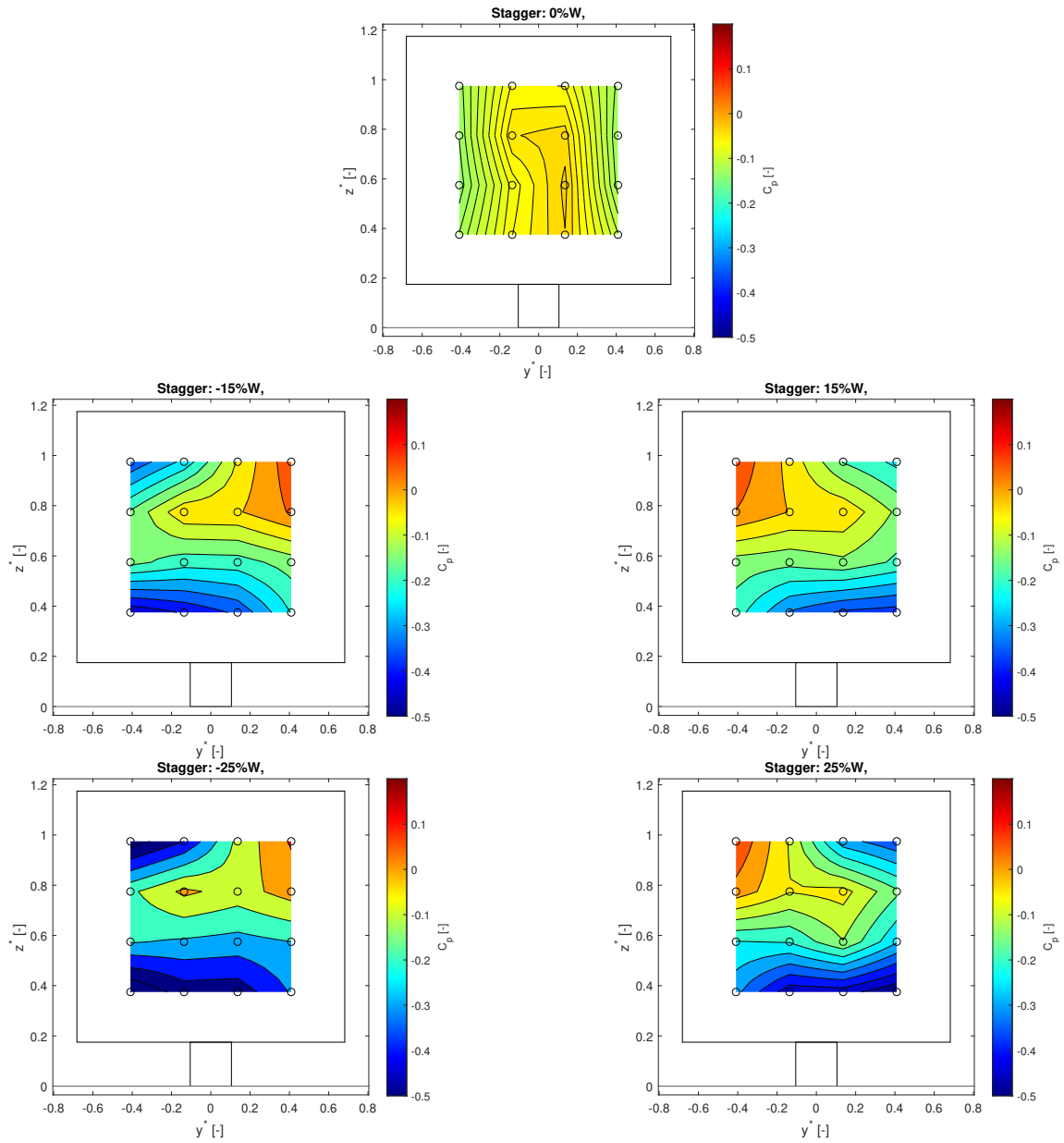


Figure 4.11: Pressure coefficient map across rear face of model #1, at various stagger positions. Longitudinal separation is  $20\%L$  and yaw is  $0^\circ$ .

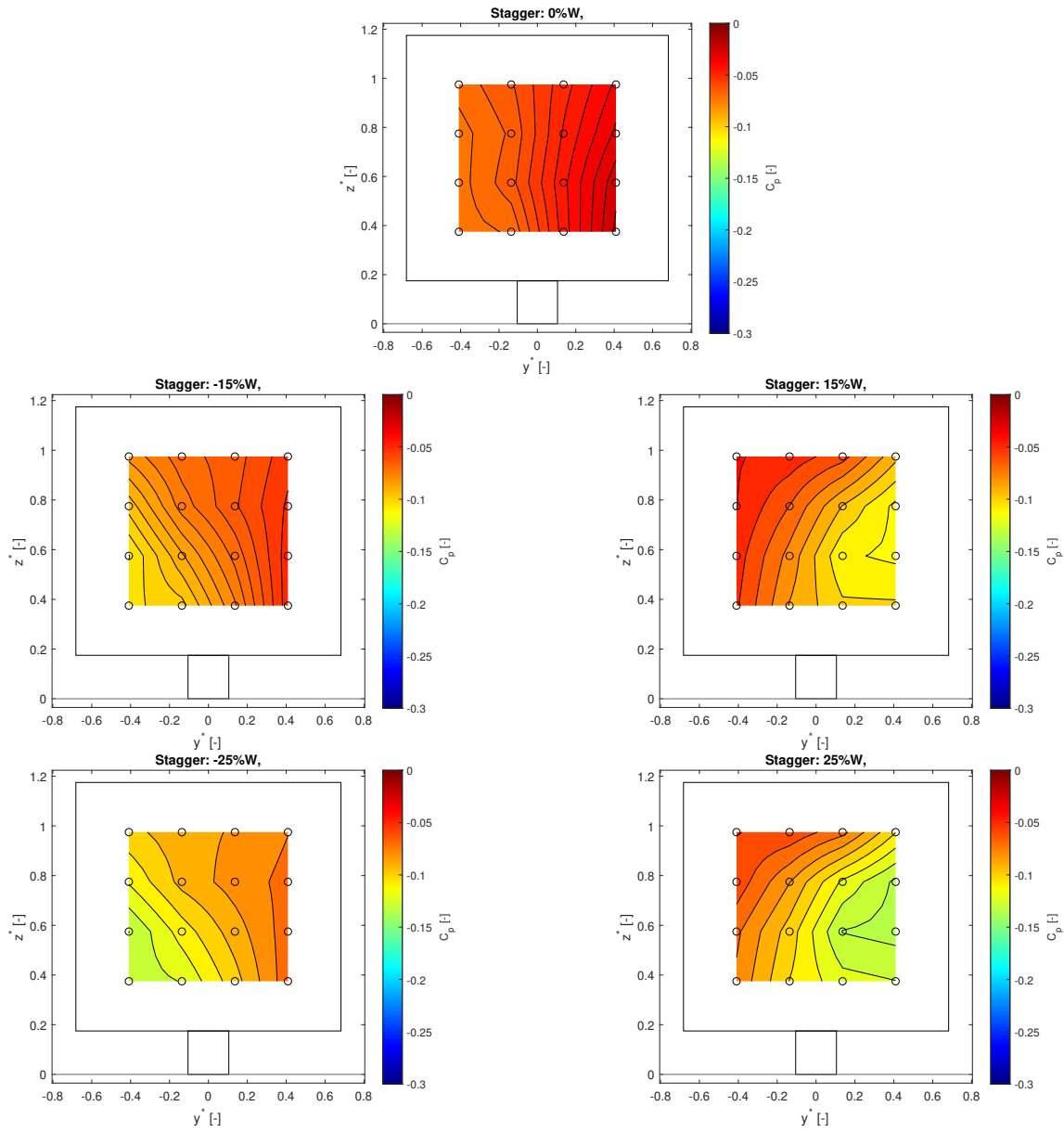


Figure 4.12: Pressure coefficient map across rear face of model #1, at various stagger positions. Longitudinal separation is  $40\%L$  and yaw is  $0^\circ$ .

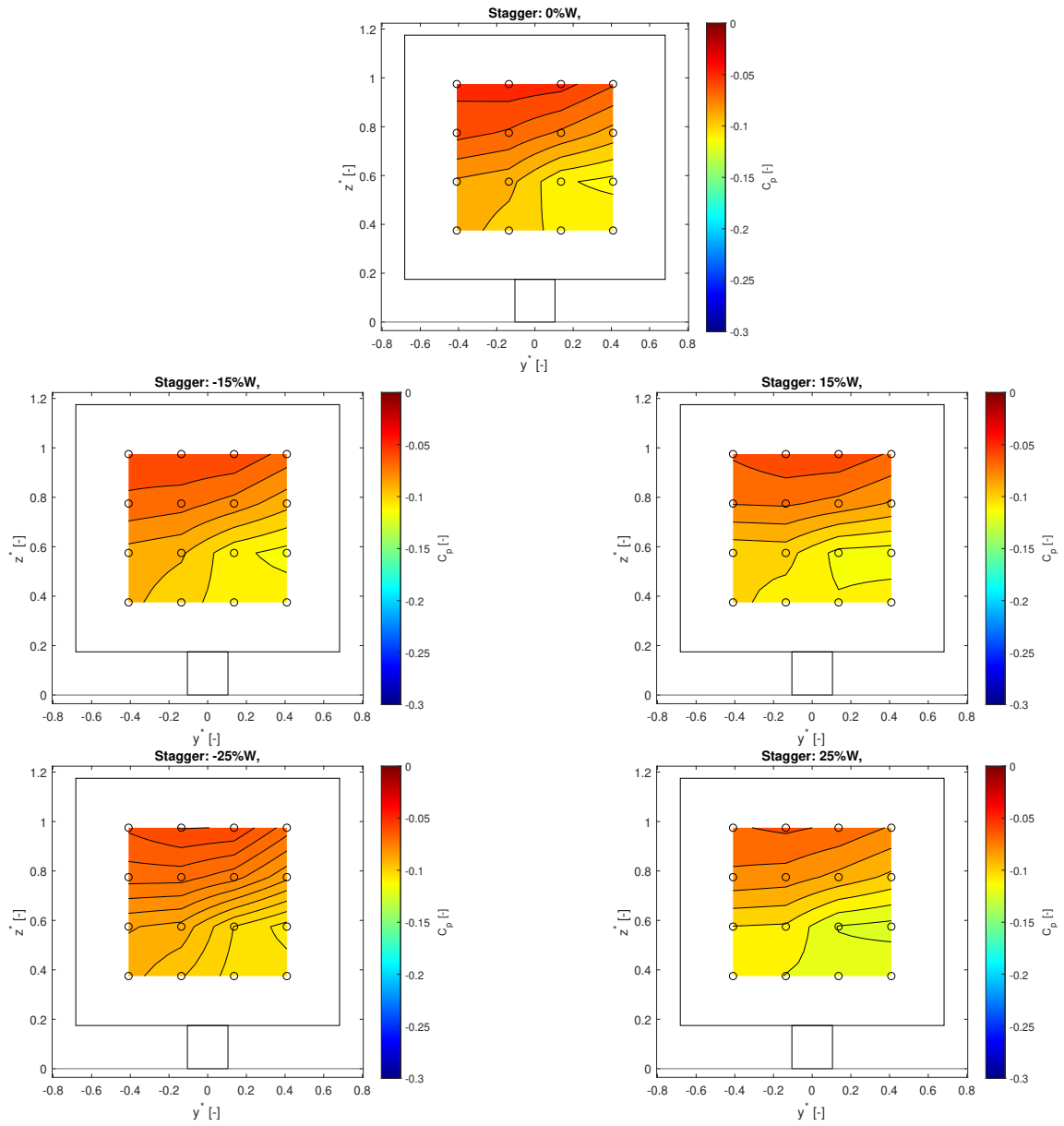


Figure 4.13: Pressure coefficient map across rear face of model #1, at stagger positions. Separation is 60% and yaw is  $0^\circ$ .

suggest that the areas of lowest pressure lie beyond the grid of pressure ports.

One can observe from table 4.3 that the combined average pressure decreases with increased lateral offset for the longitudinal separation distances of  $20\%L$  and  $40\%L$ , but stays equal for the case of  $60\%L$ . This is consistent with the drag measurements, as a lower average pressure results in more pressure drag, and at the furthest longitudinal separation, there is little influence of lateral offset. However, the difference between the average pressure coefficients with respect to the longitudinal separation distance does not agree well with the drag measurements. The relatively high average pressure coefficient at  $40\%L$  and  $0\%W$  ( $C_p = -0.05$ ) would suggest a significantly lower drag coefficient for the leading model, when compared to other drafting setups. The drag measurements have shown that it is not necessarily the case. It should be noted that the pressure measurements cover only a part of the rear surface and might therefore not be fully representative of the actual average pressure across the entire rear face of the model. Furthermore, the pressure measurements represent a single measurement run, while the drag measurements are averaged over multiple runs. Although the pressure measurements are consistent within their sample group, the force measurements have shown quite a significant spread in drag coefficient at  $40\%L$  and  $0\%W$  separation and stagger (see again fig. 4.2).

The observation that the aligned platoon at  $20\%L$  longitudinal separation creates a symmetric pressure distribution leads to the question of whether this is due to the before mentioned bi-stability. However, the probability density function of the pressure gradient, shown in fig. 4.14 (a), shows a single peak. Therefore, no bi-stable behavior is measured. The peak is centered closely around  $\partial C_p / \partial y^* = 0$ , which is expected because of the symmetry of the average field. Interestingly, the peak is also very “flat”, which signals that the lateral component of the pressure gradient must fluctuate around the average value more strongly than for the isolated case. At  $40\%L$  separation, the probability histogram presented in fig. 4.14 (b), shows a single peak at a non-zero lateral component of the pressure gradient (0.04 to 0.06 [ $\partial C_p / \partial y^*$ ]). The peak is “taller” than observed in fig. 4.14 (a). The histogram for  $60\%L$  separation, fig. 4.14 (c), similarly shows one peak ( $-0.06$  to  $-0.04$  [ $\partial C_p / \partial y^*$ ]). The latter two distributions do not show the one-sided “tail” of the histograms of the isolated models. Therefore, the fluctuations must be more symmetrically distributed for the cases of  $40\%L$  and  $60\%L$  longitudinal separation.

Longitudinal Separation	Lateral Offset				
	-25%W	-15%W	0%W	15%W	25%W
60%L	-0.08	-0.08	-0.08	-0.08	-0.08
40%L	-0.09	-0.07	-0.05	-0.07	-0.09
20%L	-0.23	-0.16	-0.09	-0.13	-0.20

Table 4.3: Average pressure coefficient ( $C_p$ ) across rear face of leading model for tested combinations of longitudinal separation and lateral offset. Sideslip angle is  $0^\circ$ , pressure averages are from single runs.

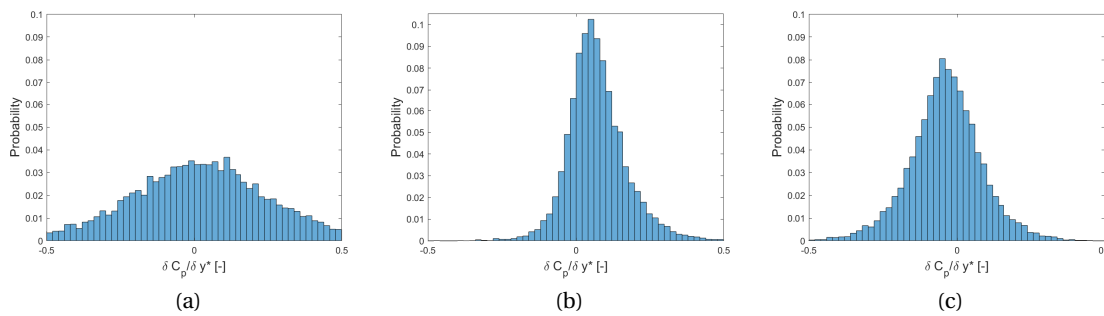


Figure 4.14: Probability density functions of pressure coefficient gradient  $\partial C_p / \partial y$  at  $y^* = 0$  for leading vehicle in platoon. No stagger,  $0^\circ$  yaw, at: (a)  $20\%L$  separation, (b)  $40\%L$  separation, (c)  $60\%L$  separation.

### 4.3. Coaxial Volumetric Velocimetry measurements

With the use of the Coaxial Volumetric Velocimetry (CVV) system described in section 3.2.3, three-dimensional average flow fields of the space between the two Ahmed body models have been created. Now, based on the results of the load cells and the pressure ports, the relation between mean flow phenomena and force/pressure can be examined. The aim is to create a satisfying description of the flow that correlates with the earlier results.

#### 4.3.1. Isolated Ahmed body

Let us start by examining the flow field for an isolated vehicle. In fig. 4.15 the horizontal and vertical cross-sections are shown of the average normalized velocity  $u/u_\infty$ . Two-dimensional streamlines are superimposed. Dimensions are given in a reference frame of which the dimensions are relative to the model height ( $x^* = x/H$ ,  $y^* = y/H$ , and  $z^* = z/H$ ).

In both the horizontal and vertical view, a recirculating wake is visible. Seen from the top, the wake appears skewed to the left. That is, streamlines separating at the right side, curve to the left of center. This is in agreement with the pressure gradient of fig. 4.8. Remembering that the pressure far outboard (in the lateral direction) on both sides of the model is at  $p_\infty$ , then it is understandable that the side of the lowest pressure in the near-wake will turn the separating streamline the furthest inwards. The side view shows recirculating structures which are at similar distances from the base. Downstream of the near-wake, the streamlines curve downwards due to the proximity of the floor. At the floorboard level, between  $x^* = 1.5$  and  $x^* = 2.0$ , there appears to be a region of very low flow velocity. As was shown by Grandemange [26], the pressure along the floor (for a non-rolling floor) will increase quite rapidly just after the recirculation bubble of an isolated wake. This adverse pressure gradient could have caused the boundary layer at the floorboard to separate.

The top view appears similar to the conditionally averaged flow fields shown in [26] (reproduced in fig. 2.25), but not to the global averages shown in the same paper or those of [41] for example. The flow fields presented in this report however are globally averaged, no conditional averaging has been performed. The similarity between the presented flow fields and the conditionally averaged examples from literature is due to the off-center location of what appears to be the single saddle-point (at  $1.5X/H$ , and  $-0.3Y/H$ ), and the shape and locations of the vortical structures. Based on these observations, it is reasonable to assume that the wake of the isolated model presented in this thesis is a continuously present occurrence of only one of the bi-stable states. Why exactly only one state would manifest itself is unclear. This matter will be further elaborated upon in the discussion section of this chapter.

In section 2.2, the recirculation region topology behind a three-dimensional bluff body was described as toric. However, in [29] the author states that for the asymmetric state of the wake the recirculation region will not have a toric organization. Indeed, subsequent articles have suggested asymmetric vortex distributions. In [57] the existence of two unconnected vortices that extend downstream is proposed, while in [56] it is suggested that there is a single horseshoe vortex which, as it travels downstream, rolls up into a single vortex line. In fig. 4.16, two velocity contours are shown from a rear view ( $y^*z^*$  plane). The most upstream location ( $x^* = 0.6$ ) shows two vortex centers, while the downstream location ( $x^* = 1.68$ ) shows only one at the opposite lateral end. The benefit of CVV measurements is that it allows for direct three-dimensional analysis of the flow field, rather than the composition of planar fields, as was done for the mentioned articles. Additionally, processing software TecPlot 360 provides an automated means of retrieving the centers swirling flows [70], which can serve as identifiers of vortex cores. The result is a (collection of) line elements at the extracted vortex cores in the recirculating region and beyond, as shown in fig. 4.17. Although there are gaps between the line section, the vortex cores suggest a largely toroidal and yawed torus in the recirculation region. Additionally there is a straight section of swirling flow that extends downstream. The observed flow topology matches the description of [56].

#### 4.3.2. Aligned Platoon

Next, let us consider the platoon at  $60\%L$  separation, at zero stagger, and zero yaw. Average flow velocities and streamlines are presented in fig. 4.18. For a top view of the wake, see fig. 4.18 (a). From the latter, it is clear that the recirculating wake region extends to the front of the trailing model. The recirculation region is thereby lengthened compared to the isolated case. This observation would align with the general notion that longer recirculation regions are related to increased base pressure [29, 59]. As shown in [12], an increased downstream pressure (e.g. due to stagnation at trailing model) increases pressure in the recirculation bubble. When the recirculation bubble is at higher pressure, then the separating streamline is curved inwards less,

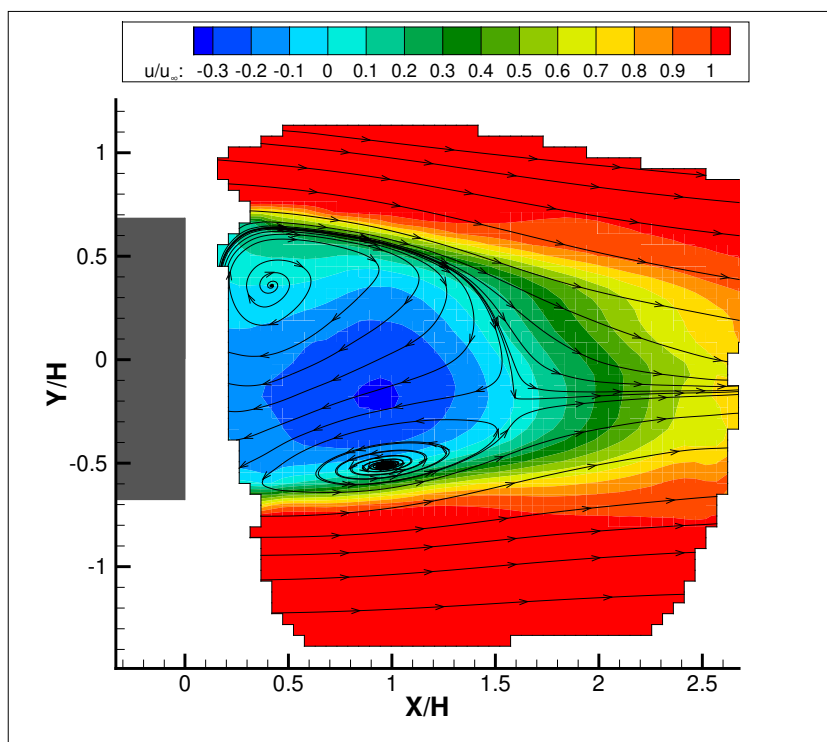
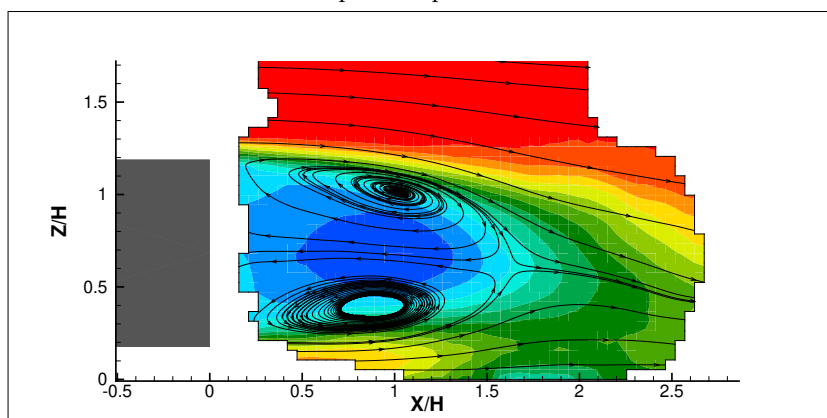
(a) Top view at plane  $z^* = 0.7$ (b) Side view at plane  $y^* = 0$ 

Figure 4.15: Contours of normalized average flow velocity in x-direction, and streamline patterns. Single vehicle (model #1) at  $0^\circ$  yaw. Bin size:  $30 \times 30 \times 30$   $[mm^3]$ .

and thus the entire region is lengthened.

The side view of fig. 4.18 (b) shows four vortical structures. The lower structure closest to the leading vehicle ( $X/H=0.5$ , and  $Z/H=0.5$ ) appears larger than in the isolated wake. The two vortex centers in the upper structure ( $X/H=1.2$ , and  $Z/H=1.1$ ) seem to be a part of the same circulating flow. This would suggest a long recirculation zone at the top, which spans almost the entire region between the two models. Some swirling flow also appears low in the domain, halfway between the two models ( $X/H=1.5$ , and  $Z/H=0.2$ ). The small recirculation zone is located between the upward turning streamlines that emerge from under the leading model and the streamlines that appear from the nose of the trailing vehicle. As was mentioned for the isolated model; the pressure in the wake can rise quickly at the floor. Consequentially, the boundary layer on the floor might separate. The reverse flow and the swirl suggest that this has indeed occurred for the presented platoon setup. A possible explanation for the increased upwards curvature of the streamlines that emerge from under the leading model, and the separation at the floor, could be the blockage that is presented by the trailing

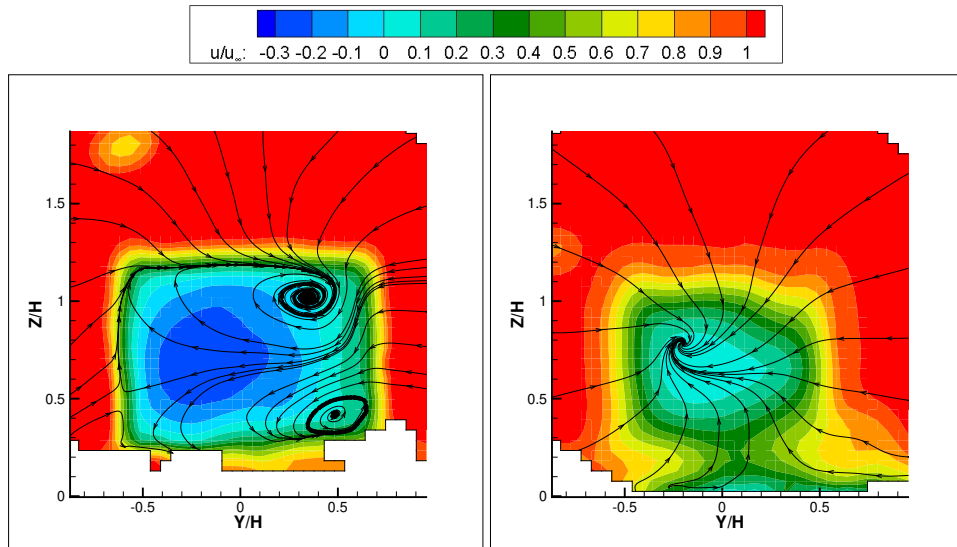


Figure 4.16: Figure 4.16: Contours of average flow velocity in x-direction, and streamline patterns. Isolated model at  $0^\circ$  yaw. Location of vertical plane:  $x^* = 0.6$  (left),  $x^* = 1.68$  (right). Bin size:  $30 \times 30 \times 30$  [mm<sup>3</sup>]

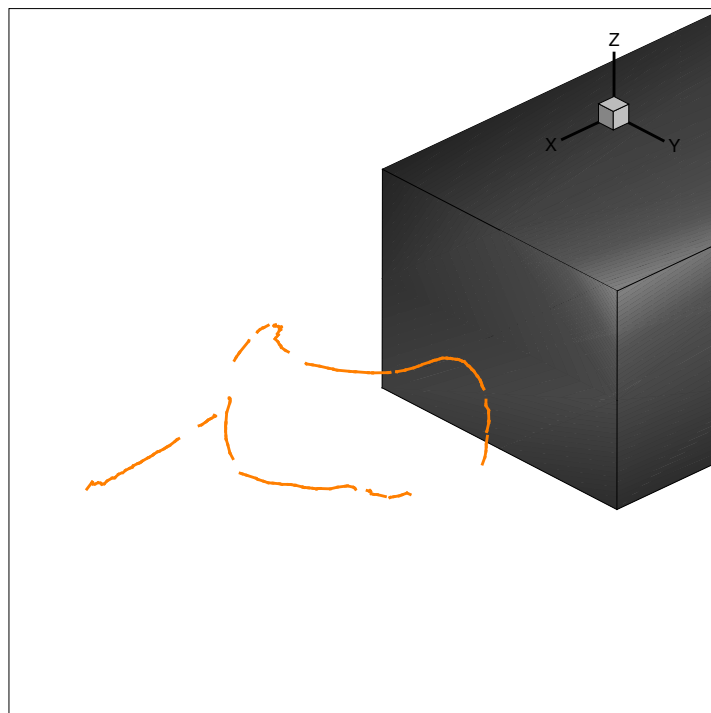


Figure 4.17: Three-dimensional vortex-core topology, identified using the "vortex core extraction method" in TecPlot 360 [70].

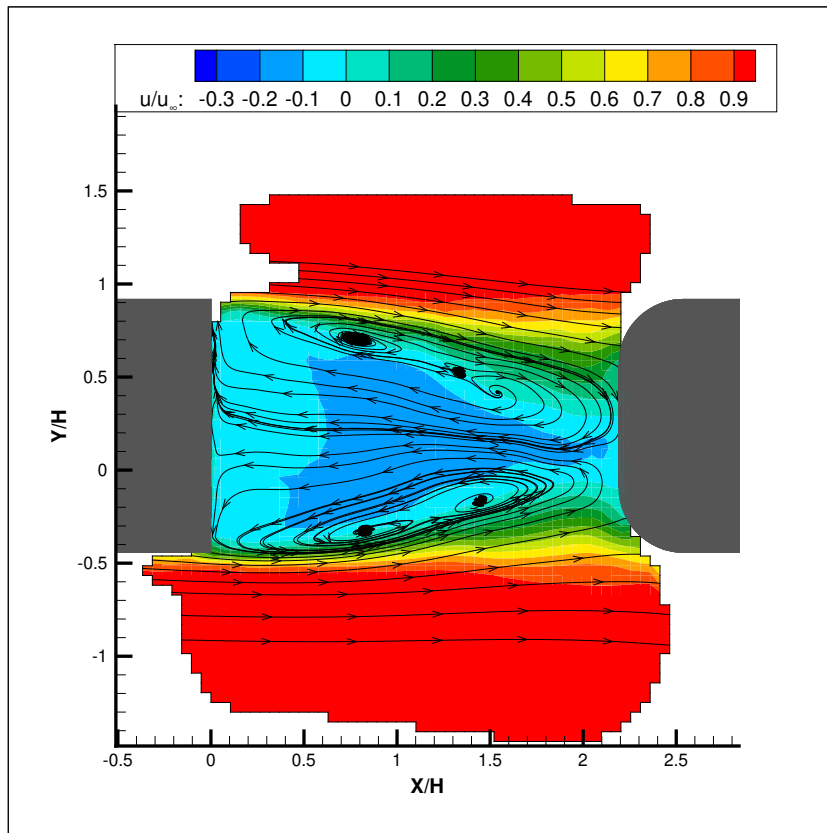
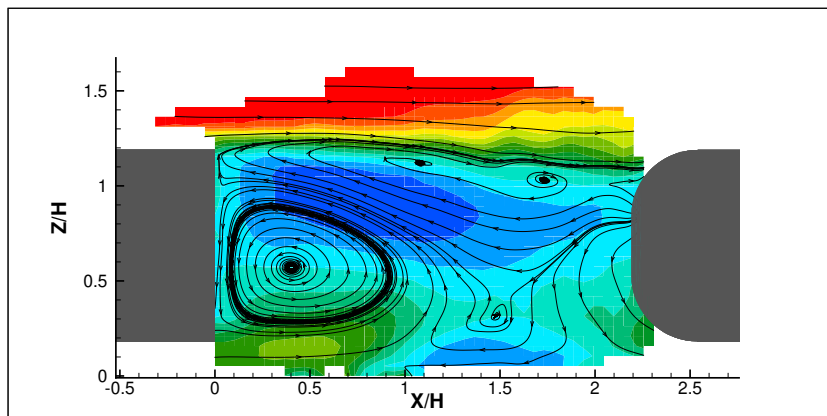
(a) Top view at plane  $z^* = 0.7$ (b) Side view at plane  $y^* = 0$ 

Figure 4.18: Contours of average flow velocity in x-direction, and streamline patterns. Platoon at 60% $L$  longitudinal separation, 0% $W$  lateral stagger, and 0°yaw. Bin size: 30x30x30 [mm<sup>3</sup>].

model. One should also keep in mind that the momentum of the flow that emerges from under the leading vehicle is likely reduced due to the wake of the centrally mounted support pole. The pressure distributions of fig. 4.13 have shown that at a separation distance of  $60\%L$ , regardless of stagger, the lower half of the leading Ahmed body model experiences a lowered pressure compared to the upper half. Such a pressure decrease corresponds with the presence of the recirculating structure close to the lower base of the model, while the upper recirculating structure is located somewhat further downstream.

In fig. 4.19 the average flow velocity between the models is shown for  $20\%L$  longitudinal separation, zero yaw, and no stagger. Compared to the  $60\%L$  longitudinal separation case, the shear layers do not “turn” into the gap much. The shear layers stagnate far outboard on the nose of the trailing model. From the top view, two vortical structures are visible in the gap between the models. They do not appear symmetrical though. Based on the pressure distribution at the rear of the leading model under equal conditions, shown in fig. 4.11, it would be expected that the left vortex center would be positioned more inboard and that the flow field would be symmetric. The side view, fig. 4.19 (b), shows two recirculation zones as well, suggesting the existence of a toroidal vortex in the gap. Interestingly, the top vortex appears to be shifted towards the trailing model, while the lower vortex is closer to the leader. Something similar has been seen at  $60\%L$  longitudinal separation. There too did the lower vortex core lie closer to the leader than the upper vortex core, when viewed from the side.

### 4.3.3. Platoon at $25\%W$ Lateral Offset

Next, let us investigate the flow field for misaligned platoons, starting with the platoon at  $60\%L$  separation. As seen from the top in fig. 4.20, streamlines in front of the trailing model’s nose show a left-to-right cross-flow along the front surface. The recirculation region has become shorter but retains the symmetric positions of the vortical structures. Instead of stagnating on the nose of the trailing model, the streamlines that divide the near-wake from the freestream stagnate in a saddle point ( $X/H = 1.6$ , and  $Y/H = 0.3$ ). The position of the free stagnation point is similar to that of the isolated case, but mirrored across the vertical plane of symmetry of model #1, e.i. to the right rather than to the left. However, the centers of the vortical structures visible from the top are not similar to the isolated case. Here, the centers of recirculating flow appear at equal distance from the base of model #1. The view from the side shows a slice of the average velocity at  $y^* = -0.43$  as seen from the leading model’s reference system. This plane coincides with the vertical plane of symmetry at the trailing model. The flow appears similar to that of the aligned case, with a long recirculation area in the top part, and a shorter one lower and closer to the leader. However, the small recirculation region at the floorboard level is not visible. When comparing the two views, one must take into account that the plane presented in fig. 4.20 (b) does not coincide with the leading model’s mounting pole wake, while fig. 4.18 (b) does.

As shown in the results fig. 4.13, little seems to change across the rear face of the leading model in terms of average pressure. Changes in the drag coefficient also appear to be minimal, although there seems to be a minor asymmetrical effect, with stagger to the right resulting in slightly higher drag than stagger to the left. Unfortunately, no CVV measurements of positive stagger at  $60\%L$  separation have been made. Based on the figures presented in this section, it appears that lateral stagger mostly changes the flow between the two models by introducing a noticeable cross-flow component across the nose of the trailing model, and by shifting the stagnation point of the recirculating wake upstream (making it a free stagnation point). The recirculation region retains its basic topology.

Looking at fig. 4.21, which depicts the average flow field at  $20\%L$  longitudinal separation and  $-25\%W$  lateral stagger, the near wake is distinctly different from the aligned case. From the top view, one can observe that on the left side, the shear layer is deflected into the gap, while on the other side it passes the nose of the trailing model. The result is a clear cross-flow from left to right in the inter-vehicle gap. Of the two vortices that were visible in the top view of fig. 4.19, only one remains for the misaligned case. It is positioned at the side of the lateral excursion. The side view still shows two vortex cores, but now both are close to the leading model. In the discussion of the pressure contours of fig. 4.11, it was noted that the areas of lowest pressure are possibly linked in a semi-circular pattern. This pattern would coincide with an asymmetric vortical structure in the gap. In figs. 4.22 and 4.23, streamlines have been rendered in three-dimensional space as ribbons for both the aligned and misaligned setups. In the aligned case, the streamlines appear to form a toroidal vortex. In the misaligned case, the streamlines do not form a toroidal vortex but appear to extend downstream along the right-hand side of the trailing model. The location of the vortex “bend” in the gap coincides with the measurement of low pressure in fig. 4.11. Based on figs. 4.21 and 4.23, it can be concluded that lateral misalignment changes the general topology of the flow field in between the two models. The typical toroidal vortex has changed into a horseshoe vortex that extends downstream on one side of the trailing model.

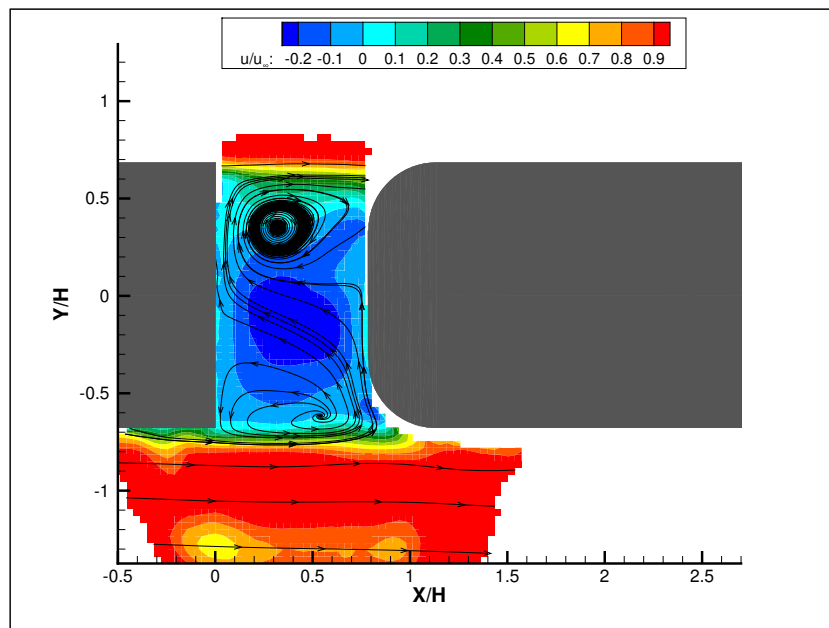
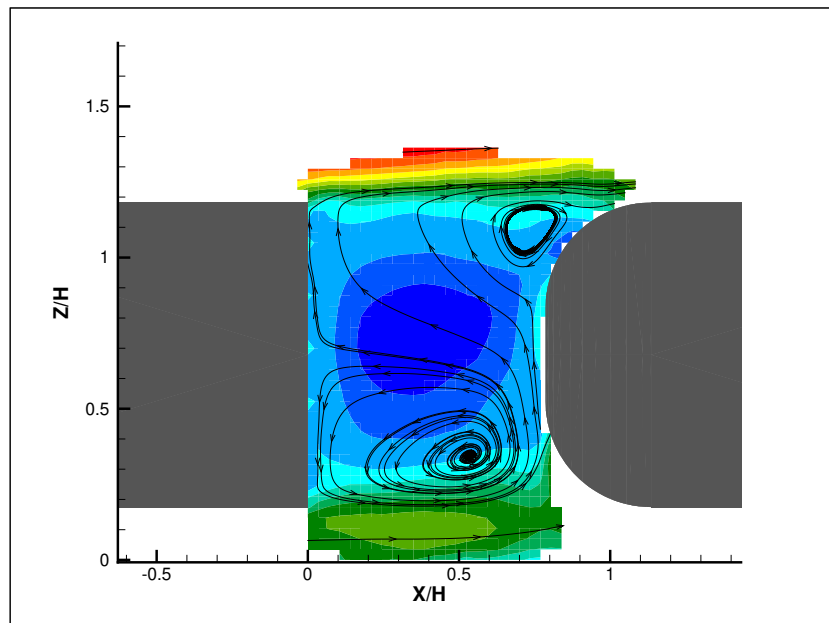
(a) Top view at plane  $z^* = 0.7$ (b) Side view at plane  $y^* = 0$ 

Figure 4.19: Contours of average flow velocity in x-direction, and streamline patterns. Platoon at 20% $L$  longitudinal separation, 0% $W$  lateral stagger, and 0°yaw. Binsize 20x20x20 [mm<sup>3</sup>].

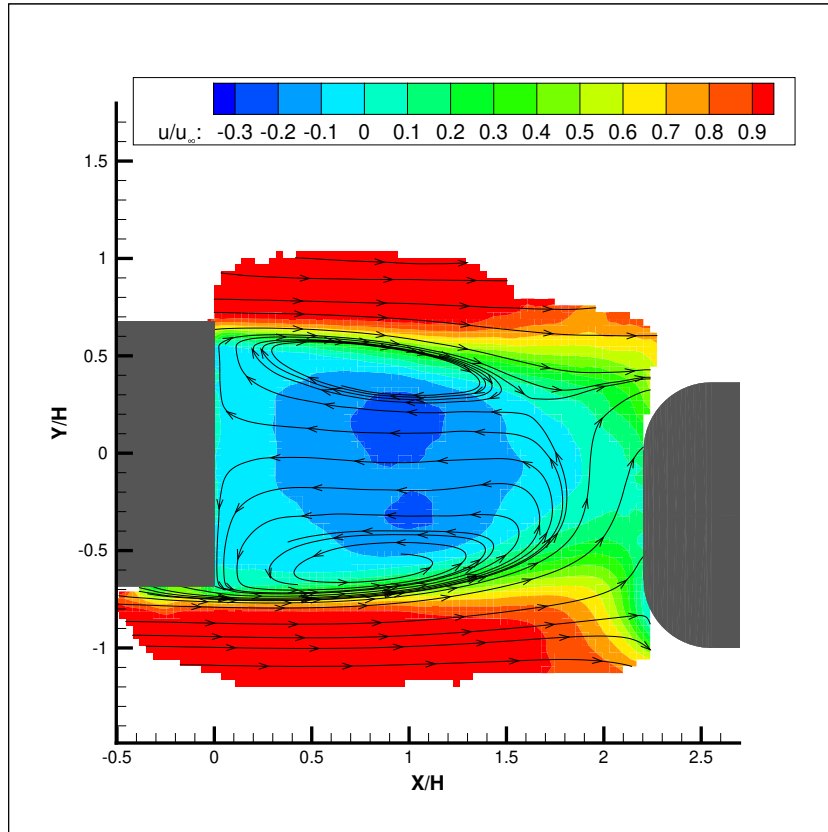
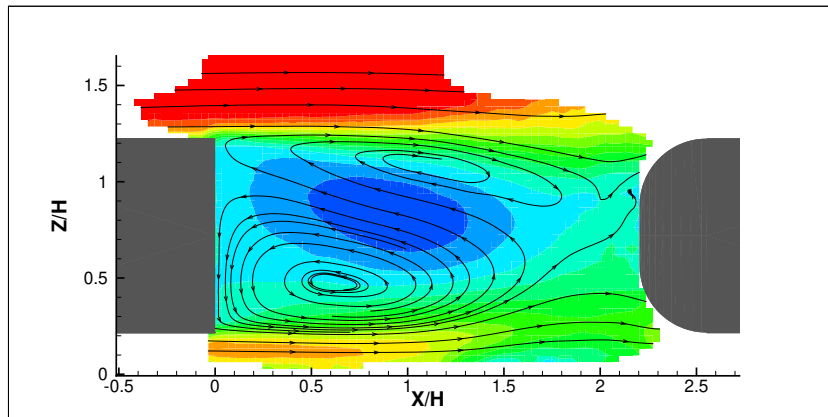
(a) Top view at plane  $z^* = 0.7$ (b) Side view at plane  $y^* = -0.34$ 

Figure 4.20: Contours of average flow velocity in x-direction, and streamline patterns. Platoon at  $60\%L$  longitudinal separation,  $-25\%W$  lateral stagger, and  $0^\circ$  yaw. Binsize  $20 \times 20 \times 20$  [mm<sup>3</sup>].

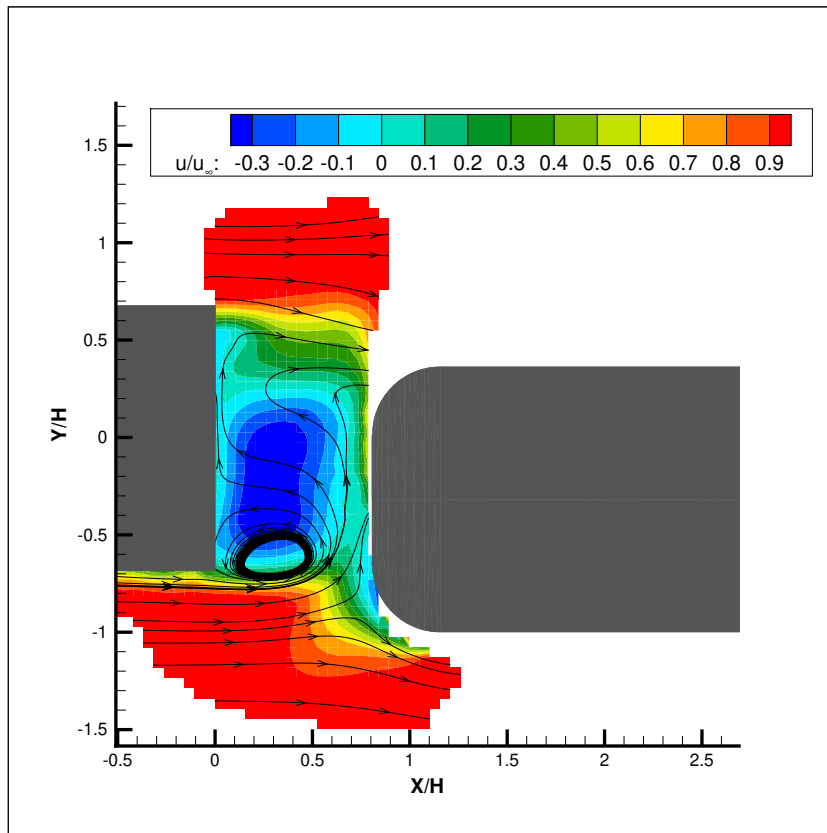
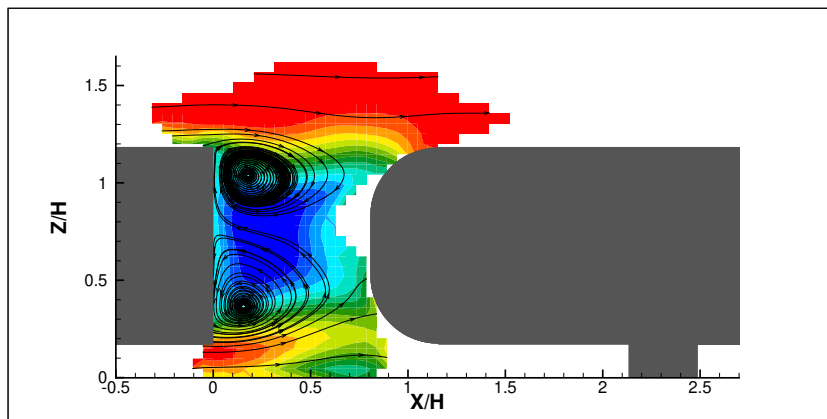
(a) Top view at plane  $z^* = 0.7$ (b) Side view at plane  $y^* = -0.43$ 

Figure 4.21: Contours of average flow velocity in x-direction, and streamline patterns. Platoon at  $20\%L$  longitudinal separation,  $-25\%W$  lateral stagger, and  $0^\circ$  yaw. Binsize  $20 \times 20 \times 20$  [mm<sup>3</sup>].

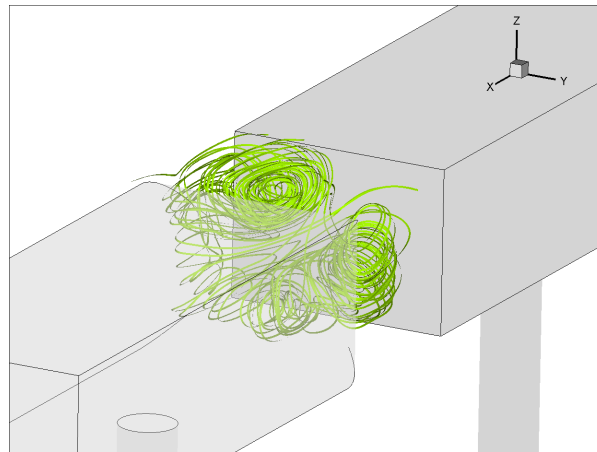


Figure 4.22: Streamlines in gap between models at 20% $L$  longitudinal separation, 0% $W$  lateral stagger, at 0°yaw. Streamline colors are used to increase contrast, and do not represent flow velocity.

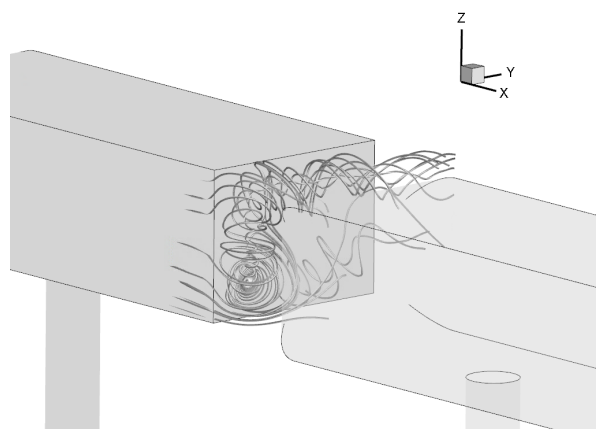


Figure 4.23: Streamlines in gap between models at 20% $L$  longitudinal separation, -25% $W$  lateral stagger, at 0°yaw. Streamline colors are used to increase contrast, and do not represent flow velocity.

## 4.4. Discussion

With the flow measurement results presented and analyzed, it is worthwhile to combine the findings and link them to results from literature. The aim of the discussion is thus to obtain a more general understanding of the observed flow phenomena and try to explain the most surprising observations.

### 4.4.1. On the trailing model drag savings

Based on the presented experiments, the trailing vehicle in the Ahmed body platoon does not benefit from drafting at all. However, it has been shown in literature that for other road vehicles, or models thereof, drafting does lower aerodynamic drag. What could cause the difference? Perhaps it is best to compare the latest results with two previous studies that reported drag increases due to drafting. These are the reports of van Tilborg [72] and Gheysens [24]; both experiments were also done at the TU Delft. The influence of suction on the edges of the nose was key in understanding the drag coefficient of the trailing vehicles. Pressure measurements confirmed that by placing the trailing vehicles in the wake of the leader, the suction force was lost. When streamlines from the freestream curve towards the rounded edges of the trailing model as they pass the near-wake of the leader, forcing them outboard again increases the pressure locally according to [24]. Although stagnation pressure across the flat part of the nose section was indeed decreased due to the low-momentum wake; that did not balance out the loss of propulsive force. Which of these two effects was dominant (momentum deficit versus suction loss) depended much on the relative importance of the flat frontal surface and the edges on the drag coefficient. There is however another consideration. For the experiment discussed here, one can deduce from the isolated case that flow over the frontal surfaces is sensitive to ZZ-strip positioning, and thus to changes to the boundary layer. It is, therefore, possible that the wake of the

leader triggered (earlier) separation at the front edges of the trailing model.

Looking back to earlier research into the bluff bodies in tandem, it seems that there are more examples of front-end flows being negatively affected by the wake of an upstream body. One could look for example at the flat plate in front of a bluff body with rounded edges experiment of [42], which has been covered in section 2.6, and to an example mentioned in [34]. In the latter example, two streamlined shapes are positioned in alignment with one another at varying separation distances. The excerpt from [34] shown in fig. 4.24 illustrates the drag coefficient of two aerodynamic struts in drafting configuration. Here, the trailing object experiences an increase in drag because the low momentum wake of the upstream strut creates a boundary layer that is prone to separation.

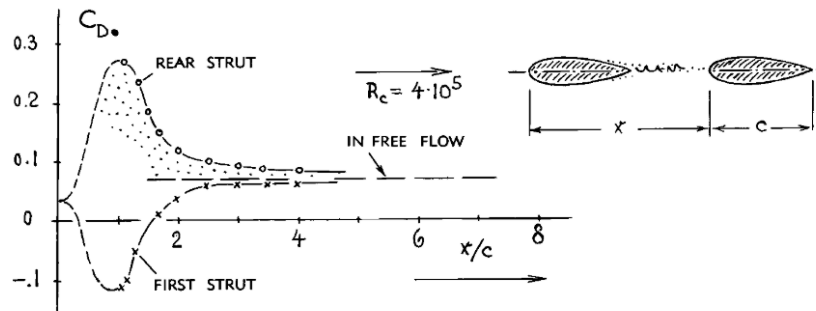


Figure 4.24: Drag coefficient of two streamlined struts in tandem. Figure reproduced from [34].

The discussion above raises the question of whether flow separation due to wake influences are also observed for full-scale vehicles. As shown by [13] (see section 2.3.3), front end separation occurs up until a critical Reynolds number, after which the flow remains attached and the drag coefficient decreases to a lower, stable value. While for isolated models the critical Reynolds number is well established, it is not clear whether the same critical Reynolds number applies for models immersed in low-momentum, turbulent wakes. Without a proper investigation of the critical Reynolds number for road vehicle models in tandem, the similarity between small-scale and full-scale model drag behavior while drafting remains uncertain.

#### 4.4.2. On bi-stability

Based on the pressure distribution for the Ahmed body in isolated condition and at zero degrees yaw, it seems highly likely that no bi-stable behavior has been observed during the presented experiments. What has likely been observed is one of the two reflectional symmetry breaking orientations presenting itself continuously. This hypothesis seems to be confirmed by the average flow field behind the isolated model as observed by CVV. However, one must be careful to consider the reported timescale of the bi-stable behavior relative to the acquisition time of the CVV measurement. The switches should happen randomly, but the average time between the switches was reported as 5.3 seconds in [27]. For the isolated Ahmed body flow field presented in this report, 3000 images were shot per illuminated cone. This takes just over 4 seconds at 700 Hz. Eight cones were used to construct the flow field, which means that around 34 seconds of flow was recorded. Transit times between positions of the robotic arm are excluded from this total. Even if bi-stability had occurred, such a short recording time could leave a significant bias in the orientation of the wake. Therefore, it is the asymmetry in the repeated pressure measurements, which took around 100 seconds per sample, which gives the strongest evidence of the single-sided asymmetric wake. The CVV derived flow field does agree with the pressure measurements in its orientation.

What could cause the continuously single-sided asymmetric wake? An obvious assumption is that some asymmetry in either the model or the setup must have prevented the wake from changing states. Proof of the sensitivity of the wake to alignment with the freestream is provided in several reports on the Ahmed body and similar models [20, 29, 56]. One of the earlier observations of the bi-stable condition has been behind a rectangular base of a three-dimensional backward-facing step by [33]. Using accurate positioning equipment, the latter research found that the wake was very sensitive to the angle of the base with respect to the oncoming flow (sideslip angle of the model). Small deviations from the zero-sideslip condition triggered one of the two bi-stable conditions to exist predominantly, as exemplified by fig. 4.25. The authors noted that within a range of  $0.45^\circ$  around the zero-sideslip setup, the wake states would switch randomly, but beyond that range only

one state was dominant. Similarly, Grandemange noticed that bi-stability was sensitive to sideslip. In [30] it was noted that bi-stability was limited to a window of  $\pm 0.5^\circ$  for a large Ahmed body model ( $Re = 2.5 \times 10^6$ ). Similarly, in [20] a precise yaw angle sweep was performed to measure the sensitivity of the wake orientation. Not only was the window for which bi-stable behavior was measured as narrow as reported earlier, but the local orientation of the jet in the wind tunnel and minor geometrical changes to the model were sufficient to skew the results.

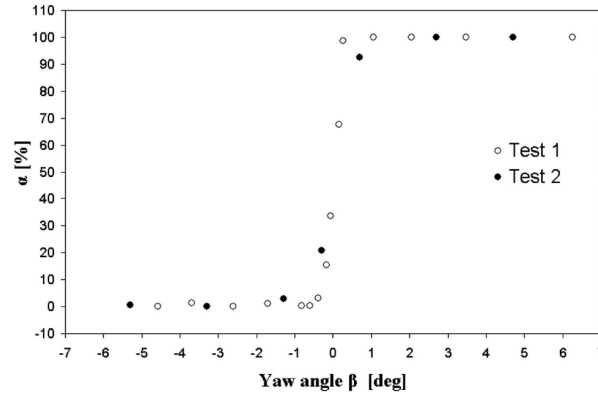


Figure 4.25: Likelihood of observing either state in a bi-stable system as a function of sideslip angle.  $\alpha$  is indicative of the likelihood of observing states  $B_1$  or  $B_2$ , as expressed by  $A = \alpha B_1 + (1-\alpha)B_2$ , where  $A$  indicates the flow field as averaged over a long time interval. Figure reproduced from [33]

For the experiments presented here, alignment of the models with the oncoming flow was performed by visually aligning markers on the models with markers in the nozzle. In the process, small yaw angles could have been introduced, which could explain the bias. However, random alignment errors are likely to occur in both directions, i.e. both left and right sideslip angles should be introduced. Yet, all observations of pressure coefficient, side force, and CVV show the same state of the wake. It is, of course, possible that there has been a constant alignment error bias (perhaps in the marker locations), but it could also be that some inherent asymmetry of the model forced the wake state.

Whatever the exact reason for the asymmetry may be, one can conclude from the examples in literature that observing the bi-stable wake is limited to a very narrow band of sideslip. Thus, precision alignment instrumentation is required if one wishes to examine the bi-stable condition. Furthermore, for full-scale vehicles under realistic road conditions, it is unlikely that the airflow will be neatly aligned. Therefore, one needs to question the relevance of the bi-stable wake in full-scale applications. Relating to the measured drag coefficient, as the bi-stable states are mirror images of one another, the drag coefficient of a single state will likely not differ much from a bi-stable wake. The induced drag due to side force should be equal for both states [29, 56].

When the trailing model is positioned in the wake and aligned with the leading model, the average lateral component of the pressure gradient weakens. The average wake becomes more symmetric, but still, no bi-stable behavior is recorded. A more symmetric wake likely reduces the induced drag due to side force. Indeed, the side force coefficient  $C_{y^*}$  of the leading model is lower when the model is in an aligned platoon, compared to the isolated case. Therefore, part of the drag savings of the leading model while platooning could be due to forced symmetry of the wake. In [27], it was shown that it is possible to force the wake of the Ahmed body to a stable symmetric state, with a control cylinder in the recirculation region. The presented results suggest that the trailing model might have a similar effect.

#### 4.4.3. On the influence of lateral stagger

Next, let us consider the principle on which the lateral offset influences the flow field, the pressure distribution, and therefore the drag of the platoon. Starting with the trailing model, it must be stated that without knowledge of the flow field around-, or the pressure on-, the curved parts of the front-end of the trailing model, it is hard to explain exactly why it experiences higher drag due to stagger. One explanation could be that stagger exposes more of the trailing model to the freestream, which is at a higher velocity than the wake. But it could also be that some other principle is key. For instance, the observed lateral crossflow across the nose might promote separation to the side exposed to the wake, while the side exposed to the freestream could potentially see more attached flow.

On the other hand, with the available force-, pressure-, and CVV measurements, more information is available to describe how the leader of the platoon is affected by lateral stagger and separation distance. Measurements show that across the entire rear face of the leading model, the pressure is increased when another model is placed in its wake. It is safe to assume that all drag gains are due to increased pressure across the rear face. The CVV images of the mean flow at the  $60\%L$  separation distance show that when the models are aligned, the recirculation zone is enclosed by the separating shear layers and the trailing model. However, when lateral misalignment is introduced, the recirculation zone is only bounded by the shear layers, which meet in a saddle point. Between the saddle point and the front end of the trailing model, crossflow is observed. However, the basic shape of the recirculation zone does not change much, and thus the pressure distribution across the rear of the leading model remains roughly similar.

When at  $0\%W$  lateral stagger and  $20\%L$  longitudinal separation, the recirculation region is bounded by shear layers that flow smoothly onto the trailing vehicle, and the trailing vehicle itself. However, as stagger is introduced, one shear layer flows past the nose of the trailing vehicle. As has been shown in section 2.2, mass is entrained along the shear layer that passes the gap and thus accelerated downstream. There is no local return flow, as that shear layer does not stagnate on the front of the trailing model, and does not turn far enough inboard to form a free stagnation point as we have seen in the case of  $60\%L$  separation and  $-25\%W$  stagger. On the side of the excursion however, freestream flow will stagnate on the nose of the trailing model. To maintain mass continuity in the gap between the models for the new situation means that the mass flow out of the gap due to the passing shear layer will need to be balanced by inflow on the side of the stagnating streamline. Thus, a crossflow will need to establish itself. The strong curvature of the flow at the side of the lateral excursion can only exist if a strong radial pressure gradient exists with lower pressures on the inboard turn. This radial pressure gradient would explain the pressure pattern across the rear face of the leading model. The asymmetric inflow/outflow condition also prohibits the occurrence of a toroidal vortex, and in turn, creates the horse-shoe type vortex that is seen in the CVV measurements. A schematic representation of the flow discussed in this paragraph can be found in fig. 4.26.

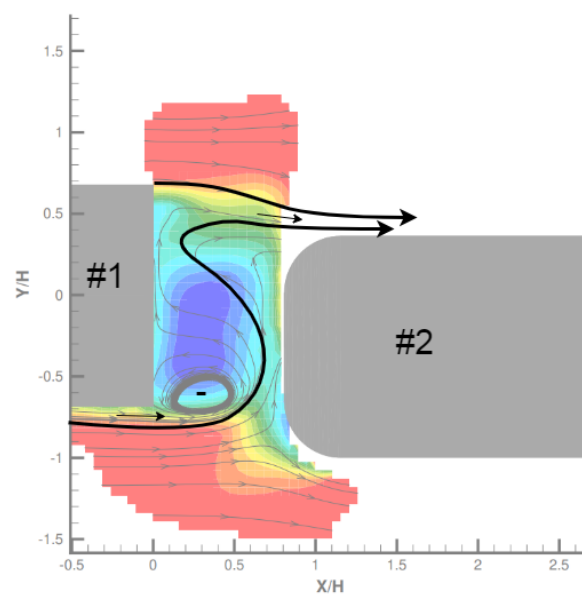


Figure 4.26: Schematic top view representation of gap flow for a platoon at  $-25\%W$  lateral stagger and  $20\%L$  longitudinal separation. Mass flow enters the region bounded by the streamlines on the left, and is expelled at the right side. Exiting flow is due to entrainment from mixing layer. The minus sign indicates area of low pressure required to turn freestream flow into the gap.



# 5

## Conclusion & Recommendations

### 5.1. Conclusions

In this report, the aerodynamic interaction effects between platooning heavy-duty vehicles have been simulated by a two-vehicle convoy of scaled, squareback Ahmed bodies in a wind-tunnel. Results from load cells, pressure taps, and Coaxial Volumetric Velocimetry have been combined to characterize the drag behavior of the models, and explain it through the topology of the flow field. Not only were the models tested at separation distances of 20%, 40%, and 60%  $L$  in the laterally aligned configuration, but also in multiple laterally misaligned scenarios which should represent real-world driving conditions.

According to the load cell results, lateral stagger has a clear detrimental effect on drag for both models at longitudinal separation distances of 20% $L$ , and 40% $L$ . At 60% $L$  the effect of lateral stagger is less pronounced. The drag penalty for both models due to lateral stagger is largest at the shortest longitudinal separation distance of 20% $L$ , and decreases for the larger separation distances. However, when the platoon is laterally aligned, minimum drag is measured at the shortest separation distance. Pressure tap measurements across the rear face of the leading model agree with the general results of the leading model load cell. Mean base pressure decreases with lateral stagger for longitudinal separation distances of 20% $L$ , and 40% $L$ , while at 60% $L$  no significant change is observed. For all platooning setups, the trailing model experiences higher drag than it would in isolation, while the leading model's drag coefficient is mostly lower than its isolated value. Although, based on the available literature, several causes can be suggested for the increased drag; the presented study cannot confirm which ones apply.

Three-dimensional mean fluid velocity field recordings of the near-wake of an isolated Ahmed body present recirculation region which is asymmetric as seen from the top. It shows visual similarity with one of the reflectional symmetry breaking wake states observed in several recent studies. The pressure tap results confirm that the asymmetric wake has been present for the duration of several measurement series, each of around 90 seconds. The typical bi-stable wake behavior, which is described in the mentioned studies, has thus not been observed. This is not surprising considering the very narrow window of yaw angles, and various other factors to which the wake is sensitive, for which bi-stability might manifest itself.

With the trailing vehicle laterally aligned behind the leader, and at 60% $L$  longitudinal separation, the recirculating wake appears to become more symmetric. Even when the platoon model is misaligned by -25% $W$ , the recirculation region retains its symmetrical appearance. The general topology of the near-wake does not appear to change. For the platoon with no lateral stagger at 20% $L$ , a toric recirculating structure is visible in the gap between the models, and the shear layers separating from the rear of the leading model align with the sides of the rear model. However, at -25% $W$  lateral stagger, the topology of the gap flow changes significantly. The torus breaks and changes in a horseshoe vortex which ends leave the gap and flow in the downstream direction. This dramatic change in topology is reflected in the pressure contour across the rear face of the leading model, and agrees well with the observed increases in drag coefficient due to lateral stagger for the closest tested separation distance.

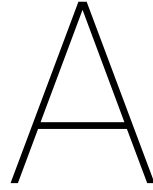
To finalize the conclusions of this study, one should try to put the findings into the context of a full-scale HDV platoon. As has been shown, offsets of 15% of vehicle width were already noticeable in these scaled tests. Furthermore, if the vehicle width is assumed to be 2.5 meters (a reasonable estimate for HDV width) then the platoon at the tested extreme lateral offset of 25% $W$  would still fit within European highway lanes of

around 3.2-3.5 meters. If one is to assume that the observed flow phenomena are representative of full-scale flow, then within-lane position keeping should become a concern for platooning systems at close following distances.

## 5.2. Recommendations

In the discussion of the results in section 4.4, some deficiencies in the setup of the presented experiment were mentioned. The main issue being the lack of data on the trailing model. Apart from the observed increase in drag for all platooning configurations, no information about pressure distribution or flow field around the nose-section of model #2 was recorded. Yet, in literature, both drag increases and decreases have been observed for trailing models in platoons of similar vehicle types, and thus a more complete discussion of drafting effects on the trailing model would be welcome. Direct pressure measurement with pressure taps, or possibly indirect measurements by interpolating PIV data [? ], would allow one to distinguish the source of drag changes. Additionally, the influence of the ZZ strip positioning on the drag coefficient, demonstrated in this work, highlights the sensitivity of the boundary layer on the models. Results obtained on this scale might not extrapolate to full-scale vehicles, as low-momentum wakes can impact vehicles at low Reynolds numbers differently than at full-scale Reynolds numbers. Ideally, a study into the effects of Reynolds number on platooning would shed light on the uncertainties.

Another area of uncertainty in extrapolating the results of this thesis to full-scale models is the influence of base aspect ratios (model height versus width). Realistic HDVs are relatively taller than the Ahmed Body. Although research into the effects of aspect ratio on the near-wake exists for isolated models [29]; just how it would influence the results presented in this thesis, or drafting in general, has not yet been investigated.



# Wind tunnel force measurement corrections

The correction procedure for open-jet type wind tunnels with high blockage models installed in the test section has been the topic of a long and relatively recent discussion. Where in the beginning, some considered open-jet type wind tunnels to be correction-free [53], it is now beyond doubt that results obtained in such wind tunnels should be corrected carefully when comparing data from different wind-tunnels or even between different models in the same wind-tunnel. The approach to corrections described in [53] has formed the basis on which subsequent research, such as [15, 51, 52], has improved the procedure of obtaining accurate correction factors. However, for the presented results the original correction procedure of [53] has been used rather than the updated method described in e.g. [15]. The original method requires fewer measurements and measurement equipment, while still achieving considerable success in eliminating interference. Considering the scatter in the force measurements due to (lack of) load cell accuracy, the applied corrections should be sufficient for the measurements in this report.

For open-jet type of wind tunnels, five interference effects can be identified. They are listed below, and a visual interpretation is found in figs. A.1 and A.2.

1. **Jet Expansion** This effect is also known as classical solid blockage. The jet in a wind tunnel is of finite cross-section, while a realistic stream is infinite. When an object displaces streamlines, then in realistic conditions the ambient pressure is theoretically observed at infinity away from the object. However, in a finite jet, the streamline at the edge is always at a static pressure equal to that of the plenum (ambient pressure). Therefore, the streamlines deflected by an object cause an over-expansion of the jet, and thus lower average flow velocity at the object.

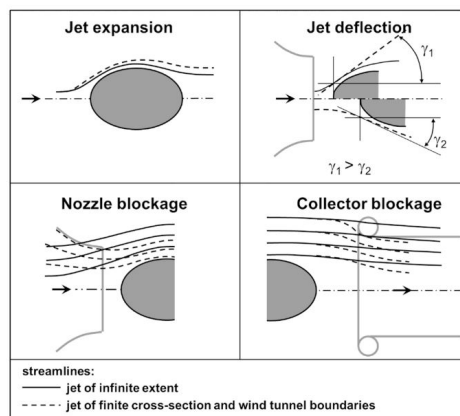


Figure A.1: Interference effects of open-jet wind tunnel and object. Image reproduced from [21], original by [36].

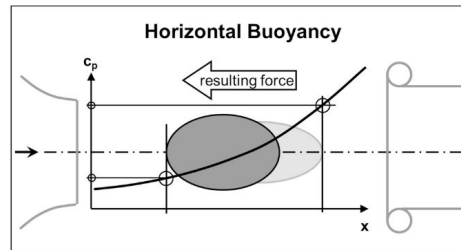


Figure A.2: Example of horizontal buoyancy effect of model in test-section. Image reproduced from [21].

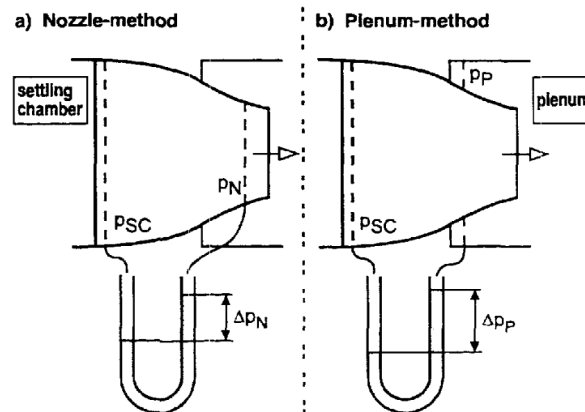


Figure A.3: Differential pressure measurements for either nozzle or plenum method. Figure reproduced from [52].

2. **Jet Deflection** Similarly to the above-mentioned expansion effect, the proximity of the nozzle to the model can cause an expansion of the outer streamlines of the jet. This will lead to lower average flow velocities at the object.
3. **Nozzle Blockage** The nozzle throat area restricts the expansion of streamlines upstream of the model, which narrows the jet compared to the unrestricted situation. This effect is similar to local flow acceleration, which can be felt even at the model's location.
4. **Collector Blockage** When the jet is displaced by the wake of the object, the collector will force it to fit a decreased cross-sectional area, rather than letting it continue unchanged. The result is that flow is accelerated downstream, which again can be felt at the model location.
5. **Horizontal Buoyancy** If a streamwise pressure gradient exists, such as shown in fig. A.2, then a force will be exerted on the object in the direction of the nozzle. This will decrease the measured drag of the object.

In the method of [53], the blockage corrections are expressed as increases to the measured freestream dynamic pressure  $q_{\infty}$ , as shown in eq. (A.1). The correction factors are denoted by  $\epsilon$  and the subscripts  $S$ ,  $C$ ,  $N$  for Solid Blockage, Collector blockage and Nozzle blockage respectively. The jet deflection blockage is included in the solid blockage term.

$$q_{cor}/q_{\infty} = (1 + \epsilon_S + \epsilon_C + \epsilon_N)^2 \quad (\text{A.1})$$

The horizontal buoyancy  $\Delta C_{D_{HB}}$  is added to the measured drag coefficient  $C_{D_m}$ , and then scaled by the corrected dynamic pressure  $q_{cor}/q_{\infty}$  according to eq. (A.2)

$$C_{D_{cor}} = (C_{D_m} + \Delta C_{D_{HB}})/(q_{cor}/q_{\infty}) \quad (\text{A.2})$$

Calculating the correction factors and the horizontal buoyancy is relatively straightforward, and a full explanation is left outside this report, as it can be found in [53]. However, two aspects of the correction method will be discussed in more detail as they deviate from the standard.

In [53] the method of measuring the dynamic pressure in the jet and its relation to the blockage correction is discussed, and the topic is further contemplated upon in [52]. The two most popular methods for dynamic pressure measurement will give very different drag coefficients at the same dynamic pressure reading. The two methods are known as the plenum-method and the nozzle-method. For both methods, the pressure difference between two locations is measured and related to the dynamic pressure via a calibrated constant  $k$ , as per eq. (A.3). As shown in fig. A.3, pressure differences are taken between the settling chamber (sc) and either a position in the nozzle (N) or in the plenum chamber (P). Usually, to minimize the influence of local flow disturbances, multiple pressure ports are used per location for an average pressure reading. Interestingly, for the W-tunnel, dynamic pressure is measured with a single pitot-static tube, mounted to the upper surface of the final (straight) section of the nozzle. Such a method is not mentioned explicitly in [53] nor [52], but it was reasoned that the nozzle-method correction was the most appropriate for the current application. The nozzle-method correction is applied under the assumption that the cross-sectional velocity is constant at the location of the pitot tube, and thus the dynamic pressure measurement is representative of the nozzle cross-section. The second assumption is that the average dynamic pressure at the nozzle exit plane should be equal to the average dynamic pressure at the pitot probe location, as the planes are of equal cross-sectional area and the continuity equation applies.

$$q_{\infty} = k_n(p_{sc} - p_n) = k_p(p_{sc} - p_p) \quad (\text{A.3})$$

The second deviation from the original correction procedure described in [53] concerns the nozzle blockage correction. The magnitude of the correction depends on both its application location and the location of the “source” of the disturbance that distorts the flow in the nozzle in the first place. Typically, for a single model, these locations are essentially the same. However, in platooning setups with multiple models there are as many application locations as there are models. Yet, the disturbance, on the other hand, should be based on the leading model, considering it is at proximity to the nozzle. Therefore, for all platooning measurements, the location of the upstream disturbance used to calculate the nozzle blockage corresponds to the leading vehicle model.

Similar issues could arise for the collector blockage if the collector would be close to the last model in the platoon. However, as for the current study the collector is rather large and far downstream of even the most aft model position, its influence is marginal, and there is no need to improve the correction.



# Bibliography

- [1] S.R. Ahmed, G. Ramm, and G. Falin. Some Salient Features Of The Time-Averaged Ground Vehicle Wake. In *SAE Trans.*, volume 93, pages 473–503, 1984. ISBN 0148-7191. doi: 10.4271/840300. URL <http://papers.sae.org/840300/>.
- [2] Assad Al Alam, Ather Gattami, and Karl Henrik Johansson. An experimental study on the fuel reduction potential of heavy duty vehicle platooning. In *13th Int. IEEE Conf. Intell. Transp. Syst.*, pages 306–311. IEEE, sep 2010. ISBN 978-1-4244-7657-2. doi: 10.1109/ITSC.2010.5625054. URL <http://ieeexplore.ieee.org/document/5625054/>.
- [3] Tom Alkim, Arjan van Vliet, Loes Aarts, and Jacqueline Eckhardt. Hypothesis and recommendations for future cross border Field Operational Tests of truck platooning in Europe: Lessons Learnt. Technical report, 2016. URL <https://www.eutruckplatooning.com/default.aspx>.
- [4] P. W. Bearman. Bluff body flows applicable to vehicle aerodynamics. *J. Fluids Eng. Trans. ASME*, 102(3): 265–274, 1980. ISSN 1528901X. doi: 10.1115/1.3240679.
- [5] D. Bevly, C. Murray, A. Lim, R. Turochy, R. Sesek, S. Smith, G. Apperson, J. Woodruff, S. Gao, M. Gordon, N. Smith, A. Watts, J. Batterson, R. Bishop, D. Murray, F. Torrey, A. Korn, J. Switkes, and S. Boyd. Heavy Truck Cooperative Adaptive Cruise Control: Evaluation, Testing, and Stakeholder Engagement for Near Term Deployment: Phase One Final Report. Technical report, Auburn University, 2015.
- [6] David Bevly, Chase Murray, Alvin Lim, Rod Turochy, Richard Sesek, Scott Smith, Luke Humphreys, Grant Apperson, Jonathan Woodruff, Song Gao, Mikhail Gordon, Nicholas Smith, Shraddha Prharaj, Joshua Batterson, and Richard Bishop. Heavy Truck Cooperative Adaptive Cruise Control: Evaluation, Testing, and Stakeholder Engagement for Near Term Deployment: Phase Two Final Report. Technical report, 2017. URL <http://atri-online.org/wp-content/uploads/2017/04/FHWA{ }AuburnDATP{ }Phase2FinalReport.pdf>.
- [7] Richard Bishop, David Bevly, Luke Humphreys, Stephen Boyd, and Daniel Murray. Evaluation and Testing of Driver-Assistive Truck Platooning: Phase 2 Final Results. *Transp. Res. Rec. J. Transp. Res. Board*, 2615(1):11–18, jan 2017. ISSN 0361-1981. doi: 10.3141/2615-02. URL <http://journals.sagepub.com/doi/10.3141/2615-02>.
- [8] Christophe Bonnet and Hans Fritz. Fuel Consumption Reduction in a Platoon: Experimental Results with two Electronically Coupled Trucks at Close Spacing. Number 724, aug 2000. doi: 10.4271/2000-01-3056. URL <http://papers.sae.org/2000-01-3056/https://www.sae.org/content/2000-01-3056/>.
- [9] R Bradley. Technology Roadmap for the 21st Century Truck Program, a government-industry research partnership. Technical Report December, USDOE Office of Energy Efficiency and Renewable Energy (EE), Oak Ridge, Tennessee, dec 2000. URL <http://www.osti.gov/servlets/purl/777307-BKSUFs/native/>.
- [10] Fred Browand, John Mearthur, and Charles Radovich. Fuel Saving Achieved in the Field Test of Two Tandem Trucks. Technical report, UC Berkeley: California Partners for Advanced Transportation Technology, 2004. URL <https://escholarship.org/uc/item/29v570mm>.
- [11] Bureau of Transportation Statistics. Freight Shipments by Mode (2017), 2017. URL <https://www.bts.gov/topics/freight-transportation/freight-shipments-mode>.
- [12] Dean R. Chapman, Donald M. Kuehn, and Howard K. Larson. Investigation of Separated Flows in Supersonic and Subsonic Streams with Emphasis on the effect of Transition. Technical Report January, National Advisory Committee for Aeronautics. Ames Aeronautical Lab., Moffett Field, CA, United States, 1957. URL <https://ntrs.nasa.gov/search.jsp?R=19930092343>.

- [13] Kevin R. Cooper. The Effect of Front-Edge Rounding and Rear-Edge Shaping on the Aerodynamic Drag of Bluff Vehicles in Ground Proximity. In *Int. Congr. Expo.*, feb 1985. doi: 10.4271/850288. URL <https://www.sae.org/content/850288/>.
- [14] Kevin R. Cooper. Commercial Vehicle Aerodynamic Drag Reduction: Historical Perspective as a Guide. In Rose McCallen, Fred Browand, and James Ross, editors, *Aerodyn. Heavy Veh. Truck. Buses, Trains*, pages 9–28. Springer Berlin Heidelberg, Berlin, 2004. ISBN 978-3-540-44419-0. doi: 10.1007/978-3-540-44419-0\_2. URL [http://link.springer.com/10.1007/978-3-540-44419-0\\_{\\_}2](http://link.springer.com/10.1007/978-3-540-44419-0_{_}2).
- [15] Kevin R. Cooper, Edzard Mercker, and Jürg Müller. The necessity for boundary corrections in a standard practice for the open-jet wind tunnel testing of automobiles. *Proc. Inst. Mech. Eng. Part D J. Automob. Eng.*, 231(9):1245–1273, aug 2017. ISSN 0954-4070. doi: 10.1177/0954407017701287. URL <http://journals.sagepub.com/doi/10.1177/0954407017701287>.
- [16] Carlos B. da Silva, Julian C.R. Hunt, Ian Eames, and Jerry Westerweel. Interfacial Layers Between Regions of Different Turbulence Intensity. *Annu. Rev. Fluid Mech.*, 46(1):567–590, jan 2014. ISSN 0066-4189. doi: 10.1146/annurev-fluid-010313-141357. URL <http://www.annualreviews.org/doi/10.1146/annurev-fluid-010313-141357>.
- [17] Edward G. Duell and A. R. George. Experimental Study of a Ground Vehicle Body Unsteady Near Wake. In *1999 SAE Int. Congr. Expo.*, number 724, Detroit, Michigan, mar 1999. doi: 10.4271/1999-01-0812. URL <https://www.sae.org/content/1999-01-0812/>.
- [18] European Commission. Statistical pocketbook 2018: EU transport in figures. Technical report, Luxembourg, 2018.
- [19] European Union. Regulation (EU) 2019/1242 of the European Parliament and of the Council of 20 June 2019 setting CO2 emission performance standards for new heavy-duty vehicles and amending Regulations (EC) No 595/2009 and (EU) 2018/956 of the European Parliament and of th, 2019.
- [20] A. Evrard, O. Cadot, V. Herbert, D. Ricot, R. Vigneron, and J. Détery. Fluid force and symmetry breaking modes of a 3D bluff body with a base cavity. *J. Fluids Struct.*, 61:99–114, feb 2016. ISSN 08899746. doi: 10.1016/j.jfluidstructs.2015.12.001. URL <https://linkinghub.elsevier.com/retrieve/pii/S0889974615002698>.
- [21] Oliver Fischer. *Investigation of Correction Methods for Interference Effects in Open-Jet Wind Tunnels*. 2017. ISBN 9783658213787.
- [22] M. Gharib and A. Roshko. The effect of flow oscillations on cavity drag. *J. Fluid Mech.*, 177(11):501–530, 1987. ISSN 14697645. doi: 10.1017/S002211208700106X.
- [23] Thomas Gheysens. *Aerodynamic analysis of a platoon of bluff bodies subjected to cross wind, a numerical investigation on the effect of drag reduction devices*. Msc thesis, TU Delft, 2016.
- [24] Thomas Gheysens and Gandert Van Raemdonck. Effect of the Frontal Edge Radius in a Platoon of Bluff Bodies. *SAE Int. J. Commer. Veh.*, 9(2):371–380, 2016. ISSN 1946-3928. doi: 10.4271/2016-01-8149.
- [25] Danielle Giaquinta. *The Flow Topology of the Ahmed Body in Cross-Wind*. PhD thesis, TU Delft, 2018.
- [26] M. Grandemange, M. Gohlke, V. Parezanović, and O. Cadot. On experimental sensitivity analysis of the turbulent wake from an axisymmetric blunt trailing edge. *Phys. Fluids*, 24(3), 2012. ISSN 10706631. doi: 10.1063/1.3694765.
- [27] M. Grandemange, M. Gohlke, and O. Cadot. Turbulent wake past a three-dimensional blunt body. Part 1. Global modes and bi-stability. *J. Fluid Mech.*, 722:51–84, 2013. ISSN 00221120. doi: 10.1017/jfm.2013.83.
- [28] M. Grandemange, M. Gohlke, and O. Cadot. Turbulent wake past a three-dimensional blunt body. Part 2. Experimental sensitivity analysis. *J. Fluid Mech.*, 752(5):439–461, 2014. ISSN 14697645. doi: 10.1017/jfm.2014.345.
- [29] Mathieu Grandemange. *Analysis and Control of Three-dimensional Turbulent Wakes: from Axisymmetric Bodies to Road Vehicles*. Phd, École Polytechnique — ENSTA ParisTech, 2013. URL <https://pastel.archives-ouvertes.fr/pastel-00947364>.

- [30] Mathieu Grandemange, O Cadot, A Courbois, V Herbert, D Ricot, T Ruiz, and R Vigneron. Journal of Wind Engineering A study of wake effects on the drag of Ahmed ' s squareback model at the industrial scale. *Jnl. Wind Eng. Ind. Aerodyn.*, 145:282–291, 2015. ISSN 0167-6105. doi: 10.1016/j.jweia.2015.03.004. URL <http://dx.doi.org/10.1016/j.jweia.2015.03.004>.
- [31] Walter T Gutierrez, Basil Hassan, Robert H Croll, and Walter H Rutledge. Aerodynamics Overview of the Ground Transportation Systems (GTS) Project for Heavy Vehicle Drag Reduction. In *1996 SAE Int. Congr. Expo.*, Detroit, Michigan, feb 1996. doi: 10.4271/960906. URL <https://www.sae.org/content/960906/>.
- [32] Mustapha Hammache and Fred Browand. On the Aerodynamics of Tractor-Trailers. In Rose McCallen, Fred Browand, and James Ross, editors, *Aerodyn. Heavy Veh. Truck. Buses, Trains*, pages 185–205. Springer Berlin Heidelberg, 2004. ISBN 978-3-540-44419-0. doi: 10.1007/978-3-540-44419-0\_20. URL [http://link.springer.com/10.1007/978-3-540-44419-0\\_{\\_}20](http://link.springer.com/10.1007/978-3-540-44419-0_{_}20).
- [33] Benjamin B. Herry, Laurent Keirsbulck, Larbi Labraga, and Jean Bernard Paquet. Flow bistability downstream of three-dimensional double backward facing steps at zero-degree sideslip. *J. Fluids Eng. Trans. ASME*, 133(5):1–4, 2011. ISSN 00982202. doi: 10.1115/1.4004037.
- [34] S. F. Hoerner. Fluid Dynamic Drag, 1965. ISSN 1382-3256.
- [35] I. Hucho. Aerodynamics of Road Vehicles. *Annu. Rev. Fluid Mech.*, 25(1):485–537, 1993. ISSN 00664189. doi: 10.1146/annurev.fluid.25.1.485. URL <http://fluid.annualreviews.org/cgi/doi/10.1146/annurev.fluid.25.1.485>.
- [36] Wolf-Heinrich Hucho. *Aerodynamik des Automobils*. 2013. ISBN 978-3-8348-1919-2. doi: 10.1007/978-3-8348-2316-8.
- [37] Hugh Humphreys and David Bevly. Computational Fluid Dynamic Analysis of a Generic 2 Truck Platoon. In *SAE Tech. Pap. 2016-01-8008*, sep 2016. doi: 10.4271/2016-01-8008. URL <https://www.sae.org/content/2016-01-8008/>.
- [38] Robbert Janssen, Han Zwijnenberg, Iris Blankers, and Janiek De Kruijff. Truck Platooning Driving the Future of Transportation Executive Summary. Technical Report February, 2015.
- [39] Constantin Jux. *Robotic Volumetric Particle Tracking Velocimetry by Coaxial Imaging and Illumination*. PhD thesis, 2017.
- [40] Constantin Jux, Andrea Sciacchitano, Jan F.G. Schneiders, and Fulvio Scarano. Robotic volumetric PIV of a full-scale cyclist. *Exp. Fluids*, 59(4):1–15, 2018. ISSN 07234864. doi: 10.1007/s00348-018-2524-1. URL <http://dx.doi.org/10.1007/s00348-018-2524-1>.
- [41] Bahram Khalighi, S. Zhang, C. Koromilas, S. R. Balkanyi, Luis P. Bernal, G. Iaccarino, and P. Moin. Experimental and computational study of unsteady wake flow behind a bluff body with a drag reduction device. *SAE Tech. Pap.*, (January 2015), 2001. ISSN 26883627. doi: 10.4271/2001-01-1042.
- [42] Keith Koenig. *Interference effects on the drag of bluff bodies in tandem*. Phd thesis, California Institute of Technology, 1978. URL <https://resolver.caltech.edu/CaltechETD:etd-12042006-140552>.
- [43] Keith Koenig and Anatol Roshko. An experimental study of geometrical effects on the drag and flow field of two bluff bodies separated by a gap. *J. Fluid Mech.*, 156(-1):167, jul 1985. ISSN 0022-1120. doi: 10.1017/S002211208500204X. URL [http://www.journals.cambridge.org/abstract\\_{\\_}S002211208500204X](http://www.journals.cambridge.org/abstract_{_}S002211208500204X).
- [44] Michael Lammert, Kenneth Kelly, and Janet Yanowitz. Correlations of Platooning Track Test and Wind Tunnel Data. Technical Report February, 2018. URL [www.nrel.gov/publications](http://www.nrel.gov/publications).
- [45] Michael P. Lammert, Adam Duran, Jeremy Diez, Kevin Burton, and Alex Nicholson. Effect of Platooning on Fuel Consumption of Class 8 Vehicles Over a Range of Speeds, Following Distances, and Mass. *SAE Int. J. Commer. Veh.*, 7(2):2014–01–2438, sep 2014. ISSN 1946-3928. doi: 10.4271/2014-01-2438. URL <http://papers.sae.org/2014-01-2438/>.

- [46] Drew Landman, Richard Wood, Whitney Seay, and John Bledsoe. Understanding Practical Limits to Heavy Truck Drag Reduction. *SAE Int. J. Commer. Veh.*, 2(2):183–190, 2009. ISSN 1946-3928. doi: 10.4271/2009-01-2890.
- [47] Brian McAuliffe, Michael Lammert, Xiao-Yun Lu, Steven Shladover, Marius-Dorin Surcel, and Aravind Kailas. Influences on Energy Savings of Heavy Trucks Using Cooperative Adaptive Cruise Control. In *WCX World Congr. Exp.*, number April, Detroit, Michigan, apr 2018. doi: 10.4271/2018-01-1181. URL <http://www.sae.org/content/2018-01-1181/>.
- [48] Brian R. McAuliffe and Mojtaba Ahmadi-Baloutaki. A Wind-Tunnel Investigation of the Influence of Separation Distance, Lateral Stagger, and Trailer Configuration on the Drag-Reduction Potential of a Two-Truck Platoon. *SAE Int. J. Commer. Veh.*, 11(2):02–11–02–0011, jun 2018. ISSN 1946-3928. doi: 10.4271/02-11-02-0011. URL <http://www.sae.org/content/02-11-02-0011/>.
- [49] Brian R McAuliffe, Mark Croken, Mojtaba Ahmadi-Baloutaki, and Arash Raeesi. Fuel economy testing of a three vehicle truck platooning system. Technical report, National Research Council Canada. Aerospace. Aerodynamics Laboratory, 2017. URL <http://nparc.nrc-cnrc.gc.ca/eng/view/object/?id=d21e1097-5d30-4a0f-b742-35ffad931c2f>.
- [50] Doug McLean. *Understanding Aerodynamics: Arguing from the Real Physics*. 2012. ISBN 9781119967514. doi: 10.1002/9781118454190.
- [51] E. Mercker, K. R. Cooper, O. Fischer, and J. Wiedemann. The Influence of a Horizontal Pressure Distribution on Aerodynamic Drag in Open and Closed Wind Tunnels. apr 2005. doi: 10.4271/2005-01-0867. URL <https://www.sae.org/content/2005-01-0867/>.
- [52] Edzard Mercker. Contemplation of Nozzle Blockage in Open Jet Wind-Tunnels in View of Different 'Q' Determination Techniques. *SAE Tech. Pap.*, (412), 1997.
- [53] Edzard Mercker and Jochen Wiedemann. On the correction of interference effects in open jet wind tunnels. *SAE Tech. Pap.*, (412), 1996. ISSN 26883627. doi: 10.4271/960671.
- [54] Mark Michaelian and Fred Browand. Field experiments demonstrate fuel savings for close-following. Technical report, 2000.
- [55] Jhon Norris and Giulia Escher. Heavy Duty Vehicles Technology Potential and Cost Study. (5):96p, 2017. URL <https://www.theicct.org/sites/default/files/publications/HDV-Technology-Potential-and-Cost-Study{ }Ricardo{ }Consultant-Report{ }26052017{ }vF.pdf>.
- [56] Giancarlo Pavia, Martin Passmore, and Costantino Sardu. Evolution of the bi-stable wake of a square-back automotive shape. *Exp. Fluids*, 59(1):20, jan 2018. ISSN 0723-4864. doi: 10.1007/s00348-017-2473-0. URL <http://dx.doi.org/10.1007/s00348-017-2473-0><http://link.springer.com/10.1007/s00348-017-2473-0>.
- [57] Anna-Kristina Perry, Giancarlo Pavia, and Martin Passmore. Influence of short rear end tapers on the wake of a simplified square-back vehicle: wake topology and rear drag. *Exp. Fluids*, 57(11):169, nov 2016. ISSN 0723-4864. doi: 10.1007/s00348-016-2260-3. URL <http://link.springer.com/10.1007/s00348-016-2260-3>.
- [58] Anirudh N. Rao, Jie Zhang, Guglielmo Minelli, Branislav Basara, and Siniša Krajnović. An LES Investigation of the Near-Wake Flow Topology of a Simplified Heavy Vehicle. *Flow, Turbul. Combust.*, 102(2): 389–415, 2019. ISSN 15731987. doi: 10.1007/s10494-018-9959-6.
- [59] A. Roshko. Perspectives on bluff body aerodynamics. *J. Wind Eng. Ind. Aerodyn.*, 49(1-3):79–100, dec 1993. ISSN 01676105. doi: 10.1016/0167-6105(93)90007-B. URL <https://linkinghub.elsevier.com/retrieve/pii/016761059390007B>.
- [60] A. Roshko and K. Koenig. Interaction Effects on the Drag of Bluff Bodies in Tandem. *Aerodyn. Drag Mech. Bluff Bodies Road Veh.*, 1978. doi: 10.1007/978-1-4684-8434-2\_10.

- [61] Anatol Roshko. Structure of Turbulent Shear Flows: A New Look. *AIAA J.*, 14(10):1349–1357, oct 1976. ISSN 0001-1452. doi: 10.2514/3.61477. URL <https://arc.aiaa.org/doi/10.2514/3.61477>.
- [62] Kambiz Salari and Jason Ortega. Experimental Investigation of the Aerodynamic Benefits of Truck Platooning. pages 1–11, apr 2018. doi: 10.4271/2018-01-0732. URL <http://www.sae.org/content/2018-01-0732/>.
- [63] Edwin J Saltzman and Robert R Meyer. A Reassessment of Heavy-Duty Truck Aerodynamic Design Features and Priorities The NASA STI Program Office...in Profile. (June), 1999. URL <https://www.nasa.gov/centers/dryden/pdf/88628main{ }H-2283.pdf>.
- [64] Fulvio Scarano, Sina Ghaemi, Giuseppe Carlo Alp Caridi, Johannes Bosbach, Uwe Dierksheide, and Andrea Sciacchitano. On the use of helium-filled soap bubbles for large-scale tomographic PIV in wind tunnel experiments. *Exp. Fluids*, 56(2), 2015. ISSN 07234864. doi: 10.1007/s00348-015-1909-7.
- [65] Daniel Schanz, Sebastian Gesemann, and Andreas Schröder. Shake-The-Box: Lagrangian particle tracking at high particle image densities. *Exp. Fluids*, 57(5):1–27, 2016. ISSN 07234864. doi: 10.1007/s00348-016-2157-1.
- [66] Jan E.G. Schneiders, Fulvio Scarano, Constantin Jux, and Andrea Sciacchitano. Coaxial volumetric velocimetry. *Meas. Sci. Technol.*, 29(6), 2018. ISSN 13616501. doi: 10.1088/1361-6501/aab07d.
- [67] Andrea Sciacchitano and Fulvio Scarano. Elimination of PIV light reflections via a temporal high pass filter. *Meas. Sci. Technol.*, 25(8), 2014. ISSN 13616501. doi: 10.1088/0957-0233/25/8/084009.
- [68] R Sims, R Schaeffer, F Creutzig, X Cruz-Núñez, M D’Agosto, D Dimitriu, M J Figueroa Meza, L Fulton, S Kobayashi, O Lah, A McKinnon, P Newman, M Ouyang, J J Schauer, D Sperling, and G Tiwari. Transport. In Edenhofer, R Pichs-Madruga O., Y Sokona, E Farahani, S Kadner, K Seyboth, A Adler, I Baum, S Brunner, P Eickemeier, B Kriemann, J Savolainen, S Schlömer, C von Stechow, T Zwickel, and J C Minx, editors, *Clim. Chang. 2014 Mitig. Clim. Chang. Contrib. Work. Gr. III to Fifth Assess. Rep. Intergov. Panel Clim. Chang.*, Cambridge, United Kingdom and New York, NY, USA, 2014. Cambridge University Press.
- [69] Gino Sovran. Tractive-Energy-Based Formulae for the Impact of Aerodynamics on Fuel Economy Over the EPA Driving Schedules. *SAE Trans.*, 92:1039–1050, 1983. ISSN 0096736X, 25771531. URL <http://www.jstor.org/stable/44644433>.
- [70] David Sujudi and Robert Haimes. Identification of swirling flow in 3-D vector fields. *12th Comput. Fluid Dyn. Conf.*, pages 792–799, 1995. doi: 10.2514/6.1995-1715.
- [71] O. G. Tietjens, L. Prandtl, and J. P. Den Hartog. *Applied hydro- and aeromechanics*. 1934.
- [72] Frank Van Tilborg. *Flow analysis between two bluff bodies in a close distance platooning configuration*. Msc thesis, TU Delft, 2018.
- [73] Sadayuki Tsugawa. Results and issues of an automated truck platoon within the energy ITS project. *IEEE Intell. Veh. Symp. Proc.*, (Iv):642–647, 2014. doi: 10.1109/IVS.2014.6856400.
- [74] Sadayuki Tsugawa, Shin Kato, and Keiji Aoki. An automated truck platoon for energy saving. In *2011 IEEE/RSJ Int. Conf. Intell. Robot. Syst.*, pages 4109–4114. IEEE, sep 2011. ISBN 978-1-61284-454-1. doi: 10.1109/IROS.2011.6048157. URL <http://ieeexplore.ieee.org/lpdocs/epic03/wrapper.htm?arnumber=6048157>.
- [75] United States Environmental Protection Agency. Fast Facts US Transportation Greenhouse Gas Emissions 1990 - 2017, 2019.
- [76] U.S. Department of Energy. Vehicle Weight Classes & Categories, 2019. URL <https://afdc.energy.gov/data/10380>.
- [77] G Van Raemdonck. *Design of Low Drag Bluff Road Vehicles*. Phd thesis, TU Delft, 2012.

- [78] R. Veldhuizen, G. M.R. Van Raemdonck, and J. P. van der Krieke. Fuel economy improvement by means of two European tractor semi-trailer combinations in a platooning formation. *J. Wind Eng. Ind. Aerodyn.*, 188(September 2018):217–234, 2019. ISSN 01676105. doi: 10.1016/j.jweia.2019.03.002. URL <https://doi.org/10.1016/j.jweia.2019.03.002>.
- [79] Richard Wood. A Review of Reynolds Number Effects on the Aerodynamics of Commercial Ground Vehicles. *SAE Int. J. Commer. Veh.*, 5(2):2012–01–2045, 2012. ISSN 1946-3928. doi: 10.4271/2012-01-2045. URL <http://papers.sae.org/2012-01-2045/>.
- [80] Richard Wood. Reynolds Number Impact on Commercial Vehicle Aerodynamics and Performance. *SAE Int. J. Commer. Veh.*, 8(2):2015–01–2859, sep 2015. ISSN 1946-3928. doi: 10.4271/2015-01-2859. URL <http://papers.sae.org/2015-01-2859/>.
- [81] Richard M. Wood. A Discussion of a Heavy Truck Advanced Aerodynamic Trailer System. In *9th Int. Symp. Heavy Veh. Weight. Dimens. – USA – 2006*, 2006. URL <http://road-transport-technology.org/conferenceproceedings/2000s/ishvwd-9/>.